Thin Films for Solid Matrix Laser Desorption/Ionization for Biomarker Analysis

by

Chen Peng

A thesis submitted in partial fulfillment of the requirements for the degree of

Doctor of Philosophy

Department of Chemistry

University of Alberta

Abstract

Scientists and clinicians involved in the development of biomarkers confront the challenge of selecting the best analytical methods among dozens that have been reported in the literature. Creation of new and improvement of existing technologies is an integral part of the pathway to analytical systems. The work of this thesis investigates new tools for biomarker analysis, which may also inform biomarker discovery, using solid matrix laser desorption/ionization mass spectrometry (SMALDI-MS) by using porous nanostructured films fabricated by thin film process glancing angle deposition (GLAD). This project consists of three phases. The first objective of this thesis is to introduce a simple interface between digital microfluidic systems (DMF) and GLAD, which provides an attractive proof-of-concept that GLAD is available for off-line SMALDI-MS detection. The second objective is to demonstrate a ready-to-use on-chip digestion system, which is coupled to SMALDI-MS for peptide mass fingerprinting. This system underwent preliminary evaluation of digestion performance using a standard protein. The third objective is to investigate the ability to detect free amino acids with modified silicon (Si) GLAD film-based SMALDI. The application of GLAD nanostructured thin films to biomarker analysis SMALDI-MS is evaluated in this thesis.

Preface

The research conducted for this thesis is in part a research collaboration with Professor Michael J. Brett in the Department of Electrical and Computer Engineering at the University of Alberta. Dr. Michael T. Taschuk, Dr. Jason Sorge, Dr. Steven Jim, and Dr. Jane Hall assisted with the growth of the thin films. I received initial training on performing mass spectrometry from Reshma Singh. This thesis is an original work by Chen Peng. No part of this thesis has been previously published in a journal, but a portion of Chapter 4 was presented as a poster at the 2014 Canadian Society for Chemistry Conference, Vancouver, BC.

Acknowledgement

There are many people without whom I'd never have made it this far and I'd like to take this opportunity to express my sincere gratitude for their help and support.

First, I would like to thank my supervisor, Professor D. Jed Harrison, for his positive-attitude, enthusiastic encourage, and insightful guidance. He has built a fantastic working environment, with excellent people and instruments. I feel incredibly blessed to spend five years here with a person like him during my life.

I would like to extend my deepest gratitude to my Supervisory Committee members, Professors Steven H. Bergens, Mark T. McDermott, and Robert E. Campbell for their valuable advice during my graduate studies. I would like to thank Professors X. Chris Le and Thomas Thundat for serving in my candidacy defense. I am also grateful to Professors Richard Oleschuk, Julianne M. Gibbs-Davis, and Thomas Thundat for willingness to serve in my final defense.

I also would like to thank Professor Michael J. Brett for the opportunity to collaborate with his group. Thanks also go to his group, Dr. Michael T. Taschuk, Dr. Jason Sorge, Dr. Steven Jim, and Dr. Jane Hall for their expertise in fabricating films.

I am indebted to the entire NanoFab staff: Dr. Eric Flaim, Keith Franklin, Stephanie Bozic, Bob Brebber, Melissa Hawrelechko, Les Schowalter, Scott Munro, Glenn

Table of Contents

Chapter 3 Ready-to-use Immobilized-Tryptic Digestion Si GLAD Films for Peptide Mass Fingerprinting 55

Chapter 4 Functionalization of Si GLAD Films for Detection of Free Amino Acids.. 87

List of Tables

List of Figures

List of Schemes

List of Abbreviations

AD .... Alzheimer's disease

APTES... 3-aminopropyltriethoxysilane

Bis F17 .... bis(heptadecafluoro-1,1,2,2-tetrahydrodecyl) tetramethyldisiloxane

CE..capillary electrophoresis

CSF...cerebrospinal fluid

CT.. control

DIOS... desorption-ionization on porous silicon

DMF .... digital microfluidics

ESI-MS... electrospray ionization mass spectrometry

EWOD .... electrowetting-on-dielectric

FAA .... free amino acids

GA ....glutaraldehyde

GC-MS .... gas chromatography

GLAD...glancing angle deposition

GPTMS... 3-glycidoxypropyl trimethoxysilane

HCCA.. α-cyano-4-hydroxycinnamic acid

IMERs.. immobilized enzyme reactors

IS ....internal standard

LC .... liquid chromatography

LDI-MS .... laser desorption/ionization mass spectrometry

LOD... limit of detection

MALDI-MS .... matrix-assisted laser desorption/ionization mass spectrometry

MeOH .... methanol

MS .... mass spectrometry

NH_4HCO_3 .... ammonium bicarbonate

NIMS .... nanostructure-initiator mass spectrometry

NMR .... nuclear magnetic resonance spectroscopy

pAD .... probable Alzheimer's disease

PCR .... polymerase chain reaction

PMF .... peptide mass fingerprinting

PSA .... prostate-specific angtigen

SEM .... scanning electron microscopy

SERS .... surface-enhanced raman spectroscopy

Si .... silicon

SMALDI-MS .... solid matrix laser desorption/ionization mass spectrometry

TFA .... trifluoroacetic acid

TOF-MS .... time-of-flight mass spectrometry

TSH .... thyroid stimulating hormone

UTLC .... ultrathin layer chromatography

XPS .... X-ray photoelectron spectroscopy

Chapter 1 Introduction

1.1 Introduction

The last decades have witnessed an emerging role for molecular or biochemical markers indicating normal biological processes, pathogenic processes, or pharmacological responses to therapeutic drugs, often called 'biomarkers'.[1] For instance, the measurement of serum prostate-specific antigen (PSA) is used as a diagnostic biomarker and has a tremendous impact on the diagnosis of prostate carcinoma.[2]

In 2012, there are approximately 30 million people worldwide suffering from Alzheimer's disease (AD) and the World Health Organization projects that this number will triple in the next 20 years. AD is becoming a growing health issue and a major burden to the health systems of all nations.[3] AD is a progressive, incurable neurodegenerative disorder characterized by progression from memory loss to profound cognitive failure.[4] Drugs aimed at inhibiting neurodegenerative processes are likely to be most effective if the treatment is initiated as early as possible.[5] However, there is widespread support for the concept that AD has a long asymptomatic period.[4] This is where biomarkers may have a profound impact on AD diagnosis.[5] This thesis is dedicated towards new tools for biomarker analysis, which may also suggest biomarker discovery.

In general, proteomics and metabolomics based biomarker discovery and analysis employs either nuclear magnetic resonance spectroscopy (NMR)[6, 7] or mass spectrometry (MS); where the latter can be coupled with a separation technique such as gas

chromatography (GC-MS),[8-10] liquid chromatography (LC-MS)[11-13] or capillary electrophoresis (CE-MS)[14, 15]. Also, mass spectrometry can be performed using different mass analysers. This thesis will develop an alternate MS method to aid in biomarker analysis. Tools we are developing are based on time-of-flight mass spectrometry (TOF-MS) and on digital microfluidics (DMF) and we explore a silylated thin film technology of glancing angle deposition (GLAD) to develop a solid matrix laser desorption/ionization (SMALDI) method. Some model systems used as a vehicle to support this development are proteins, as related to proteomics, and AD biomarkers for metabolite analysis, as related to metabolomics.

Proteomics is the study of the entire population of proteins and peptides in an organism or a part of it, such as cells, tissues, or fluids like cerebrospinal fluid (CSF), plasma, serum, urine, or saliva.[3] A proteomic analysis has two steps: (i) protein separation and (ii) protein identification.[16] Two fundamental strategies for protein identification by mass spectrometry are employed in proteomics; these are classified as bottom-up and top-down approaches. The bottom-up approach in proteomics utilizes an initial treatment of protein digestion with a protease (usually trypsin) to cut proteins into relatively small peptides whose masses can be accurately determined by mass spectrometry. These peptide fragments can then be matched back to identify the originating proteins. This so-called "peptide mass fingerprinting (PMF)" allows reliable identification.[3] For the top-down approach, intact protein ions are subjected to fragmentation for mass spectrometric analysis.[17] Chapter 3 of this thesis is based on a bottom-up approach.

Metabolomics is the global study of metabolites and their concentration changes, interactions and dynamics in complex biological systems. Metabolome analysis covers the identification and quantification of all intracellular and extracellular metabolites with molecular mass lower than 1000 Da.[18] From the methodological point of view, there are two different approaches: (i) target analysis that includes identification and quantification of the selected metabolites in the sample and (ii) metabolite profiling that involves rapid analysis, often not quantitative, of a large number of different metabolites with the objective to identify a specific metabolite profile that characterizes a given sample.[19] The preliminary experiments in Chapter 4 have been developed to potentially facilitate target analysis.

MS is a frequently employed method of detection in the analysis of the proteome and metabolome. The specific choice of mass spectrometric methods is based on the molecular mass and fragmentation patterns.[19, 20] One of the methods is laser desorption/ionization mass spectrometry (LDI-MS). Siuzdak's group reported a matrix-free LDI-MS strategy, which has proven that nanostructured materials have advantages in LDI-MS.[21] Since GLAD is a powerful, elegant technique for fabricating nanostructures, our group have explored the use of nanostructured GLAD films in matrix-free LDI-MS.[22] Thus, the focus of this thesis is the application of silicon (Si) GLAD films to matrix-free LDI mass spectrometry detection with intended application in the fields of proteomics and metabolomics.

1.2 Objectives and Scope

With advances in micro and nanofabrication techniques during the last decade, proteomics and metabolomics may benefit from "lab-on-a-chip" technology, which has the potential to reduce sample handling, reduce surface contact, and allow for efficient automation. The first objective of this thesis is to introduce a simple interface of DMF and GLAD, which provided an attractive proof-of-concept that GLAD is available for off-line LDI-MS detection. The second objective is to demonstrate a ready-to-use on-chip digestion system, which is coupled to SMALDI-MS for peptide mass fingerprinting and is preliminarily evaluated by digestion performance using a standard protein. The third objective is to investigate the performance of detecting free amino acids (FAA) by modified Si GLAD films based SMALDI, for application in analysis of AD via metabolites.

1.3 Background Review

1.3.1 LDI-MS

Mass spectrometry developers have put major efforts into developing mass spectrometers for biomolecule detection for many decades. In the late 1980s, matrix-assisted laser desorption/ionization mass spectrometry (MALDI-MS) was pioneered by Karas and Hillenkamp. They first reported laser desorption of bioorganic compounds in the mass range above 10 000Da by using an organic matrix.[23] Since organic matrices are mixed with analytes in the technique, this is called matrix-assisted LDI. The first role of the matrix is to absorb the laser energy and convert most of it to heat, causing the sample to disintegrate. Second, the excited states of the matrix act as buffers, storing the laser energy and releasing it on a time scale similar to or longer than that of intra- and inter-molecular relaxation.[24] Figure 1.1 shows a schematic diagram of the desorption/ionization process of MALDI.
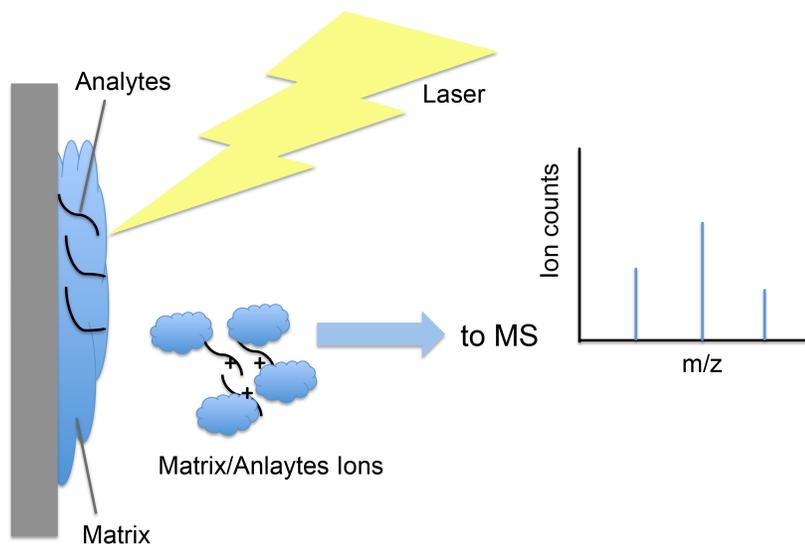
Figure 1.1 Laser irradiation to vaporize and ionize matrix/analytes in MALDI.

There are three major limitations in MALDI-MS. First, in a typical MALDI analysis, matrix selection and optimization are important steps but are still empirical procedures.[25] Second, in the low-mass region (below 700 Da), the use of MALDI is limited due to spectral interference from matrix-related ions. Third, MALDI-MS is not suitable for quantitative analysis, which result from inhomogeneous matrix/analytes cocrystallization. In 1999, Siuzdak's group reported a matrix-free LDI for biomolecular mass spectrometry based on desorption-ionization on porous silicon (DIOS). Their method uses porous Si to trap analytes deposited on the surface, and laser irradiation to vaporize and ionize them.[21] DIOS does not need a matrix to assist the desorption/ionization process. Furthermore, this matrix-free technique can reduce the background interference from the matrix in the low-mass region. A three step DIOS process model was proposed by Alimpiev *et al.* (1) adsorption of neutral analyte molecules by formation of hydrogen bonds with surface Si-OH groups, (2) the electronic excitation of the substrate to form free electron/'hole' pairs and (3) thermally-activated dissociation of analyte ions from the surface.[26] In 2007, the same group introduced nanostructure-initiator mass spectrometry (NIMS), which uses a nanostructured surface to trap "initiator" materials. Analytes are adsorbed on top of the NIMS surface. The laser irradiation results in rapid surface heating causing initiator vaporization, triggering desorption of adsorbed analytes.[27] The initiator materials are transparent to UV lasers and do not ionize, and the analytes are not incorporated or cocrystallized with the initiator, which represent the differences from MALDI. NIMS is able to analyze a wide range of biomolecules; e.g., small molecules, drugs, lipids and peptides, mouse embryo tissue imaging, and single cancers.[28]

Using the electrochemical etching method to fabricate porous Si films produces structures where there is some control of morphology. In 2010, Harrison's group applied a GLAD technique to fabricate nanostructured Si thin film with highly controlled morphology for use in SMALDI-MS. Peptides, drugs and metabolites in the mass range of 150-2500 Da were studied.[22] Based on SMALDI-MS and the GLAD technique, in this thesis we further explore the potential application of the GLAD technique in proteomics and metabolomics.

1.3.2 GLAD

1.3.2.1 GLAD Film Growth

GLAD is a single-step nanofabrication tool used to engineer nano-columns with controllable architecture. The GLAD technique involves physical vapor deposition of thin films onto rotating substrates oriented at highly oblique angles relative to the incident vapor stream, as shown in Figure 1.2.a.[29] With physical vapor deposition, the atoms are ejected from the source material. Barring collisions with other source atoms or residual gas, the vapor flux will travel ballistically to the substrate, where it is adsorbed and integrated in the growing film. During GLAD deposition at an angle α, defined in Figure 1.2.a., any surface topology is amplified by ballistic shadowing. The arrival of vapor flux is at an angle α and the nuclei grow into columns and shadows develop (see in Figure 1.2.b.). The columns and shadows they cast will have a size distribution. As a result, some nuclei will screen neighboring nuclei from incoming vapor flux, suppressing their growth as shown in Figure 1.2.c. Given sufficient time, smaller nuclei and columns can become completely shadowed and stop growing and isolated columns develop. This process, seen schematically in Figure 1.2.d., continues throughout the growth of a GLAD film.[30]

(a)

(b)

(c)

(d)
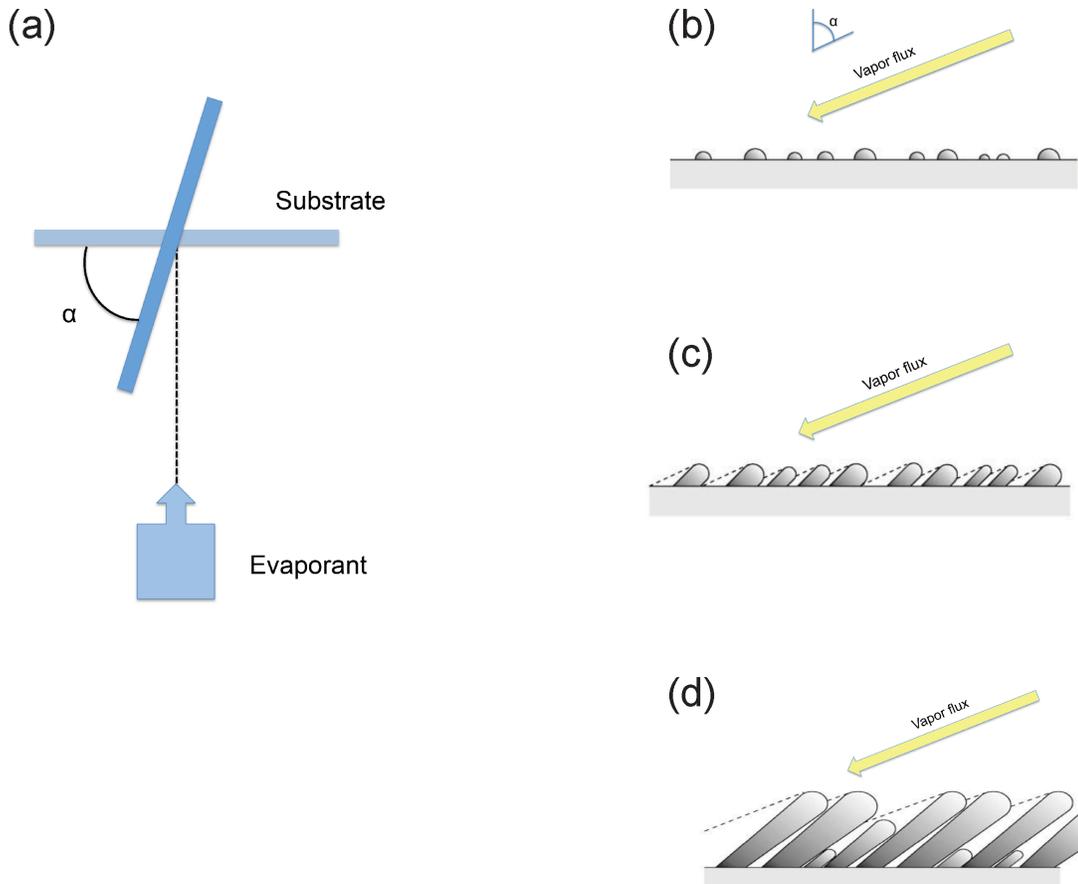
Figure 1.2 Schematic view of GLAD film growth: (a) the vapor flux arrives at an angle α, to the substrate normal; (b) film nuclei formation; (c) nuclei grow and develop shadows; (d) some columns shadowed by larger neighbors.

1.3.2.2 GLAD Applications in Chemistry and Biology

GLAD films have found application in many fields. In this section, the focus is on chemistry and biology applications. The large surface areas make GLAD films are ideal for sensing studies. Steele *et al.* utilized TiO_2, SiO_2 and Al_2O_3 GLAD films for humidity sensors.[31] Zhang *et al.* demonstrated the sensitivity enhancement of a photonic crystal biosensor through the incorporation of TiO_2 GLAD films.[32] Gish *et al.* evaluated the capability of a localized surface plasmon resonance biosensor, which was fabricated by Ag GLAD films.[33] Another sensing approach, which has received significant attention, is

8

surface-enhanced raman spectroscopy (SERS). Zhao's group developed a SERS probe based on a Ag nanorod array.[34] This SERS platform was used to detect viruses and microRNA.[35, 36] Brett's group explored the application of GLAD film as separation tools, such as microfluidics and ultrathin layer chromatography (UTLC) applications. Kiema *et al.* fabricated microfluidic structures based on the GLAD technique.[29] Bezuidenhout *et al.* presented a GLAD grown micro- and nanostructured microfluidic device for the separation of DNA mixtures.[37] Bezuidenhout *et al.* produced a GLAD-UTLC plate with controllable nanostructure and thickness.[38] Kirchert *et al.* reported the first GLAD-UTLC qualitative analysis of a real food sample.[39] Due to the highly controlled morphology of GLAD films, Jemere *et al.* demonstrated the application of Si GLAD films in matix-free LDI-MS.[22]

1.3.3 Digital Microfluidics

1.3.3.1 Microfluidics and DMF

There is a growing demand to integrate analytical techniques with microfluidics to provide miniaturized platforms with many favorable properties, such as reduced sample volume, decreased processing time, low cost analysis and low reagent consumption.[40] The microfluidics are conceptually derived from macroscopic devices, taking into account the particularities brought by the reduction of the dimensions and the physical modifications due to the influence of the solid walls.[41] Currently, most of the microfluidic devices are based on continuous fluid flow. An alternative approach to microfluidics is DMF, which manipulate the liquid as unit-sized discrete microdroplets. Because of its architectural similarities to digital microelectronic systems, this approach is referred to as "digital"

9

microfluidics.[42] Although microfluidics have also been used to manipulate droplets, DMF is a distinct paradigm.[43] The principal difference is that in DMF, samples are addressed individually, while in microfluidics, they are controlled in series.[44] The second difference is that DMF is capable of addressing all the reagents in an assay individually with no need for complex networks of microvalves.[45]

1.3.3.2 DMF Device Configurations and Fabrication

There are two configurations for DMF implementation as shown in Figure 1.3: closed format and open format. In a closed format (also known as two-plate format), the droplets are sandwiched between two substrates (the substrates housing the actuation and ground electrodes, respectively). In an open format (also known as single-plate format), the droplets are placed on top of a single substrate (housing both actuation and ground electrodes).[46] In both configurations, a dielectric layer is deposited on top of the electrodes and the dielectric layer is covered by an additional hydrophobic coating.
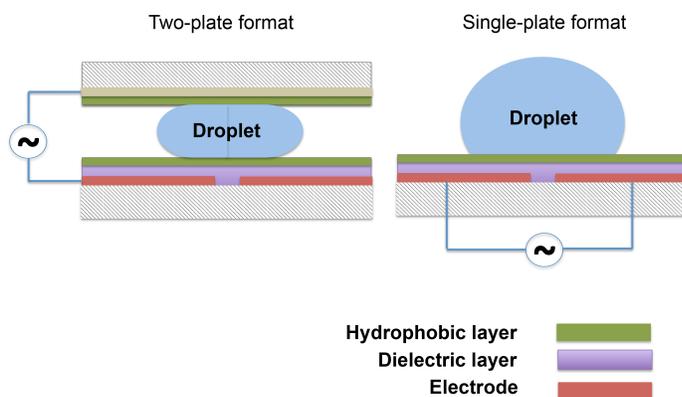
Figure 1.3 Schematics of closed and open DMF devices. The actuation electrodes plate is composed of electrodes, a dielectric layer, and a hydrophobic layer.

DMF devices are typically fabricated in a clean room. Electrodes are formed from substrates, such as chromium, gold, indium-tin oxide, and doped polysilicon, which are common to photolithography facilities. A variety of techniques, including vapor deposition (for parylene, silicon nitride), thermal growth (for silicon oxide) or spin-coating (for PDMS or SU-8) are used to deposit the dielectric layer on top of the electrodes. A hydrophobic layer, typically Teflon-AF, is deposited by spin-coating.[44] Table 1.1 lists common fabrication materials in DMF devices.

Table 1.1 Summary of commonly used DMF device fabrication materials.

Electrode	Dielectric layer	Hydrophobic layer	Reference
Au	Parylene C	Teflon	47
Cr, Au	SU-8 GM1040	Teflon	48
Cr, Pt	SiO_2	Teflon	49
Cr, Au	Parylene C	Teflon	50
Cr, Au	Parylene C	Teflon	51
Cr, Au	Parylene C	Teflon	52
Cr	Parylene	Teflon	53
Ti, Pt, Au	Si_3N_4	Teflon	54
Phosphorous-doped polysilicon	Thermal oxide	Teflon	55

1.3.3.3 DMF Droplet Actuation Physics

DMF is explained as being a phenomenon driven by "electrowetting" or "electrowetting-on-dielectric" (EWOD).[44] We follow the model of virtual displacement to explain EWOD.[56] The thermodynamic system is defined as a droplet, a dielectric layer, an electrode, and a power supply. An ideal smooth solid surface was supposed at the contact of a conductive liquid or an electrolyte. When a voltage V is applied between a droplet and an electrode, a charge density σ_L builds up in the droplet close to the liquid-solid interface and this induces an image charge density σ_E on the electrode as shown in Figure 1.4.
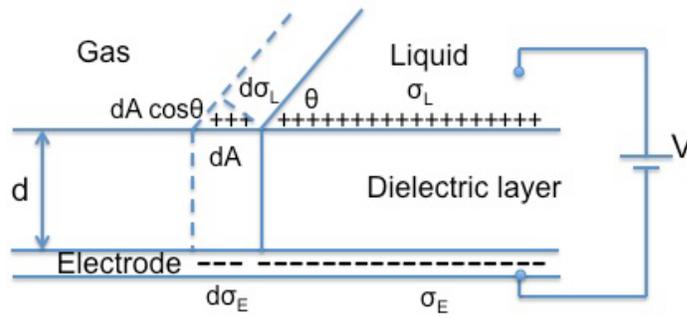
Figure 1.4 Schematic drawing of the electric charges during electrowetting.

An infinitesimal increase in area dA at voltage V changes the interface area and the liquid-solid surface charges increase additional $d\sigma_L$ and the image charge $d\sigma_E$. As a result, the droplet free energy changes. The free energy of the system (E) can be written in differential form

$$dE = \gamma_{SL}\, dA - \gamma_{SG}\, dA + \gamma_{LG}\, dA\cos\theta + dU - dW \quad (1.1)$$

Where U is the energy stored in the dielectric layer and W is the work performed by the voltage supply. γ is the surface tension, which is defined as the work done per unit area.

γ_{SL} A, γ_{SG} A, and γ_{LG} A$\cos\theta$ are the free energies of the solid-liquid, solid-gas and liquid-gas interfaces, respectively.

First, in the situation of no voltage supplied, dU=dW=0. At equilibrium, dE/dA=0, therefore, γ_{SL}-γ_{SG}+γ_{LG} $\cos\theta$=0, which is Young's equation. For a nonzero voltage V, the energy stored in the dielectric is

$$\frac{dU}{dA} = \frac{1}{2} V \sigma_L \quad (1.2)$$

When the droplet shape changes, the surface charges on the liquid-solid surface area changes immediately. The energy stored in the charge source is then twice the energy stored in the dielectric.

$$\frac{dW}{dA} = V \sigma_L \quad (1.3)$$

Setting dE/dA=0, Young's equation with an additional electrowetting term γ_{EW} was obtained,

$$\gamma_{LG} \cos\theta = \gamma_{SG} - \gamma_{SL} + \gamma_{EW} \quad (1.4)$$

where the electrowetting force $\gamma_{EW} = \frac{\varepsilon_0 \varepsilon_D}{2d} V^2$, ε_D is the dielectric constant of the dielectric material, ε_0 is the permittivity of vacuum and d is the thickness of the dielectric layer.

When the voltage V induces the electrowetting, the contact angle changes from θ_0 to θ.

$$\gamma_{LG} (\cos\theta - \cos\theta_0) = \frac{\varepsilon_0 \varepsilon_D}{2d} V^2 \quad (1.5)$$

The dielectric layer has a fixed specific capacitance (capacitance per unit area)

$$C = \frac{\varepsilon_0 \varepsilon_D}{d} \quad (1.6)$$

Therefore, Lippmann-Young's equation is obtained

$$\cos\theta - \cos\theta_0 = \frac{C}{2\gamma_{LG}} V^2 \quad (1.7)$$

From this model, we see that by applying voltage to the electrodes on DMF devices, the contact angle is changed. The changes of contact angle resulting from the change of the shape of the droplet lead to microdroplet transportation.[56]

1.3.3.4 DMF Applications in Chemistry and Biology

DMF is an attractive platform in chemistry and biology applications, such as DNA, enzyme assays, immunoassays and cell assays. Abdelgawad *et al.* demonstrated the first DNA handling and purification by using DMF.[46] Liu *et al.* developed a DMF device to facilitate DNA repairing by DNA ligation.[57] The most complete DNA application was reported by Chang *et al.* Their team presented a DMF device for polymerase chain reaction (PCR).[54] The DMF/PCR biochip shows the advantages of small size, rapid heating/cooling rates, low reagent/sample consumption, and lower power consumption. Enzyme assays and immunoassays are used to selectively detect analytes in biological samples. Taniguchi *et al.* demonstrated a bioluminescence assay for luciferase by using DMF.[58] Srinivasan *et al.* reported a fully automated glucose assay in a range of serum, saliva, plasma and urine on a DMF device.[59] Sista *et al.* presented a DMF platform for multiplex enzyme assays for a newborn screening laboratory to screen lysosomal storage disease.[60] Ng *et al.* introduced particle-based immunoassays relying on DMF using a thyroid stimulating hormone (TSH) as model analytes.[61] The same team later developed an automated DMF platform for particle-based immunoassays.[62] Since cell assays are often expensive due to the reagents and materials, the miniaturization platform-DMF is an obvious match. Bogojevic *et al.* presented the multiplexed cell-based screening assay

implemented by DMF.[63] Au *et al.* reported the study of genome-level effects on cells manipulated by DMF.[64]

The capacity of DMF for individually addressing many reagents also provides a good fit for the field of proteomics, which requires tedious multistep sample processing prior to analysis by mass spectrometry.[53] The work in this area, focusing on the combination of DMF sample handling with detection by MALDI-MS is reviewed here. Wheeler *et al.* reported in-line peptide sample purification for MALDI mass spectrometry, which relies on DMF.[55] Moon *et al.* demonstrated an integrated DMF chip for multiplex proteomic sample preparation and analysis by MALDI mass spectrometry.[65] The methods comprised a series of rinsing steps, with peptides analyzed off-chip by MALDI-MS. More recently, Luk *et al.* integrated many proteomic processing steps including protein precipitation, rinsing, resolubilization, reduction, alkylation, and digestion into an automated DMF platform.[66] The same team later integrated agarose discs bearing immobilized enzymes into DMF systems for digesting proteins.[67] In their work, they developed a complete proteomic workup including digestion based on DMF platform.

1.3.4 Immobilized Enzyme Reactors in Proteomics

Enzymatic digestion of the analyzed proteins and coupling with mass spectrometry are the common steps in proteomics.[68] Traditionally, protein digestion is performed by free enzymes, typically trypsin. With this approach, a small number of enzymes is added into protein solutions that require a long incubation time (typically 5-24 h). In recent years, protein digestion by enzymes immobilized on solid supports, referred to as immobilized

15

enzyme reactors (IMERs), has been shown to achieve efficient digestion in shorter digestion time and has gained in popularity.[69]

One of the most striking features of IMERs is the coupling of IMERs to separation and identification systems which enables high-throughput and automated proteome profiling.[69] In general, IMERs can be coupled with CE[70, 71] and HPLC[72-75] for separation. Capillary IMER can be directly coupled on-line with ESI-MS for speedy protein identification or off-line with MALDI-MS.[76, 77] Less developed, on-line coupling with MALDI, in principle, can also be achieved. For example, Ekstrom *et al.* described a microchip IMER that interfaced to a MALDI target plate for automated MS analysis.[78] Xu *et al.* reported in situ digestion of proteins on the porous silicon surface modified by trypsin. However, their DIOS mass spectra results showed that the modified protein surface is not suitable for the detection of peptide residues unless matrix is added to improve the desorption/ionization efficiency.[79]

1.3.4.1 Immobilization Chemistry

The two categories of immobilization techniques are noncovalent immobilization and covalent immobilization.[68, 80] Covalent coupling is formed by the reaction of functional groups of the selected enzyme with the proper solid support. Most often, ε–amino groups on lysine residues in enzymes are used for covalent attachment.[81] In this section, the focus is on two covalent immobilization techniques used in this thesis.

1.3.4.1.1 3-Glycidoxypropyl Functionality

Temporini *et al.* prepared a number of bioreactors based on the commercially available silica-based monolithic column activated with 3-glycidoxypropyltrimethoxysilane.[75, 82, 83] The reaction path resulting in enzyme immobilization is shown in Figure 1.5. 3-Glycidoxypropyl silane hydrolyzes on a silica surface to bond to it, and the nucleophilic ε–amino groups in the enzyme attack the epoxy groups forming a covalent linkage.
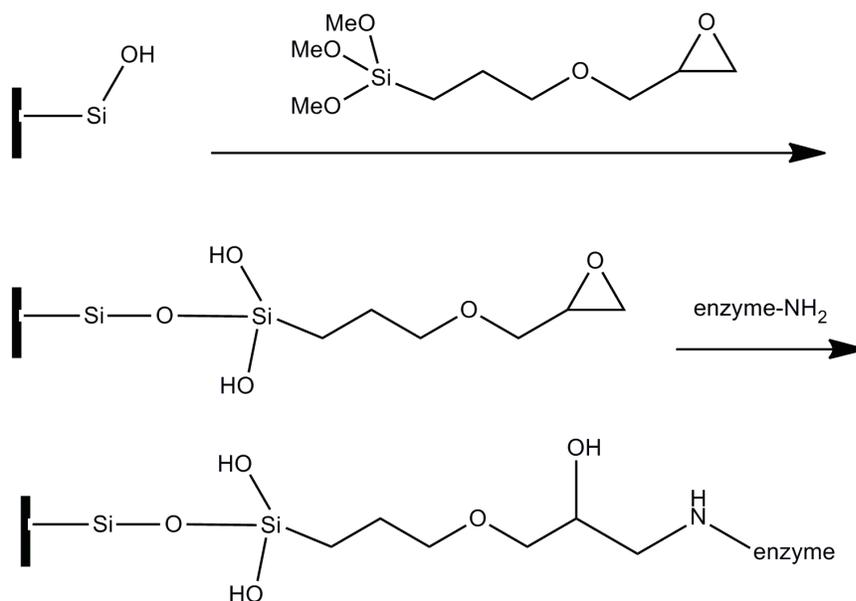
Figure 1.5 Activation of silica-based monolith using 3-glycidoxypropyltrimethoxy-silane and immobilization of enzyme through its amine functionalities.[68]

1.3.4.1.2 Glutaraldehyde Approach

Glutaraldehyde, a linear, 5-carbon dialdehyde, is soluble in all proportions in water. However, the glutaraldehyde structure in an aqueous solution, in which the crosslinking reaction with proteins is carried out, is not limited to the monomeric form.[84] The possible forms are shown in Figure 1.6. There is still argument about the main reactive species in glutaraldehyde solutions during the crosslinking process.
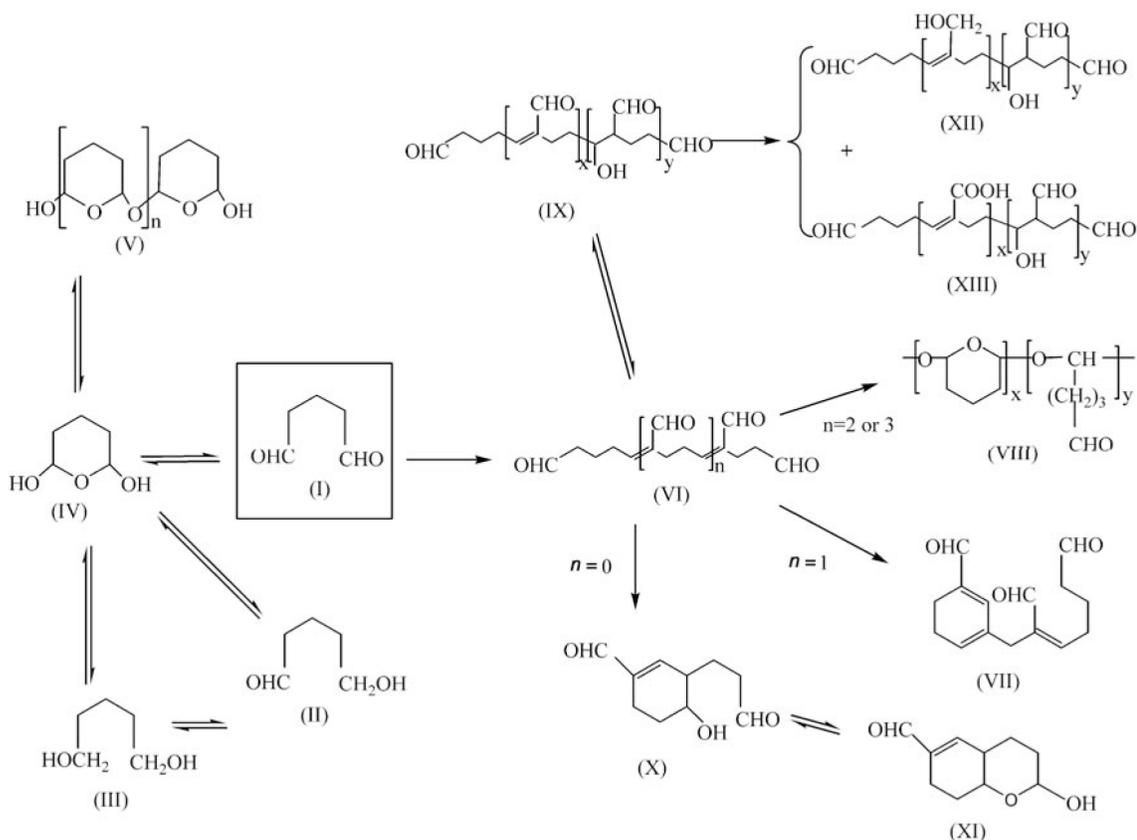
Figure 1.6 Summary of the possible forms of glutaraldehyde in aqueous solution. Chemical I is glutaraldehyde monomer and the origins and identity of the other postulated or determined species are discussed in detail in Migneault's paper[84] (© 2009 BioTechniques. Used by Permission)

Aldehydes are expected to form Schiff bases upon nucleophilic attack by the ε–amino groups of lysine residues. However, Schiff bases are unstable under acidic conditions and tend to break down to regenerate the aldehyde and amine. In contrast, the linkage formed by the reaction of glutaraldehyde with an amino group has shown stability at extreme pHs. Thus, a simple Schiff base with both ends of monomeric glutaraldehyde has been ruled out as a mechanism for glutaraldehyde crosslinking with proteins. Several alternative mechanisms have been proposed. Monsan *et al.* proposed that the reaction involved the conjugate addition of protein amino groups to the aldehydic part of the α, β-unsaturated polymers (and poly-glutaraldehyde) to give a Schiff base (imine) stability by conjugation (Figure 1.7, reaction 1).[85] Richards *et al.* proposed a slightly different mechanism in which an addition reaction occurred on ethylenic double bonds (Michael-type addition) of the α, β-unsaturated oligomers (Figure 1.7, reaction 2).[86]
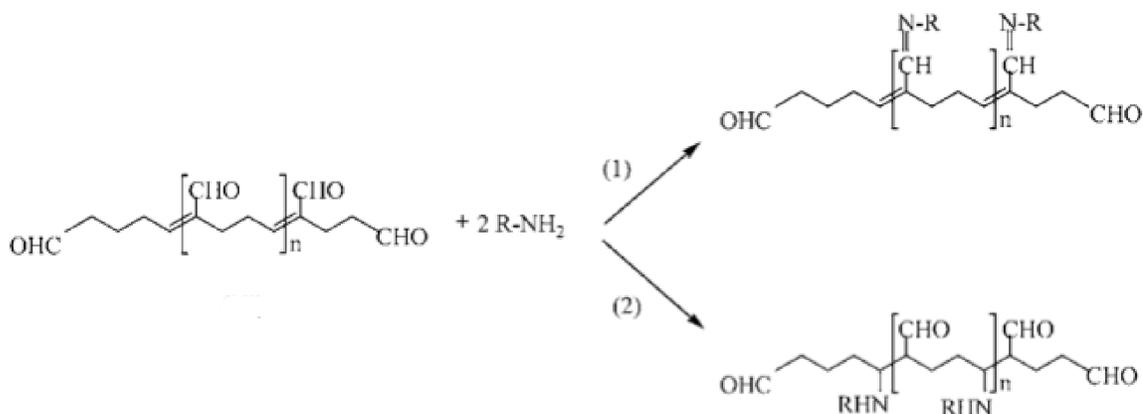
Figure 1.7 (1) Schiff base and (2) Michael-type reactions of glutaraldehyde with proteins.[84] (© 2009 BioTechniques. Used by Permission)

1.4 Thesis Outline

This thesis reports the investigation of Si GLAD films applied to SMALDI-MS in proteomics and metabolomics. Three aspects were identified in which Si GLAD nanostructured films could potentially provide an opportunity for low-cost, fast LDI mass spectrometry analysis: coupling with DMF chips, on-line immobilized-tryptic digestion, and FAA detection.

In this chapter, overall objectives and scope of this study have been laid out. We discussed SMALDI-MS. A brief description of DMF and GLAD technique, and IMERs are presented to facilitate the discussions in the following chapters.

Chapter 2 reports how DMF devices were fabricated and demonstrates a simple interface of DMF and GLAD, which provided an attractive proof-of-concept that GLAD is available for off-line LDI-MS detection. The difference in hydrophobicity of DMF and GLAD provides a unique opportunity to fabricate an interface where the off-line mass spectrometry can be applied. The results provided a proof-of-concept of a feasibility of combining DMF devices with LDI-MS.

In Chapter 3, we introduce a ready-to-use chip, which is a Si GLAD film functionalized with silane, followed by immobilization of trypsin via covalent bonding. The performance of this chip is evaluated by digestion performance using a standard protein. Although the result of immobilized-tryptic digestion does not show advantages compared with the result of free-solution tryptic digestion, it provides a matrix-free LDI detectable modified

surface. Our method showed higher sensitivity (pmol) than previous reported modifications for trypsin immobilization that cannot be detected without adding a matrix.[79] The resulting functionalized GLAD films provide the possibility towards low-cost and fast peptide mass fingerprinting analysis.

The performance of detecting FAA by silylated Si GLAD films was investigated in Chapter 4. Two Si GLAD film functionalization approaches have been studied. The reliability of the approach is quantitatively demonstrated with calibration of asparagine, glutamine and histidine pure samples, illustrating the sensitivity of the method for FAA detection is 400-fmol, 300-fmol, and 300-fmol levels, respectively. The overall results show the feasibility of silylated Si GLAD films to analyze FAA with LDI-MS. The FAA detection technique expanded the potential application of GLAD techniques in metobolomics.

Chapter 5 concludes the present progress of this work and discusses future perspectives and opportunities.

Chapter 2 DMF-GLAD Interface for SMADI Detection

2.1 Introduction

Mass spectrometry is one of the most powerful tools in analytical science. Sample preparation before introduction into the mass spectrometer can be labor intensive and time-consuming. Digital microfluidics (DMF) devices present the potential of sample preparation followed by coupling to a mass spectrometer. Shih *et al* developed a method to couple DMF to nanoelectrospray ionization mass spectrometry.[87] Boukherroub's group presented the integration of an off-line matrix-free analysis on silicon (Si) nanowires with a DMF system.[88] They developed a device comprising a digital microfluidics system and a patterned superhydrophobic/superhydrophilic silicon nanowire interface. In their device, the unpatterned electrode layer was a Si substrate functionalized to be superhydrophobic, and then selected positions were processed to be superhydrophilic through oxygen plasma treatment. In their work, they used chemical etching to prepare Si nanowire substrates interfaced to the DMF region of the device. Notably, they lacked control of the morphology of the nanowire substrates when fabricated this way. Our group members demonstrated the performance of Si glancing angle deposition (GLAD) films, which is fabricated by a single-step nanofabrication tool with controllable nano-columns, for solid matrix laser desorption/ionization (SMALDI) analysis of small molecules (mass range of 150-2500 Da).[22] We developed a DMF-GLAD interface system for the purpose of coupling DMF to SMALDI at a similar time to Boukherroub's group. In the first part of this study, we fabricated a commonly used DMF device design, which consisted of a patterned electrode layer and an unpatterned electrode layer. In the second part, we built

up an interface of DMF to Si GLAD by mounting the Si GLAD film within the DMF devices. Although our DMF devices were limited by the droplet transportation repeatability, we were able to perform peptide droplet in-line mass spectrometry detection.

The work presented in this chapter was in collaboration with Dr. Michael Brett's group in the Department of Electrical and Computer Engineering at the University of Alberta. Jane Zhen Hall assisted with the growth of the GLAD films.

2.2 Experimental Section

2.2.1 Chemicals and Materials

HPR 504 positive (Fujifilm Electronic Materials USA Inc., North Kingstown, RI, USA) and Microposit 354 Developer (Shipley Company, L.L.C., Marlborough, MA, USA) were used in DMF fabrication process. Silicon wafers (Test Grade, 10 cm diameter, University Wafer, Boston, MA, USA) and evaporated material, silicon (CERAC, Inc., Milwaukee, WI, USA) were used in the GLAD fabrication process. [Des-Arg^9]-bradykinin (MW=903), trifluoroacetic acid (TFA) and methanol were from Sigma-Aldrich. Solutions were prepared using ultrapure water prepared with a deionizing system (Millipore Canada, Mississauga, ON, Canada). [Des-Arg^9]-bradykinin stock solutions were prepared by constituting lyophilized samples in water. Samples were diluted in methanol/0.1% TFA (30/70, v/v).

2.2.2 DMF Devices Fabrication

DMF devices were fabricated in the University of Alberta NanoFab, using a chrome-on-glass photomask printed at the NanoFab (Edmonton, AB). The device design featured an array of actuation electrodes (1.8 mm × 1.8 mm) with inter-electrode gaps of 4 μm and contact pads (2 mm × 2 mm). The two electrode-plates configuration was used in our design.

2.2.2.1 Patterned Substrates Fabrication

2.2.2.1.1 Electrodes Fabrication by Photolithography

Prior to electrode patterning, 0211 glass substrates (University of Alberta, Edmonton, AB) were cleaned in hot piranha solution (H_2SO_4: H_2O_2, v: v/1:3) for 15 min and then sputtered to give a 250 nm chromium (Cr) layer, using a planar magnetron sputtering system. Substrates were then coated with HPR 504 at a spin rate of 4000 rpm for 40 s. After baking in an oven at 115°C for 30 min, devices were exposed to UV radiation through a Cr-on-glass photomask (NanoFab, Edmonton, AB), using an ABM mask aligners at exposure energy of 89.8 watt/cm^2 for 2.0 s. After exposure, exposed photoresist was etched away by agitation in Developer 354 for 40 s, followed by deionized water rinsing and nitrogen gun drying. Substrates were then immersed in Cr etching for 3 min, followed by rinsing with deionized water and drying with nitrogen. Substrates were protected with a thin film of photoresist and then cut into the desired size by a Diamond Touch dicing saw.

2.2.2.1.2 Dielectric Layer Coating

Before dielectric coating, substrates were cleaned in cold piranha (H_2SO_4: H_2O_2, v: v/1:3) solution for 15 min. Patterned electrodes were coated with parylene C dielectric layer for a thickness of 2.5 μm, using a vapor deposition system.

2.2.2.1.3 Hydrophobic Layer Coating

After deposition of dielectric layers, devices were spin coated with a 50 nm thick hydrophobic layer, formed from 1% Teflon AF in Fluorinert FC-40 at a spread speed of 500 RPM for 20 s, followed by a spin rate of 3000 RPM for 60 s. Substrates were baked in an oven at 175°C for 10 min and then kept in the oven while it cooled to room temperature.

2.2.2.2 Unpatterned Substrates Fabrication

Unpatterned indium tin oxide coated glass substrates (Delta Technologies Ltd, Stillwater, MN) were cleaned in cold piranha (H_2SO_4: H_2O_2, v: v/1:3) solution for 15 min. These glass substrates were taped on Si wafers due to the limitation of the size of spin coating loading chucks. Substrates were spin coated with a hydrophobic layer for a thickness of 50 nm as above.

2.2.3 GLAD Film Fabrication

Silicon wafer substrates were cleaned prior to deposition by hot piranha (H_2SO_4: H_2O_2, v: v/1:3) solution for 15 min. Silicon vertical posts of 500 nm were deposited using GLAD at angle of 86° relative to the substrate normal, using a substrate rotation rate of 1.2 RPM at a deposition rate of 0.4 to 0.9 nm/s. Scanning electron microscopy images were taken of chromium coated samples using JEOL 6301F field emission scanning electron microscope.

2.2.4. DMF Instrumentation

The device used a two-plate configuration. As presented in Figure 2.1, a droplet was sandwiched between a bottom patterned electrode plate and a top unpatterned electrode plate. A double-sided tape spacer was used between the two plates. AC electric potential was applied on patterned electrodes via the exposed contact pads and the unpatterned electrodes were grounded.
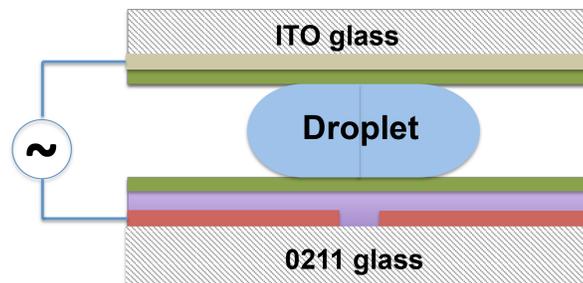
Figure 2.1 Schematic graph of a two-plate configuration DMF device: a spacer was used between two plates and a droplet was sandwiched between the bottom patterned electrode plate and the top unpatterned electrode plate.

2.2.5 DMF-GLAD Interface

The DMF-GLAD coupling interface was composed of a piece of 3 mm × 3 mm Si GLAD film by attaching to the unpatterned DMF layer by double-sided tape. Si vertical posts were facing down as presented in Figure 2.2.
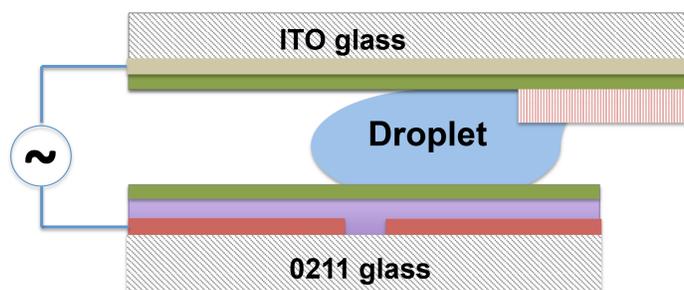
Figure 2.2 Schematic graph of DMF-GLAD devices. A piece of Si GLAD film was attached to the unpatterned DMF layer by double-sided tape.

2.2.6 Mass Spectrometry

SMALDI measurements were made using an AB SCIEX 4800 Plus MALDI TOF/TOF mass spectrometer, operated with a pulsed frequency tripled Nd: YAG laser at 355 nm, at a repetition rate of 200 Hz. Positive ion mode mass spectra were acquired under the following conditions. The reflector, delayed extraction mode was used. An accelerating potential of 20 kV, an 80% grid potential and a delay time of 210 nsec was applied. Each spectrum is the result of 400 laser shots. Si GLAD film was separated from DMF system and attached to MALDI plate by conductive double-sided tape.

2.3 Results and Discussion

2.3.1 DMF Device Characterization

Two electrode-plate configuration DMF devices were fabricated as described in the experimental section. The features of our devices are common to device designs presented by other groups.[55, 65] Characterization for each layer was performed and is discussed in the following section.

2.3.1.1 Electrodes and Dielectric Layers

The DMF chip was composed of two basic units, the electrodes and the dielectric layers. By applying voltage to the electrodes, the droplets can move within the devices. As previously described in Chapter 1, the model of virtual displacement was used to explain the microdroplet transportation. The thermodynamic system is defined as a droplet, a dielectric layer, an electrode and a power supply. An ideal smooth solid surface was supposed at the contact of a conductive liquid or an electrolyte. When a voltage V is applied between a droplet and an electrode, the contact angle changes from θ_0 to θ, with the system described by Lippmann-Young's equation, where C is specific capacitance

$$\cos\theta - \cos\theta_0 = \frac{C}{2\gamma_{LG}} V^2 \ (2.1)$$

From this model, we see that by applying voltage to the electrodes on DMF devices, the contact angle is changed. The changes of contact angle resulting from the change of the shape of the droplet lead to microdroplet transportation.[56]

The patterned electrodes used in our devices are Cr. In reality, the surface roughness is one of the reasons for hysteresis. Hysteresis is the local change of contact angle and its extreme form is droplet pinning, in which the droplet cannot move around the device. This effect will be described in more detail in the following minimum-voltage section. For the purpose of evaluating the chip fabrication quality, the surface roughness of the Cr electrode was measured by profilometry. A Zygo optical profilometer, which is based on scanning white light interferometry, was used to measure Cr electrodes surface roughness. Figure 2.3 showed an example surface profile for one measurement. The surface profile contains information from the scanning surface map, as shown on the right as a three dimensional oblique plot. The vertical axis in the plot is the peak-to-valley value marked by different colors. This plot describes the peak-to-valley distribution of a 0.72 mm × 0.54 mm spot surface. On the left-lower corner, PV, rms and Ra are the parameters we used for evaluating the surface roughness. PV stands for peak-to-valley height, which is measured by the profilometer. The profilometer calculates the roughness differently for rms and Ra. Rms is a root mean squared calculation of surface heights measured across the peak and valley. Ra is the arithmetic average of surface heights across the peak and valley. In our measurements, five different spots on the Cr surface were selected and each spot was measured three times. The rms roughness of the Cr is less than 0.5 nm, with a maximum peak-to-valley distance of 6 nm. It is known that roughness on this scale does not influence the contact angle significantly.[89] The surface profile analysis indicates that the Cr electrode can be considered as smooth and homogenous for application in DMF.
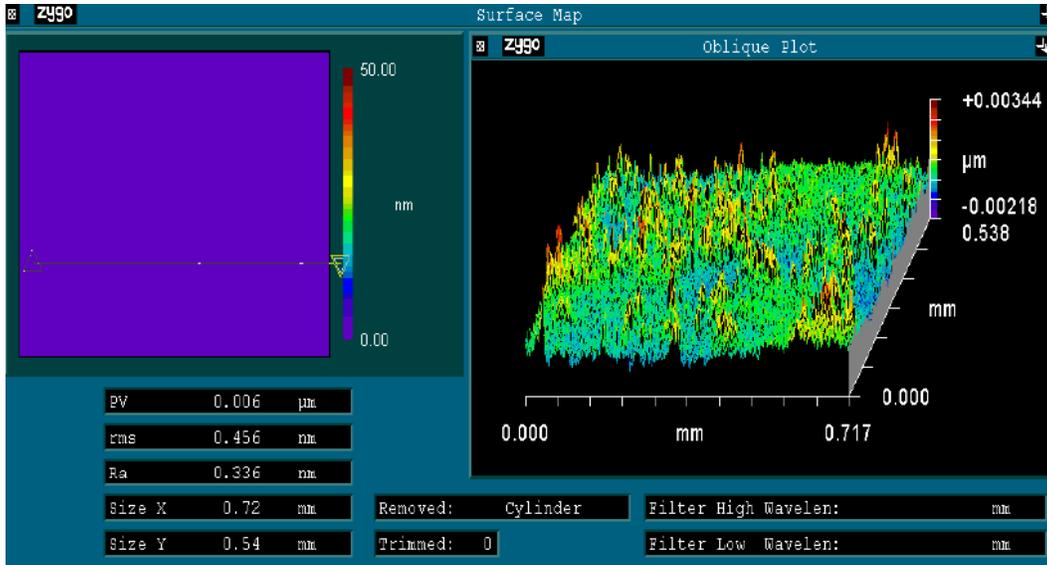
Figure 2.3 Profilometer measured surface profile. It describes the peak-to-valley distribution of 0.72 mm × 0.54 mm spot surface. Data shown in lower-left corner box: PV=0.006 μm, rms=0.456 nm, Ra=0.336 nm.

The parylene C polymers were chosen in the chip design because they have a high dielectric constant of 3.2. From previous analysis, we know that when a voltage V is applied to DMF devices, the contact angle changes from θ_0 to θ. From Lippmann-Young's equation, for the purpose of reducing applied voltage, a dielectric layer with high dielectric constant is preferred to deposit on the electrodes. The polymers are deposited using a vapor phase deposition process, which consists of three steps: 1) vaporization, 2) pyrolization and 3) deposition, as outlined in Scheme 2.1. The first step is vaporization of the solid dimer at 175°C. The second step is cleavage of the dimer to obtain the stable monomeric diradical molecules at about 660°C. The third step is the monomers adsorb and polymerize on the substrate in the deposition chamber at room temperature.[90] Under the vapor deposition process conditions, the large average number of collisions required per polymerization (10 000) and the short mean free path of the molecular vapor (less than 1 mm) leads the coating to form slowly and uniformly over the surface, with no pin holes found even in submicron film thicknesses. Therefore, the substrates are considered uniformly encapsulated and the coatings should be homogenous.[91] The thickness is measured by an Alphastep250 profilometer. Three different spots were measured. The thickness is 2.57 ± 0.01 μm.
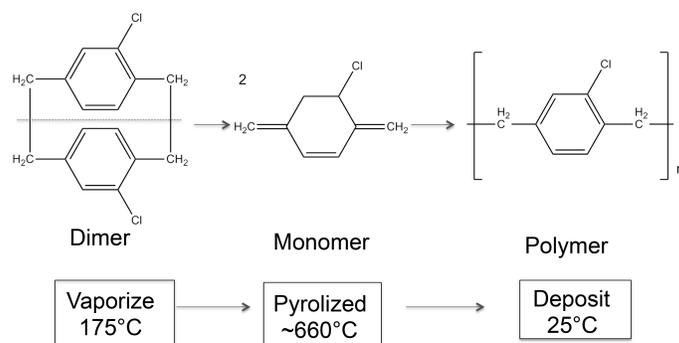
Scheme 2.1 Parylene C deposition process. The parylene C polymers vapor deposition process consists of three steps (1) vaporization, (2) pyrolization and (3) deposition.

2.3.1.2 Hydrophobic Layers

A hydrophobic layer, which makes the liquid-solid surface more hydrophobic, is used to cover the dielectric layer for the purpose of increasing the initial contact angle θ_0. When a voltage V is applied, the contact angles need to change from θ_0 to θ to actuate the droplet movement. From Lippmann-Young's equation, the larger the initial contact angle θ_0 is, the lower is the voltage needed to actuate droplet transportation. Teflon AF is the most typically used hydrophobic material, which has the largest contact angle among commercially available materials. Teflon [chemical name: fluorinated (ethylenic-cyclo oxyaliphatic substituted ethylenic) copolymer] is a family of amorphous fluoropolyers and the general chemical structure is shown in Figure 2.4.[92]
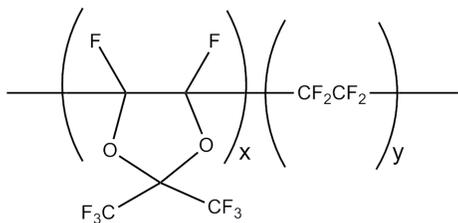
Figure 2.4 Teflon AF chemical structure.

Since Teflon AF film coating was a new area to the University of Alberta NanoFab, developing a Teflon AF process was part of the DMF project. Teflon AF resins in two concentrations were investigated, 6% and 1% Teflon AF in Fluorinert FC-40. A Teflon AF film was coated on substrates by spin coating. The spin coating can be divided in three stages. First, the solution is distributed to the rotating substrate. Second, spreading of the solution takes place due to centrifugal force and the thickness is reduced to a critical height. Finally, the subsequent reduction in film height under spin speed is dominated by evaporation of the solvent. After spin coating, the substrates were baked in an oven to

remove solvents. The film thickness and the contact angles are two important parameters used to quantitatively evaluate Teflon AF films. The spin coating calibration curves and the contact angle calibration curves were obtained.

2.3.1.2.1 Complex Index of Refraction

Optical parameters were first measured on Teflon AF, to later be used for film thickness measurements. The refractive indices (n and k) were obtained by variable angle spectroscopic ellipsometry. A thin Teflon AF film on a Si wafer was prepared. By using the ellipsometry processing software, a Cauchy model with a Teflon AF film on Si was built up and applied to Teflon AF films on a Si substrate over the scanning wavelength range from 300 to 1700 nm. The index of refraction versus wavelength data can be provided by the Sellmeier equations,

$$n^2(\lambda)=1+\frac{B_1\lambda^2}{\lambda^2-C_1}+\frac{B_2\lambda^2}{\lambda^2-C_2} \quad (2.2)$$

$$n^2(\lambda)=A+\frac{B_1\lambda^2}{\lambda^2-C_1}+\frac{B_2\lambda^2}{\lambda^2-C_2} \quad (2.3)$$

$$n^2(\lambda)=1+\frac{B_1\lambda^2}{\lambda^2-C_1}+\frac{B_2\lambda^2}{\lambda^2-C_2}+\frac{B_3\lambda^2}{\lambda^2-C_3} \quad (2.4)$$

where λ is wavelength, $n^2(\lambda)$ is the square of the refractive index, the coefficient A, $B_{1,2,3}$ and $C_{1,2,3}$ are the fitted Sellmeier parameters. From the Cauchy model of a reflection film, the refractive indices versus wavelengths are obtained as shown in the Table 2.1. These refractive indices are used for later film thickness measurements.

Table 2.1 Indices of refraction at different wavelength.

wavelength (nm)	300	400	500	600	700	800	900	1000
refractive index n	1.3182	1.3105	1.3067	1.3045	1.3032	1.3024	1.3018	1.3013

2.3.1.2.2 Spin Calibration Curves

Two kinds of substrates were investigated, the Teflon AF film on 0211 glass and the Teflon AF film on Si wafers. The thickness of Teflon AF film on 0211 glass was measured by variable angle spectroscopic ellipsometry through the model fitting calculations. Nine different spots were selected on each substrate. One of the measurements is shown in Figure 2.5. The calculations have four steps. Firstly, the Teflon AF film was analyzed using a Cauchy model of glass in the original software, then adding a Cauchy model of a Teflon AF film on glass built on the previously determined optical parameters. This model will generate theoretical data from 300 to 1700 nm and at multiple angles from 65° to 75°, shown as the red line in Figure 2.5. Second, the measurements are taken from a wavelength range from 300 to 1700 nm and at multiple angles from 65° to 75° by variable angle spectroscopic ellipsometry. Since light travels different paths through the films, the variable angles are measured to improve the confidence of fitting. Third, from the measurements, experimental data were obtained, which gave the blue line shown in Figure 2.5. Finally, a fitting between theoretical data and experimental data was performed as shown in the green line, and the film thickness was calculated from the fitting.
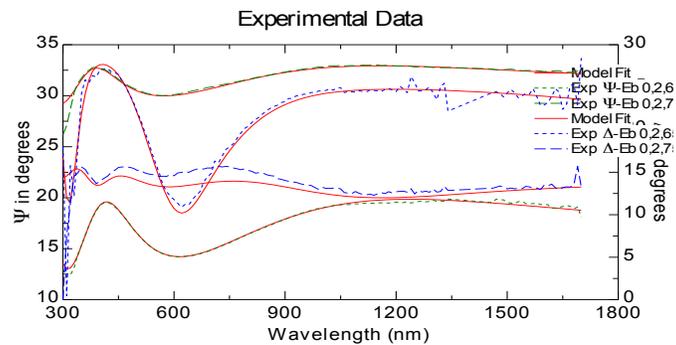
Figure 2.5 Ellipsometry fitting curves. Red represents the theoretically generated data, blue represents the experimentally generated data, and green represents the fitting data.

The thickness of Teflon AF films on Si wafers was measured by a filmetrics resist and dielectric thickness mapping system. This system measures film thickness by analyzing how the film reflects light, which does not work for transparent glass substrates. By inputting the indices of refraction versus the wavelength to the filmetrics resist and dielectric thickness mapping system, the system can automatically map the thickness of the layer over the entire wafer surface area and calculate uniformity. Figure 2.6 shows one of the sample measurements. Color codes represent different thicknesses in which red is the most and purple is the least. The thickness map demonstrates that the Teflon AF film on Si wafers was thicker in the middle point and gets thinner as the radius increases. Under the right-lower corner, the min, max, mean, and standard deviation of the thickness are shown.
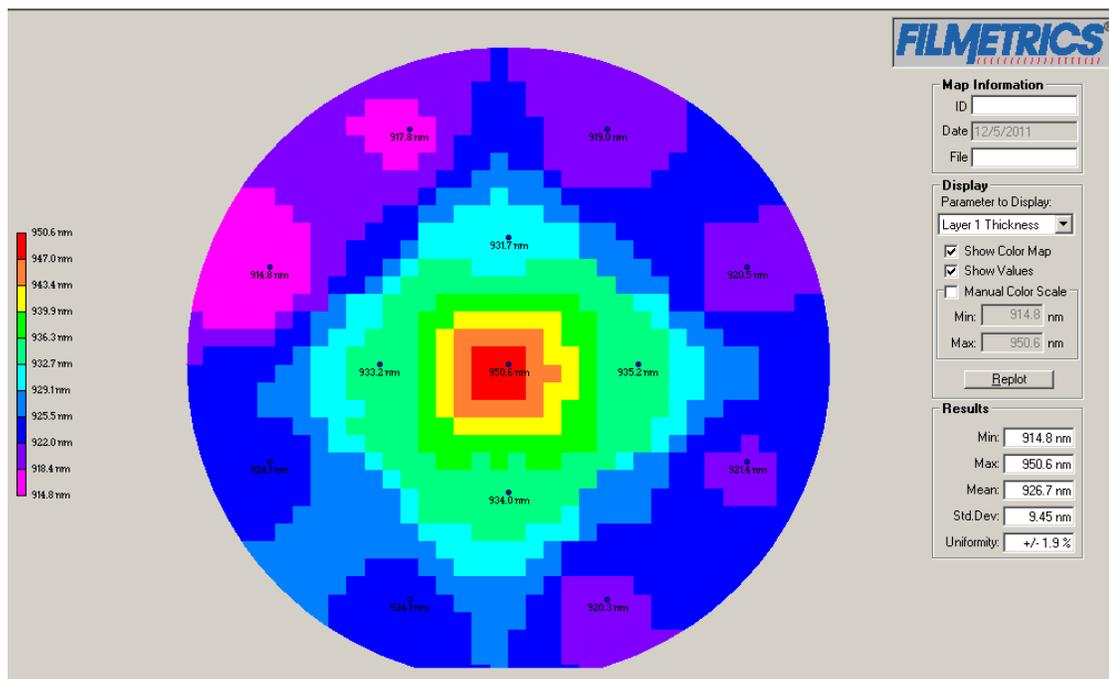
Figure 2.6 Filmetrics mapping. Thickness data shown in the right-lower corner: min=914.8 nm, max=950.6 nm, mean=926.7 nm, standard deviation=9.45 nm.

When 6% Teflon AF in Fluorinert FC-40 was used, the thickness calibration curves were obtained under different spin speeds, as presented in Figure 2.7. For each different spin speed, three replicate substrates were prepared. Figure 2.7.a. was obtained from Teflon AF film on 0211 glass and Figure 2.7.b. was obtained from Teflon AF film on Si wafers. In the calibration curves shown in both Figure 2.7.a. and Figure 2.7.b, the X-axis represents five different spin speeds and the Y-axis represents the Teflon AF film thickness, measured as described above. The inverted triangle symbol represents the minimum thickness on the substrates. The triangle represents the maximum thickness, while the circle represents the mean thickness. At a spin speed of 1000 RPM, the thickness was ~1 μm. When spin speed increased to 2000 RPM, the thickness decreased substantially to ~0.6 μm. Higher spin speeds trended towards a plateau thickness. When Figure 2.7.a. and Figure 2.7.b were compared at high spin speed, from 3000 RPM to 5000 RPM, the Teflon AF films on 0211 glasses were more uniform than on Si wafers with smaller standard deviations, which may be due to the different thickness measurement techniques, as glass was measured with variable angle spectroscopic ellipsometry and Si was measured with a filmetrics resist and dielectric thickness mapping system.
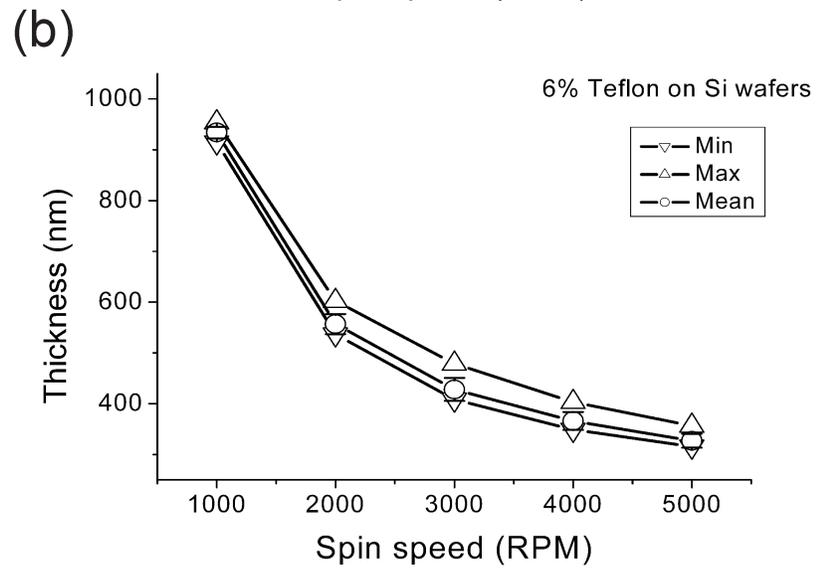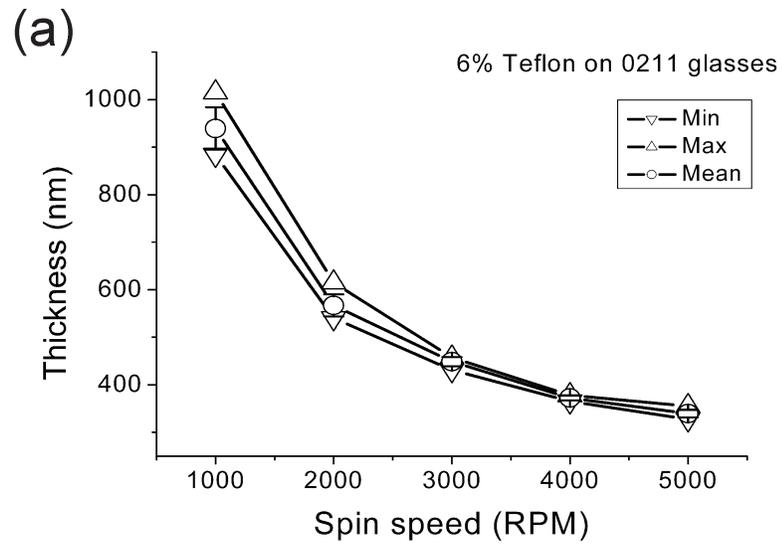
Figure 2.7 Spin speeds curves versus thickness of 6% Teflon AF solution, (a) on 0211 glasses; (b) on Si wafers (n=3).

Since the targeted hydrophobic layer thickness was less than 100 nm, a less concentrated solution, 1% Teflon AF in Fluorinert FC-40 solution, was studied. For each different spin speed, three replicate Teflon on 0211 glass substrates were prepared. The spin curve is shown in Figure 2.8. The thickness decreased almost linearly as the spin speed increased from 2000 RPM to 5000 RPM. 3000 RPM was chosen as the spin speed in the DMF fabrication process, because the standard deviation was minimum and the thickness was in the range to 50 to 70 nm.
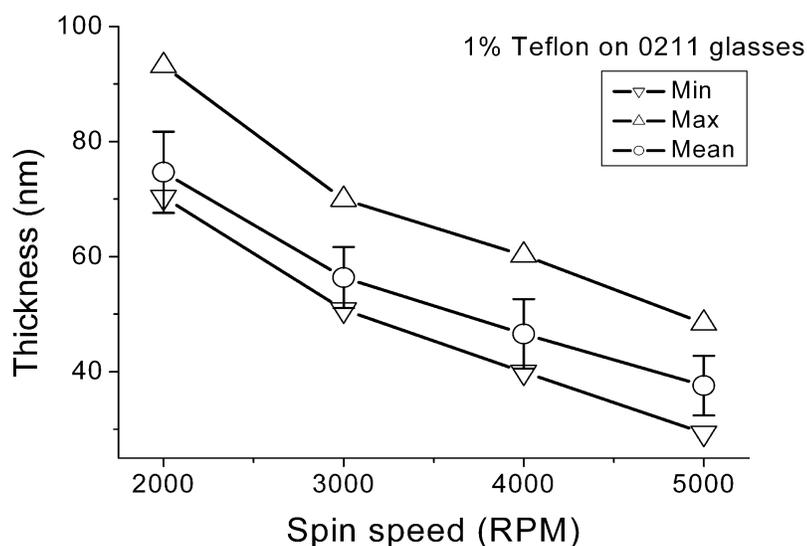
Figure 2.8 Spin speeds curves versus thickness of 1% Teflon AF solution on 0211 glasses (n=3).

2.3.1.2.3 Contact Angles

For a microdroplet on a solid surface as shown in Figure 2.9, at equilibrium, Young's equation $\gamma_{SG}=\gamma_{LG}\cos\theta+\gamma_{SL}$ can be rearranged to get the contact angle $\theta=\arccos\frac{\gamma_{SG}-\gamma_{SL}}{\gamma_{LG}}$.
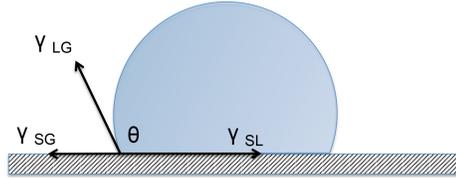
Figure 2.9 Schematic of the surface tension at the contact line. γ_{SG} represents surface tension between solid and gas interfaces, γ_{LG} represents surface tension between liquid and gas interfaces and γ_{SL} represents surface tension between solid and liquid interfaces.

Experimentally, contact angles are determined by image analysis of side views of droplets, as shown in Figure 2.10 when using the contact angle measurement system. The contact angle data was directly obtained from the summary table on the upper left corner in Figure 2.10. In contact angle measurement, fresh DI water was used to prevent contaminants from depositing on the solid surface. Contaminants will cause a change of surface tension between solid and liquid interfaces, and consequently lead to a change of the measured contact angle θ. The contact angle was taken immediately, just when the water droplet sat on the surface, to limit the effects of evaporation.
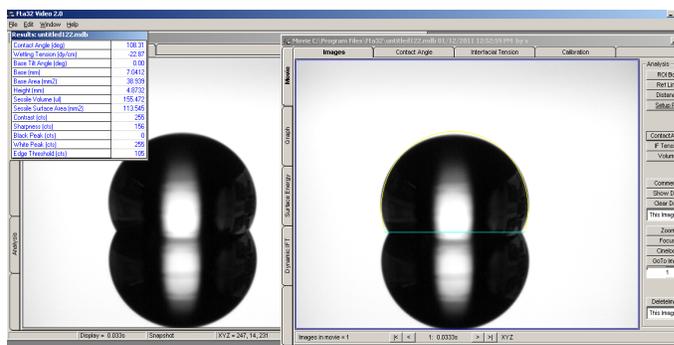
Figure 2.10 Experimental data from contact angle measurement system.

Contact angle plots are shown in Figure 2.11 in which nine different spots on the substrate are measured. Three replicated substrates of 6% Teflon AF solution spin coating on 0211 glass and Si wafers at spin speed of 3000 RPM were measured. The contact angle plots indicate that the Teflon AF film on 0211 glasses and Si wafers were both highly hydrophobic. Contact angles for water droplets on the film were ~110° on Teflon AF films on 0211 glass. Contact angles for water droplets were ~109° on Teflon AF films on Si wafers. The reported Teflon AF films contact angle is ~113°.[45]
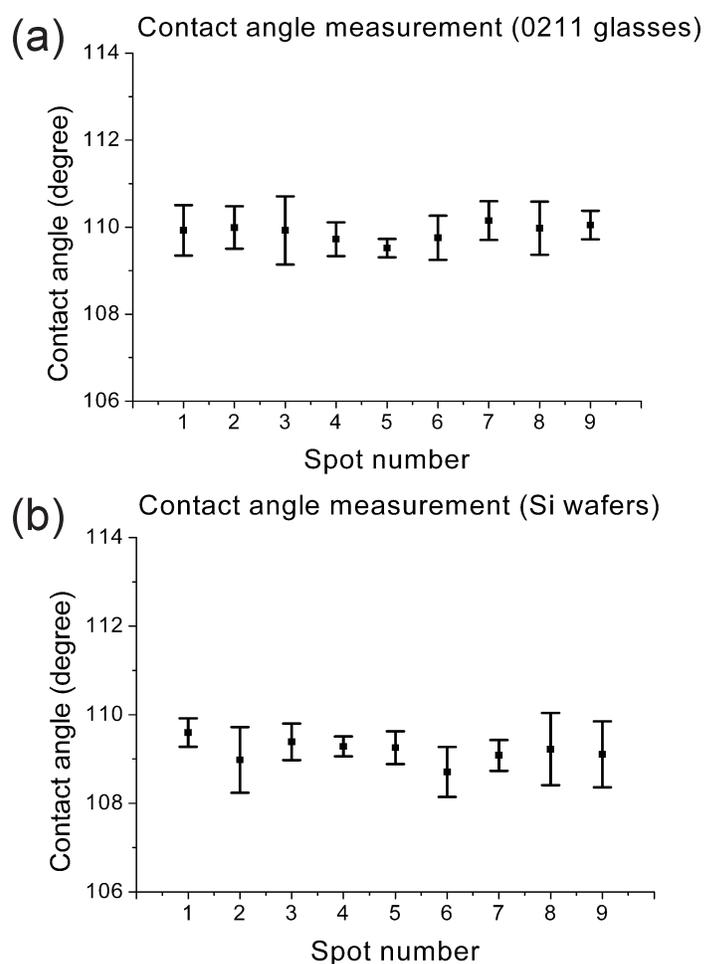
Figure 2.11 Contact angles plot of Teflon AF film (a) on 0211 glasses; (b) on Si wafers (n=3). The measusred water droplet is 5 μL.

To evaluate the contact angle of 1% Teflon AF solution spin coating on 0211 glass substrates under different spin speeds, contact angle calibration curves were obtained as presented in Figure 2.12. In the calibration curve, the X-axis represents four different spin speeds and the Y-axis represents contact angles. The inverted triangle symbols represent minimum contact angles on the substrates, the triangle represent maximum contact angles, while the circles represent the mean contact angles on the substrates. Each group was the measurement of three replicate substrates. At various spin speeds, the contact angles remained the same. Comparing contact angles on different concentrations of Teflon AF films, the contact angles of 1% Teflon AF solution formed films was 2° larger than when using 6% Teflon AF solution. Generally, a reproducibility of ±2° is often considered to represent a good quality of coating.[93]
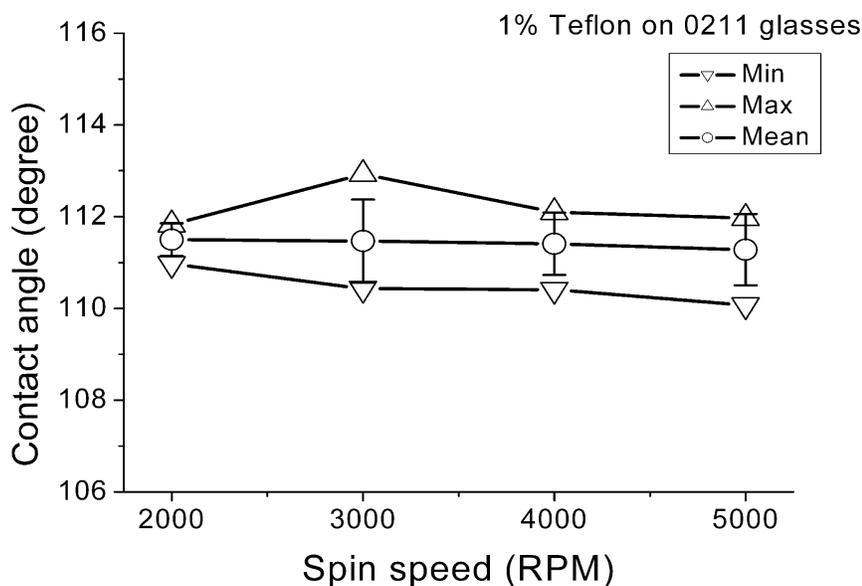
Figure 2.12 Spin speeds curves versus contact angles of 1% Teflon AF solution on 0211 glasses (n=3).

2.3.2 DMF Device Performance

2.3.2.1 Droplet Actuation Control

The two electrode-plate configuration, which limits the evaporation rate, was used in our devices. The instrumental setup is shown in Figure 2.13.a. A 0.4 mm and 0.75 mm thick spacer was used between two plates respectively. A droplet was sandwiched between the bottom actuation electrodes and the top unpatterned electrode plate. Figure 2.13.b. shows the mask design of the device. The device design featured an array of actuation electrodes (1.8 mm × 1.8 mm) with inter-electrode gaps of 4 μm and contact pads (2 mm × 2 mm). An AC electric potential, which was used to reduce analyte molecule adsorption on the surface, was applied to the patterned electrodes via the exposed contact pads. The unpatterned electrode on the other plate was grounded.

(a)

Camera

Chip

$C_{dielectric}$

$C_{droplet}$ $R_{droplet}$

$C_{dielectric}$

DC voltage supply

Function generator

(b)

I-CP
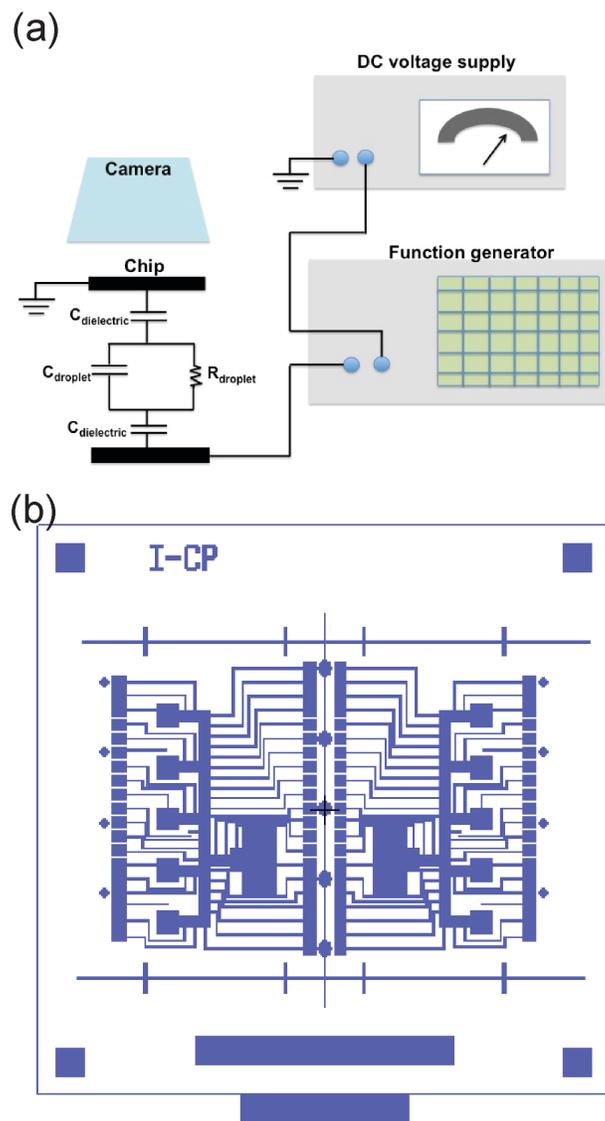
Figure 2.13 (a) Schematic instrumental setup. (b) Mask design of the device: the drawing shows a mask with two devices in mirror image. Small pads and leads are the electrical contacts and pads for voltage delivery. The large squares are the droplet actuation electrodes. A series of reagent storage reservoirs, and a waste reservoir sit off to the side of the main droplet actuation path running along the center of the device.

Once the potential was stepped between the electrodes sequentially, the movement of a droplet was actuated. As shown in the right panel of Figure 2.14, at the moment of T_{V2}, the left actuation electrode, to which V_1 was previously applied, was re-grounded and the middle actuation electrode, which the droplet was on, received a voltage of V_2. At the moment of T_{V3}, the right actuation electrode, which the droplet was just next to, received a voltage of V_3 and the middle actuation electrode, to which V_2 was previously applied, was re-grounded. Through these sequentially controlling steps of V_1, V_2, and V_3, the droplet was transported from the left electrode to the right electrode. The model of virtual displacement was used to explain the EWOD phenomenon, as previously described in Chapter 1.[56] An ideal smooth solid surface was supposed at the contact of a conductive liquid or an electrolyte. When a voltage V is applied between electrodes, the contact angle changes from θ_0 to θ. Lippmann-Young's equation gives

$$\cos\theta-\cos\theta_0=\frac{C}{2\gamma_{LG}}V^2 \quad (2.5)$$

The applied voltage V induces the change of contact angle, which lead to the change of the shape of the droplet and actuates droplet transportation.
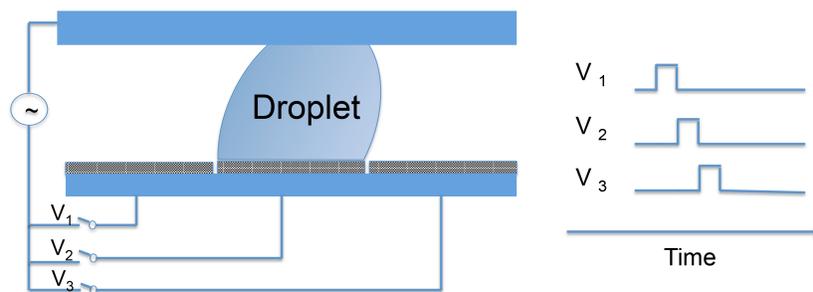
Figure 2.14 Time plots of applied voltages. Through sequentially controlling steps of V_1, V_2, and V_3, the droplet was transported from the left electrode to the right electrode.

2.3.2.2 Droplet Actuation Tests

The droplet actuation tests and spacer height tests were performed for the purpose of optimizing the applied voltage and spacer height. At 0.75 mm spacer height, the theoretically calculated droplet volume, which was treated as a cube, sitting on each actuation electrode was 2.4 μL. In the water droplet actuation test, one 3 μL DI water droplet was dispensed on the chip. This volume was chosen for the reason that the droplet needs to overlap with the edge of the neighboring electrode. To actuate a droplet, the output of a function generator at 500 Hz was amplified to generate 30 V_{RMS} driving potential. In this first test, the DI water droplet did not move. The voltage was increased by 5 V_{RMS} steps to 75 V_{RMS}, where the water droplets started to move. The movability was defined as moving reversibly and repeatedly across electrodes at least three times.

In the spacer height test, the original 0.75 mm height was reduced to 0.4 mm. At 0.4 mm, the theoretically calculated droplet volume sitting on each actuation electrode is 1.3 μL. One 1.5 μL DI water droplet was dispensed, so that the droplet overlapped the edge of the neighboring electrode. To actuate a droplet, a 30 V_{RMS} driving potential at 500 Hz was applied initially. The DI water droplet did not move under this driving potential. Increasing the voltage in 5 V_{RMS} steps showed 75 V_{RMS} was required for the water droplet to start to move. The minimum applied voltage was the same for two different spacer heights. Comparing the droplet transportation rate, which was the velocity of droplet movement observed by eye, between neighboring electrodes, droplets actuated in 0.4 mm spacer height devices moved faster than in 0.75 mm spacer height devices. In our DMF-GLAD interface devices, since the thickness of the GLAD substrate was 0.5 mm, the spacer height of 0.75 mm was selected.

In the analyte droplet actuation test, 1 mg/mL [Des-Arg[9]]-bradykinin stock solution was prepared by reconstituting 1 mg peptide powder in 1 mL DI water. Since the 0.75 mm spacer was used, a 3 µL peptide droplet (1 mg/mL) was dispensed on the chip. To actuate a droplet, a 75 V_{RMS} driving potential at 500 Hz was applied initially, but the peptide droplet did not move. A voltage of 150 V_{RMS} still left the droplet pinned on the original electrode. This may be due to the high concentration of the analyte; therefore, we diluted the stock solution to 0.1 mg/mL with 0.1% TFA. One 3 µL diluted peptide solution droplet was dispensed on the chip. To actuate a droplet, 75 to 150 V_{RMS} driving potential was applied. Only when the driving potential was greater than 120 V_{RMS} did the diluted peptide solution droplet move across electrodes. However, the peptide solution droplet moved at most across four sequential electrodes. We also observed that the liquid interface was distorted when the voltage was applied during the second usage of the chip. This may be due to the adsorption of analyte molecules on the surface after a period of usage.[94]

Reversible and repeated movement was never observed in the analyte droplet actuation experiments. There are three potential reasons to explain why analyte droplets lack repeatability in DMF chips. First, the analytes deposit on surfaces, which cause hysteresis and leads to droplet pinning. Second, since the Teflon spin coating process may cause pinholes of the surface, that could lead to the breakdown of the Teflon AF spin coating layer even when the applied voltage is far below the breakdown potential. Third, due to the adsorption of molecules on the surface, the inhomogeneous surface may lead to

dielectric breakdown phenomena. The breakdown is explained in more detail in the following section.

2.3.3 Minimum Voltage

The experimental observations showed that droplets did not move from one electrode to another as soon as the voltage was applied. This phenomenon can be explained by a minimum actuation voltage. In EWOD devices, the actuation of droplets requires a minimum applied voltage, V_{min}, which is related to the hysteresis contact angle α. For an ideal surface, a unique contact angle for a given solid-liquid-gas three-phase line is given by Young's equation. When a droplet sits on a perfectly smooth, homogenous and horizontal surface, the contact angle θ is defined by Young's equation

$$\gamma_{SG} = \gamma_{LG} \cos\theta + \gamma_{SL} \quad (2.6)$$

However, in practice, careful experiments have shown that there are two relatively reproducible values of the contact angles, one the advancing contact angle θ+α and one the receding contact angle θ_0-α. The difference between these two contact angles has been denoted as contact angle hysteresis α.[95] If the contact angle hysteresis is taken into consideration, the advancing and receding electrowetting line forces are

$$f_{EWOD, \text{advancing}} = \gamma \cos(\theta+\alpha) \quad (2.7)$$

$$f_{EWOD, \text{receding}} = \gamma \cos(\theta_0-\alpha) \quad (2.8)$$

The total electrowetting line force is then

$$f_{EWOD, \text{total}} = f_{EWOD, \text{advancing}} - f_{EWOD, \text{receding}} = \gamma \cos(\theta+\alpha) - \gamma \cos(\theta_0-\alpha) \quad (2.9)$$

It is assumed that the contact angle hysteresis is small. Because α<<θ, so that cosα=1, sinα=α, the equation can be rearranged

$$f_{EWOD,\,total} = \gamma(\cos\theta - \cos\theta_0) - \gamma\alpha(\sin\theta + \sin\theta_0) \text{ (2.10)}$$

At the minimum potential V_{min},

$$f_{EWOD,\,total} \geq 0 \text{ (2.11)}$$

Because the minimum potential corresponds to the linear part of Lippmann-Young's equation,

$$\gamma(\cos\theta - \cos\theta_0) = \frac{C}{2}V_{min}^2 \text{ (2.12)}$$

In the case where α is small, $\sin\theta + \sin\theta_0 = 2\sin\theta_0$, the equation can be simplified

$$V_{min} \approx 2\sqrt{\frac{\gamma\alpha\sin\theta_0}{C}} \text{ (2.13)}$$

Therefore, the minimum actuation potential depends on the capacitance C of the dielectric layer and the hysteresis that is determined by the interfacial properties between the droplet liquid and solid.[95] Therefore, in order to minimize the potential required to actuate droplets, a smaller hysteresis contact angle is preferred. This explains why the surface homogeneity of DMF chips is important, in the sense of minimizing the hysteresis contact angles.

2.3.4 Dielectric Breakdown

The schematic composition of the dielectric layer and hydrophobic layer is shown in Figure 2.15. The parylene C dielectric layer guarantees electrical insulation. The Teflon hydrophobic layer increases the initial contact angles. The thinner the dielectric layer is, the larger capacitance it has, and the lower actuation potential the EWOD devices required. However, this thickness reduction is limited by the dielectric breakdown. When the electric field in the dielectric layer exceeds a limit value, which is called the dielectric strength, breakdown occurs and the electric field frees bound electrons. Dielectric constant and dielectric strength of Teflon and parylene C are listed in Table 2.2. Total capacitance of the DMF devices, C includes the contribution of the dielectric layer, $C_{dielectric}$ (parylene C) and the hydrophobic layer, $C_{hydrophobic}$ (Teflon).

$$\frac{1}{C} = \frac{1}{C_{dielectric}} + \frac{1}{C_{hydrophobic}} (2.14)$$

The order of magnitude of the capacitance for our DMF devices is $C \sim 10^{-8}$ F/m^2. For a perfect homogeneous device, our commonly used design parameters should be able to tolerate the applied voltages without dielectric breakdown. However, defects such as pinholes could greatly reduce the breakdown strength, and may account for the poor reproducibility we observed.

Figure 2.15 Dielectric layer and hydrophobic layer of DMF devices.

Table 2.2 Dielectric constant and dielectric strength of Teflon and Parylene C.

	Dielectric constant	Dielectric strength	Capacitance	Voltage applied
Teflon	2.1	59 V/μm	$\sim 7 \times 10^{-7}$ F/m^2	~ 2 V
Parylene C	3.2	800 V/μm	$\sim 1 \times 10^{-8}$ F/m^2	~ 145 V

2.3.5 DMF-GLAD Device Performance

2.3.5.1 DMF-GLAD Interface

At the DMF-GLAD interface, the droplet was placed on a hydrophobic surface bounded by a Si GLAD surface as shown in Figure 2.16. The Si GLAD surface is hydrophilic. Figure 2.17 a-c shows a sequence of images of a 500 nm thick GLAD film; as originally grown from the top, in a titled view from the surface normal, and along the edge of the film, illustrating the columnar character of separate, individual silicon nano-pillar strands. Due to the highly hydrophilic surface of the Si GLAD film, once the droplet transfers from the edge of the DMF electrode to the edge of the GLAD film, the droplet on the wetting edge would tend to spread into the hydrophilic GLAD surface. Capillary forces on the contact lines between DMF and GLAD interface should stretch the droplet, consistent with results presented below.
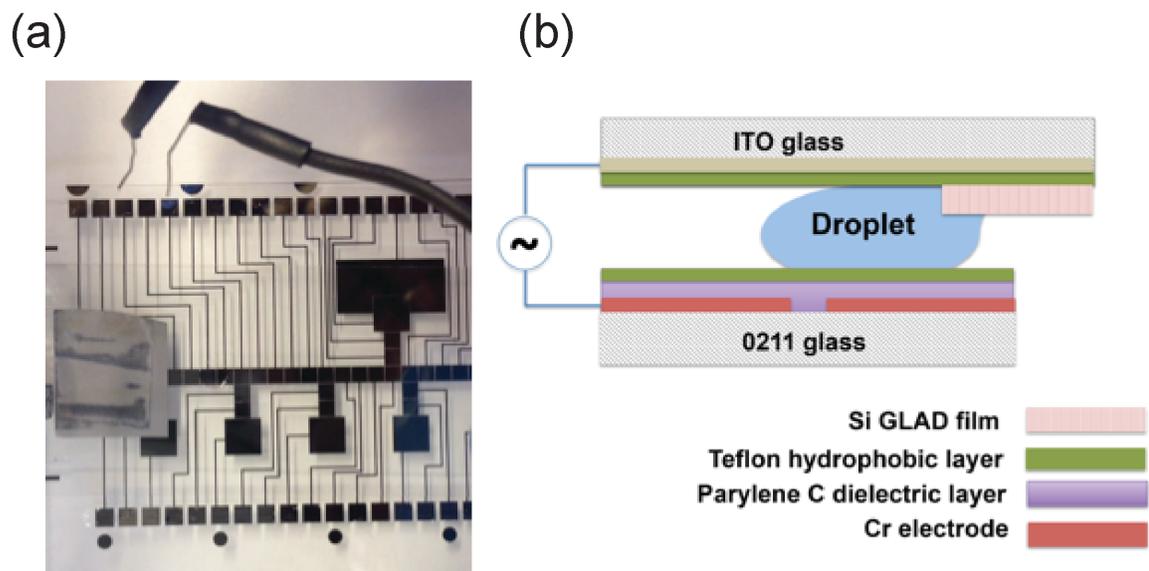
Figure 2.16 (a) Top-view and (b) schematic draw of side view of DMF-GLAD devices.

(a)

U of A   SEI   5.0kV   X50,000   100nm   WD 7.0mm

(b)

U of A   SEI   5.0kV   X30,000   100nm   WD 13.0mm

(c)

U of A   SEI   5.0kV   X50,000   100nm   WD 9.0mm
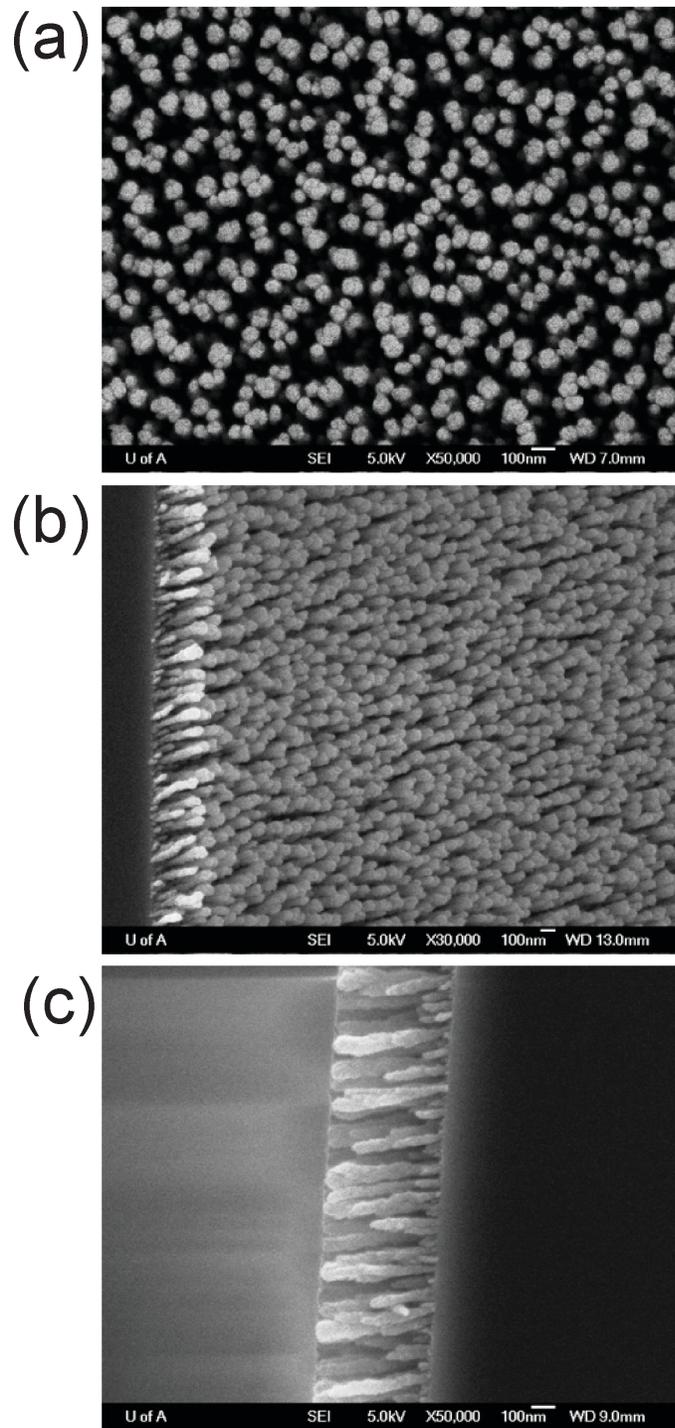
Figure 2.17 SEM images of a 500 nm thick Si GLAD film deposited on a Si substrate with (a) top view; (b) tilted view and (c) side view. The images illustrate the columnar character of separate, individual nano-pillar strands.

2.3.5.2 Peptide Droplet Detection

For each new DMF device, a DI water droplet was used to test the quality of the chips. The spacer height was 0.75 mm and one 3 µL DI water droplet was dispensed on the chip that overlapped the edge of the neighboring electrode. To actuate a droplet, 75 V_{RMS} driving potential was applied at 500 Hz. Four out of five devices were in good condition, in which a DI water droplet can move reversibly and repeatedly across electrodes at least three times. These devices were chosen for further peptide solution droplet actuation. One 3 µL [Des-Arg^9]-bradykinin diluted peptide solution droplet (0.1 mg/mL) was dispensed on the chip. To actuate a droplet, 120 V_{RMS} was applied at 500 Hz. Once the droplet touched the edge of the GLAD film, the droplet was immediately withdrawn by the GLAD film. The Si GLAD film was separated from the DMF device and attached to a modified MALDI plate for matrix-free laser desorption/ionization mass spectrometry.

Mass spectrometry measurements were performed on a time-of-flight mass spectrometer. Positive ion mode mass spectra were acquired, as in Figure 2.18. The film provided a low background mass spectrum at low mass range and produced a high signal-to-noise ratio and low chemical background spectrum containing the [Des-Arg^9]-bradykinin molecular ion at m/z 902.9.
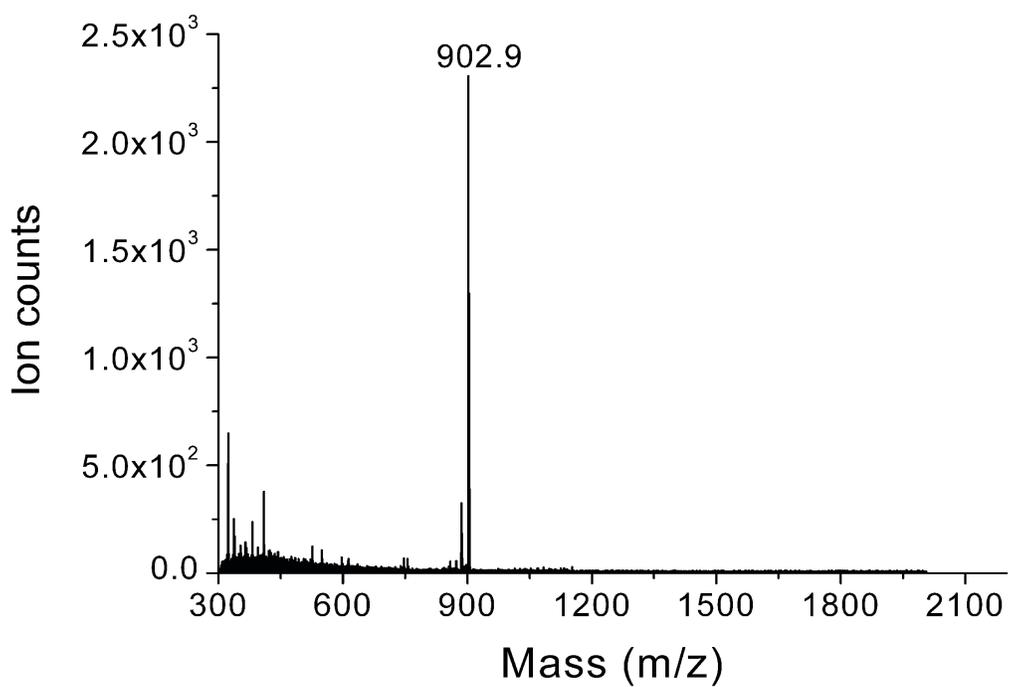
Figure 2.18 [Des-Arg[9]]-bradykinin (m/z=902.9) detected by DMF-GLAD SMALDI. Mass spectrum was obtained in positive ion mode.

2.4 Conclusion

This study has demonstrated the feasibility of coupling Si GLAD film with DMF devices for matrix-free detection of peptide molecules by SMALDI. We have fabricated DMF devices for droplets transportation. Teflon AF film thickness and contact angles against spin speed calibration curves were obtained. Although we cannot obtain good repeatability of the DMF devices, the results still show the potential of DMF-GLAD interface for SMALDI detection. The potential advantage of this interface includes carrying out sequential chemical processing by using DMF device, which is less laborious. Since other researchers report reproducible DMF devices, the applications appear meaningful, if still challenging.

Chapter 3 Ready-to-use Immobilized-Tryptic Digestion Si GLAD Films for Peptide Mass Fingerprinting

3.1 Introduction

Enzymatic digestion of proteins to be analyzed, coupled with separation and mass spectrometry are the common steps in peptide mass fingerprinting (PMF).[96] Traditionally, protein digestion is performed in solution by free enzyme, with a small amount of enzyme added to the protein solution, leading to long incubation times (typically 5-24h). In recent years, protein digestion by enzymes immobilized on solid supports, which can achieve efficient digestion in a shorter time in immobilized enzyme reactors (IMERs), has gained in popularity. One of the most striking features of IMERs is that coupling to a separation and identification system enables high-throughput, automated proteome profiling.[69] In general, IMERs can be coupled with capillary electrophoresis (CE)[71, 72] or high-performance liquid chromatography (HPLC)[73, 74, 97] for separation. IMERs can be coupled on-line with electrospray ionization mass spectrometry (ESI-MS)[70, 76, 77] or off-line with matrix-assisted laser desorption/ionization mass spectrometry (MALDI-MS)[78, 79] for protein identification. Although on-line coupling with MALDI-MS can be also achieved, it is less developed. Ekstrom *et al.* described a microchip IMER that interfaced to a MALDI target plate for automated MALDI-MS analysis.[78] Xu *et al.* studied *in situ* digestion of proteins on a tryptic modified porous silicon (Si) surface, with detection by MALDI, and concluded that the modified protein surface is not suitable for the digestion and detection of peptide residues, unless matrix is added to improve the desorption/ionization efficiency.[79]

Recently our group demonstrated nanostructured glancing angle deposition (GLAD) fabricated Si thin films for solid matrix laser desorption/ionization mass spectrometry (SMALDI-MS), for applications such as peptide detection.[22] Since the Si nanopillars were oxidized to allow silane chemistry to be used for the attachment of enzymes, the Si GLAD films offer an opportunity for rapid PMF by SMALDI-MS within the same IMER experimental class. In this chapter, a simple IMER proteolysis platform of immobilized-tryptic-digestion GLAD films was developed. The immobilization of trypsin, which has a number of potential immobilizing sites including the ε-amino groups of lysine, was achieved through one-step reaction with 3-glycidoxypropyl trimethoxysilane (GPTMS) functionalized Si GLAD surfaces, which provide reactive epoxy groups. The target protein, cytochrome c (~40 pmol), was deposited on the modified films and the digests were detected by SMALDI-MS. Comparisons between immobilized-tryptic digestion and free solution digestion, with detection by SMALDI-MS were performed.

The work presented in this chapter was in collaboration with Dr. Michael Brett's group in the Department of Electrical and Computer Engineering at the University of Alberta. Steven Kim Jim assisted with the growth of the GLAD films.

3.2 Experimental Section

3.2.1 Chemicals and Reagents

All solvents were analytical grade. Ultrapure water was prepared with a deionizing system (Millipore Canada, Mississauga, ON, Canada). MALDI matrix (α-cyano-4-hydroxycinnamic acid, HCCA), trypsin from bovine pancreas, cytochrome c from horse heart (M.W.=12,384 g/mol), angiotensin II (M.W.=1046 g/mol), 3-aminopropyltriethoxysilane (APTES), glutaraldehyde (GA), 3-glycidoxypropyl trimethoxysilane (GPTMS), methanol (MeOH), ammonium bicarbonate (NH_4HCO_3), trifluoroacetic acid (TFA), monosodium phosphate and disodium phosphate were purchased from Sigma-Aldrich. Si wafers (Test Grade, 10 cm diameter, University Wafer, Boston, MA, USA) and evaporated material, Si (CERAC, Inc., Milwaukee, WI, USA) were used in the GLAD fabrication process.

3.2.2 Si GLAD Films Preparation

3.2.2.1 Si Wafer Cleaning

Si wafer substrates were cleaned prior to deposition by hot piranha solution (H_2SO_4: H_2O_2, v: v/1:3) for 15 min, followed by distilled water rinsing and drying with nitrogen. Piranha is highly reactive and can become extremely hot when prepared, so care must be taken. We prepared this solution by adding hydrogen peroxide to sulfuric acid very slowly. We handled piranha solution by using the wet deck in the University of Alberta NanoFab (Edmonton, AB).

3.2.2.2 Electron Beam Deposition

Cleaned Si wafers were cut in half by a diamond stylus and mounted onto a deposition chuck. The deposition chuck was loaded into a high vacuum electron-beam deposition system (AXXIS, Kurt J. Lesker Co., Clairton, PA, USA). Si vertical posts of 500 nm were deposited using GLAD at an angle of 86° relative to the substrate normal, using a substrate rotation rate of 1.2 RPM at a deposition rate of 0.4 to 0.9 nm/s.

3.2.3 GLAD Films Characterization

3.2.3.1 Scanning Electron Microscopy

Scanning Electron Microscopy (SEM) images were taken of chromium coated samples using a JEOL 6301F field emission scanning electron microscope. Working distances and accelerating voltages used to obtain images are listed at the bottom of each image. Chromium coated specimens were coated with an Edwards Xenosput XE 200 coater.

3.2.3.2 X-ray Photoelectron Spectroscopy

The X-ray Photoelectron Spectroscopy (XPS) measurements were performed on AXIS Ultra spectrometer (Kratos Analytical) at the Alberta Centre for Surface Engineering and Science (ACSES), University of Alberta. The base pressure in the analytical chamber was lower than 4×10^{-8} Pa. Monochromatic Al Kα source (hν = 1486.6 eV) was used at a power of 210 W. The analysis spot was 300 μm × 700 μm. The resolution of the instrument is 0.55 eV for Ag 3d and 0.70 eV for Au 4f peaks. The survey scans were collected for binding energy spanning from 1100 eV to 0 with analyzer pass energy of

160 eV and a step of 0.4 eV. For the high-resolution spectra the pass-energy was 20 eV with a step of 0.1 eV. The number of scans varied from 8 to 30 to get reasonable signal to noise ratio. Electron flood neutralizer was applied to compensate sample charging.

3.2.4 Trypsin Immobilization Procedures

3.2.4.1 APTES-GA Approach

Si GLAD films were cut into 6 mm × 6 mm pieces by diamond stylus. The film surfaces were functionalized by immersing the Si GLAD films in APTES solution (1% v/v in toluene) for 20 min at ambient temperature (~22°C) followed by immersing in GA (2.5% v/v in water) for an hour at ambient temperature. The modified Si GLAD films were water rinsed and subsequently immersed in trypsin solution (1 mg/mL), which was freshly prepared by constituting lyophilized samples in phosphate buffer (50 mM, pH 7.0), and kept at 4°C for overnight. The immobilized-tryptic digestion GLAD films were washed with water to remove unreacted trypsin before use.

3.2.4.2 GPTMS Approach

Si GLAD films were cut into 6 mm × 6 mm pieces by diamond stylus. Prior to linking trypsin to the Si GLAD films, the film surfaces were functionalized by immersing the Si GLAD films in GPTMS solution (1% v/v in methanol) for 20 min at ambient temperature. The silylated Si GLAD films were rinsed with methanol to remove physically absorbed silane and subsequently immersed in the trypsin solution (1 mg/mL) at 4°C for overnight

as described above. The immobilized-tryptic digestion GLAD films were washed with water to remove unreacted trypsin before use.

3.2.5 Digestion Samples Preparation

3.2.5.1 Free Solution Digestion

Trypsin was dissolved at concentrations of 0.1 and 0.5 mg/mL in water. Cytochrome *c* was dissolved at concentrations of 1 and 0.5 mg/mL in ammonium bicarbonate buffer (20 mM, pH 7.9). Free solution digestion was performed by mixing 10 µL trypsin and 10 µL cytochrome *c* under conditions optimized previously,[98] with a trypsin to cytochrome *c* ratio of 1: 10, at 37°C. MALDI matrix solution was prepared by dissolving 5 mg/mL of HCCA in a mixture of acetonitrile/0.1% TFA (v/v, 50/50). 1 µL of the free solution digest sample and 9 µL of the matrix solution were mixed then deposited and dried for MALDI-MS.

3.2.5.2 Digestion on Immobilized-Tryptic Digestion GLAD Films

Cytochrome *c* was dissolved at concentrations of 1 and 0.5 mg/mL in ammonium bicarbonate buffer. A 5 µL aliquot of cytochrome *c* was deposited onto the immobilized-tryptic digestion GLAD film surfaces. The films were placed inside a humid chamber to slow down the evaporation of the buffer solution during the digestion. The digestion reaction was quenched by adding 5 µL 0.1% TFA.

3.2.6 Mass Spectrometry

Mass spectrometry measurements were performed on an Applied Biosystems Voyager STR time-of-flight mass spectrometer (Framingham, MA, USA). A pulsed N_2 laser at a wavelength of 337 nm was operated at a repetition rate of 3.0 Hz. Positive ion mode mass spectra were acquired under the following conditions. The reflector, delayed extraction mode was used. An accelerating potential of 20 kV, a 74% grid potential, a 0.07% guide wire voltage and a delay time of 350 nsec was applied. Each spectrum is the result of 200 laser shots. The MS data recorded were processed by Voyager Data Explorer version 4.0 (Applied Biosystems, Framingham, MA, USA).

Free solution digestions were analyzed by both MALDI-MS and SMALDI-MS. In MALDI analysis, 0.6 µL of the analyte-matrix mixture was deposited onto a MALDI plate. In SMALDI analysis, 0.6 µL of free solution digestion sample was deposited onto a bare Si GLAD film, which was then attached to a modified MALDI plate by conductive double-sided tape as described in our previously published work[22]. The immobilized-tryptic digestion films were directly attached to a modified MALDI plate by conductive double-sided tape, after quenching the reaction with 0.1% TFA. The film was washed by water twice, each time 5 µL water was pipetted on the surface, allowed to stay for 5 sec, followed by nitrogen blowing to drive off the droplet. After simple washing step, the film was ready for SMALDI.

3.3 Results and Discussion

3.3.1 Trypsin Immobilization Approaches

Effective immobilization of trypsin is a critical step in designing a reactive surface for protein digestion. Many different immobilization schemes are possible.[69] In this work two were selected, which have been used previously to immobilize trypsin on surfaces.[99] The abundant surface silanol groups (-SiOH) present on the Si GLAD film are the basis for the surface modification. One of these approaches is a classic two-step APTES-GA based approach, in which APTES is reacted with GA and the trypsin binds to the surface. This reaction can be quite effective, but the high reactivity of GA with amines can result in reactions that impair the trypsin function. An alternative method was also tested, utilizing one-step silanization with GPTMS, which directly immobilizes the reactive epoxide on the surface, and then reacts with a more limited subset of amines on the trypsin. The conjugation of trypsin onto the differently functionalized Si GLAD surfaces is further demonstrated based on its digestion of cytochrome *c*.

3.3.1.1 APTES-GA Approach

The net result of immobilization of trypsin by the APTES-GA approach was a surface with marginal or no activity, despite multiple attempts. The SMALDI mass spectrum for the digestion of cytochrome *c* solution (5 µL, 1 mg/mL) on the APTES-GA approach modified GLAD films was acquired under positive ion mode as shown in Figure 3.1. Peak m/z 617.7 was from intact cytochrome *c*, which is explained in the following section. There was no cytochrome *c* digest peak. An analysis was performed to determine where this procedure might have failed.
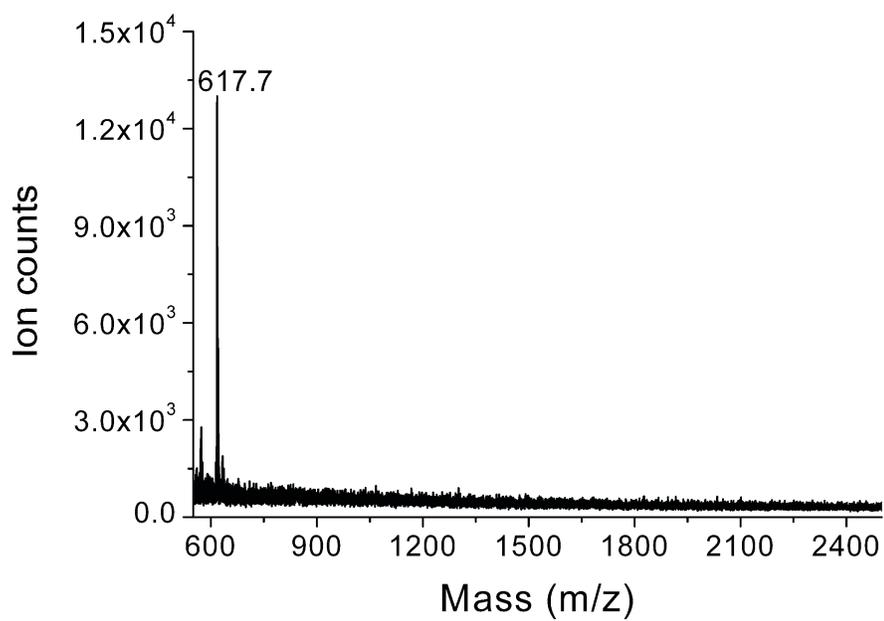
Figure 3.1 Mass spectrum (positive ion mode) of the digestion on the APTES-GA approach immobilized-tryptic digestion GLAD films. Peak m/z 617.7 was from intact cytochrome *c*.

3.3.1.1.1 XPS of APTES Functionalized Surfaces

Surface sensitive XPS was used to analyze the effect of silicon/silica surface treatment with APTES. Atomic concentrations of oxygen (O 1s), nitrogen (N 1s), carbon (C 1s) and silicon (Si 2p) on the APTES functionalized Si GLAD film surfaces were measured using XPS. Atomic concentrations before and after modification are presented in Table 3.1. The atomic C to N ratio was most informative for characterizing the modified surface, as the Si and O present largely derives from the silicon/silica substrate. Compensating for the blank background via $(C_{mod}-C_{blank})/(N_{mod}-N_{blank})$ gave a ratio of 4.07:1 for the APTES modified surface. The molecule itself has a C/N ratio of 9:1, while for fully hydrolyzed APTES attached to a silica surface the ratio is ideally 3:1. Consequently, the observed ratio indicates good coverage of APTES on the surface, with reasonably complete hydrolysis of the ethoxy-silicon bond, showing the first immobilization step was successful.

Table 3.1 Quantitation report of XPS.

	Blank	Modified Surface
Peak	Atomic Concentration (%)	Atomic Concentration (%)
O 1s	51.90	41.76
N 1s	0.00	3.44
C 1s	16.52	30.51
Si 2p	31.58	24.29

3.3.1.1.2 Sensitivity of APTES and APTES-GA Modified Surfaces

The APTES surface was then reacted with GA, which is highly reactive to primary amines, and serves as a cross linker between enzymes and the APTES surface.[100] Following this reaction, the SMALDI activity of APTES and APTES-GA modified surfaces were evaluated with 100 pmol angiotensin II deposited on the films, as shown in Figure 3.2.a-b. Mass spectra of angiotensin II at an m/z 1045.5 on the APTES modified

surface showed good signal strength at ~5.3×10⁴ ion counts. However, there were less

than 5×10^3 ion counts for angiotensin II on the APTES-GA modified surface. The reason

for this reduced sensitivity after the glutaraldehyde linkage step is not entirely clear. The

terminal amine of angiotensin II may also have reacted with the GA on the modified

surface, reducing potential signal strength. However, since only ~40 pmol cytochrome c is

to be digested and analyzed, it is not surprising that the APTES-GA modified GLAD

films were not effective with this reduced sensitivity.
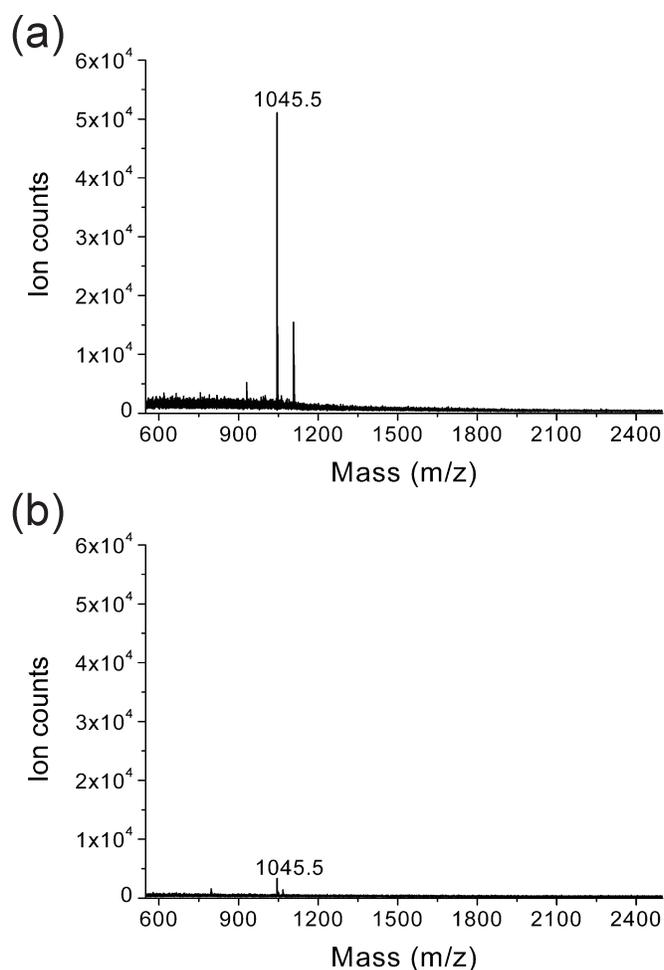
Figure 3.2 (a): 100 pmol angiotensin II (m/z=1045.5) deposited on APTES modified Si GLAD film; (b): 100 pmol angiotensin II (m/z=1045.5) deposited on APTES-GA modified Si GLAD film. Mass spectra obtained under positive ion mode.

3.3.1.2 GPTMS Approach

The surface chemistry for attachment using GPTMS is illustrated in Scheme 3.1. This scheme successfully immobilized active trypsin on the Si GLAD film surface, with the first spectra obtained for ~40 pmol cytochrome *c* showing peaks with m/z of 1167 and 1632 at low intensity. These are expected fragment peaks but optimization to improve the signal strength was required.
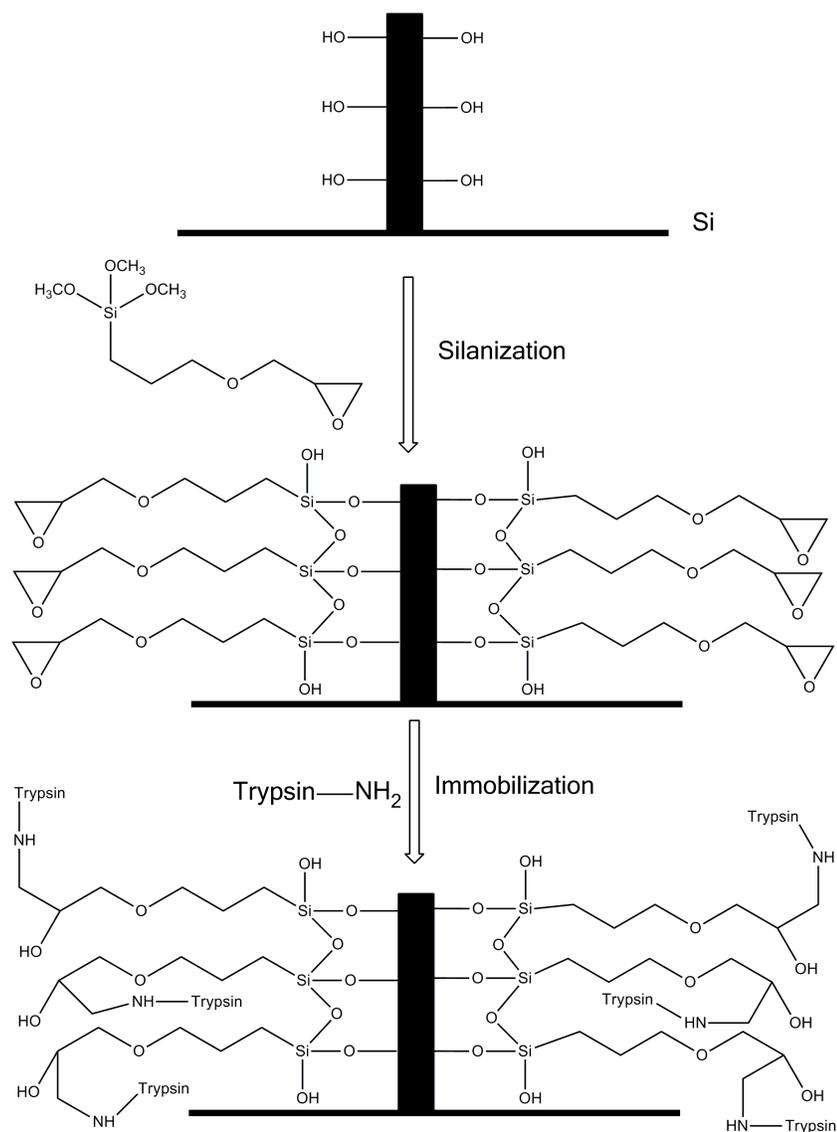
Scheme 3.1 Schematic of the immobilization of trypsin onto the Si GLAD film nanopillars.

3.3.1.2.1 Solvent Choices

An initial problem was that after digestion on the GPTMS immobilized-tryptic digestion films, cracks would appear on the films, as shown in Figure 3.3.a, leading to unrepeatable experimental results. The cracking was resolved by switching solvents from toluene to methanol. We postulate that the increased surface tension of methanol relative to toluene helped reduce stresses in the hydrophilic Si GLAD film during the solvent evaporation stage, as shown in the bottom six pieces in Figure 3.3.b.
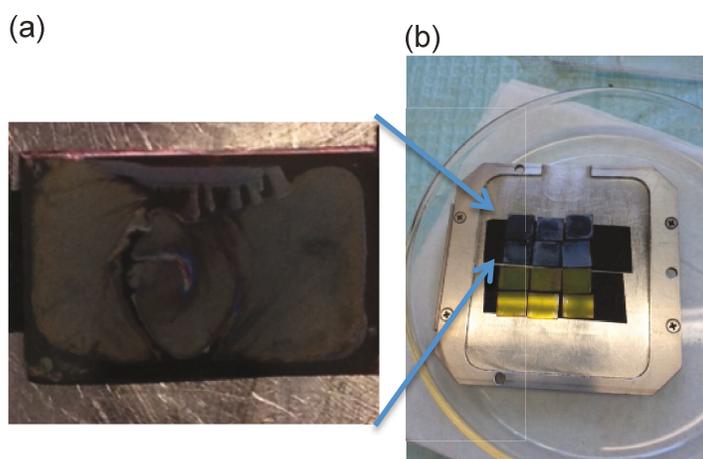
Figure 3.3. (a) Cracks on the immobilized-trypsin digestion film, (b) top six pieces with and bottom six piece without cracks

3.3.1.2.2 Nanostructures of GLAD Films

Treatment of GLAD films with liquids that subsequently evaporate is known to change the structure and orientation of nanopillars within GLAD films.[29] Figure 3.4.a-c shows a sequence of images of 500 nm thick bare Si GLAD films; a) as originally grown from the top, b) as a tilted view from the surface normal, and c) along the edge of the film, illustrating the columnar character of separate, individual silicon nano-pillar strands. Figure 3.5.a-c shows the same three angular views for a Si GLAD film that has been

modified with GPTMS. Treatment with the GPTMS derivatizing solution can be seen to induce clumping of the columnar pillars, with an increase in the pore space between clumps, and less space within a clump. Figure 3.6.a-c shows the same three angular views for a Si GLAD film that has been modified with GPTMS-trypsin, following digestion of cytochrome c, and subsequent mass spectral analysis of the sample. The further chemical treatment, consisting of application of sample, and nitrogen blow before sample analysis, causes further restructuring of the surface. Matting of the clumps into larger aggregates, with the columns standing about 45 degrees to the vertical, and with gaps between clumps are all observed. Matting of nanotubes and nanorod surfaces with high surface areas and high aspect ratios on exposure to liquids and subsequent evaporation has been reported, and referred to as a "nano-carpet effect".[101] Our observation of the structural changes indicate that the more matted a nano-porous surface becomes, approaching the look of planar, entangled cellulose strands like in paper, versus more vertical, pyramidal clumps, the less likely the surface is to volatize ions under laser ablation. Previous work has shown that the more fragile the film the greater the effect of solvent evaporation on the original columnar structure, unless steps like critical point evaporation are utilized. Consequently, while our GPTMS immobilized-tryptic digestion GLAD films are effective as prepared, it is possible that reducing the amount of clumping using critical point drying techniques, or variations in the surface tension of the solvents employed, could improve performance further.
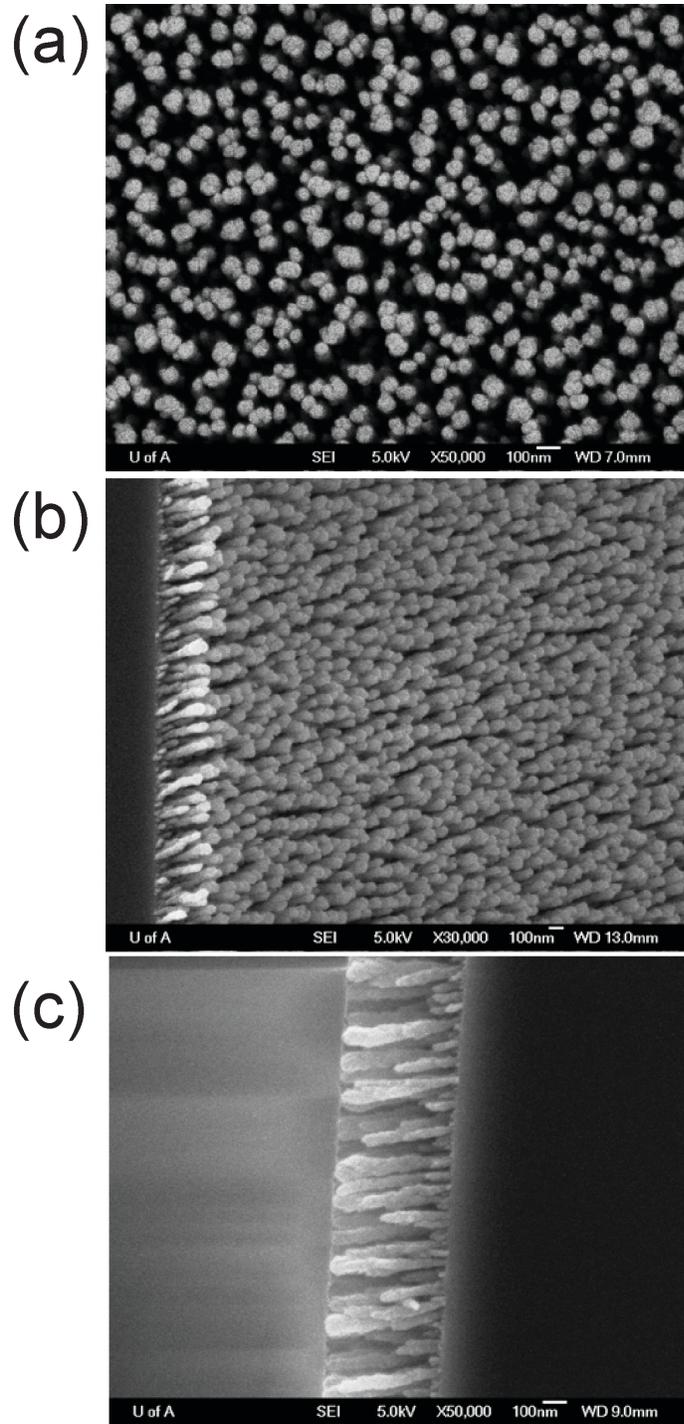
Figure 3.4 SEM images of a 500 nm thick bare Si GLAD film deposited on a Si substrate with (a) top view, (b) tilted view and (c) cross view. It repeats Figure 2.17.
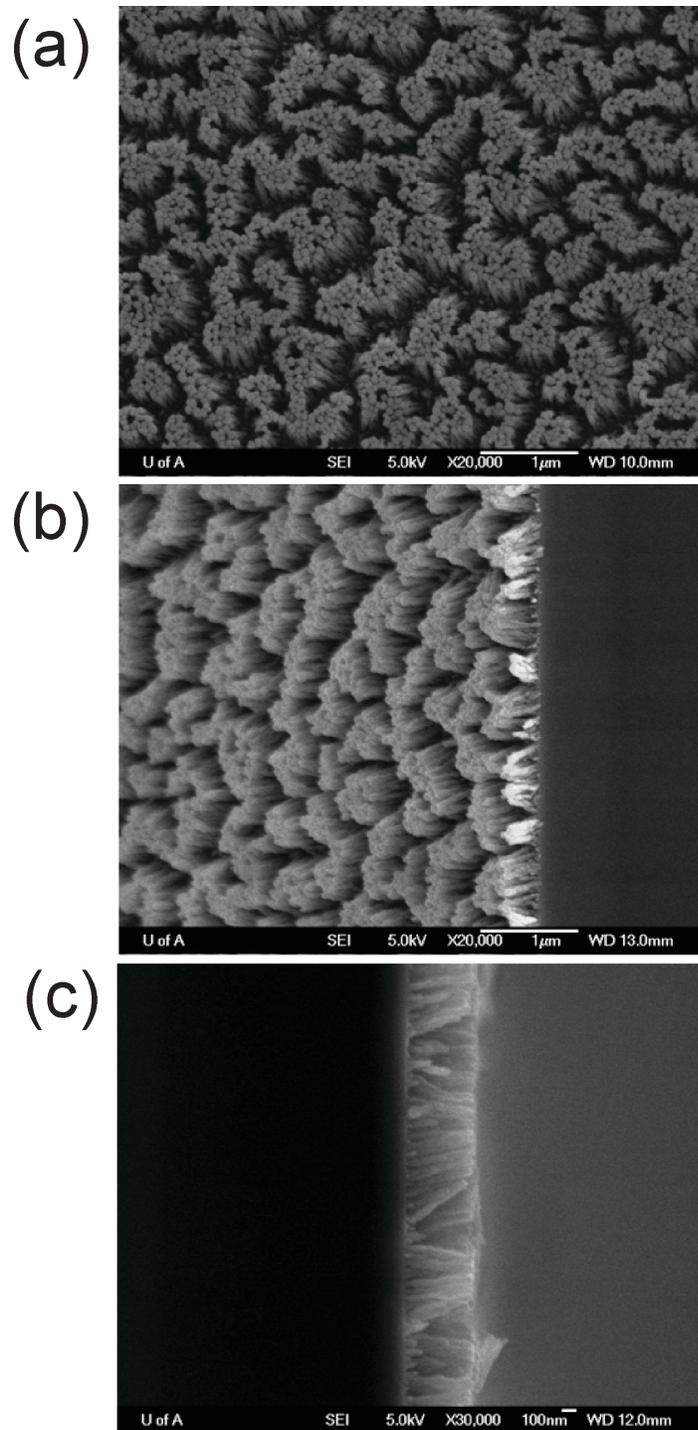
Figure 3.5 SEM images of a 500 nm thick Si GLAD film functionalized with GPTMS with (a) top view, (b) tilted view and (c) cross view.
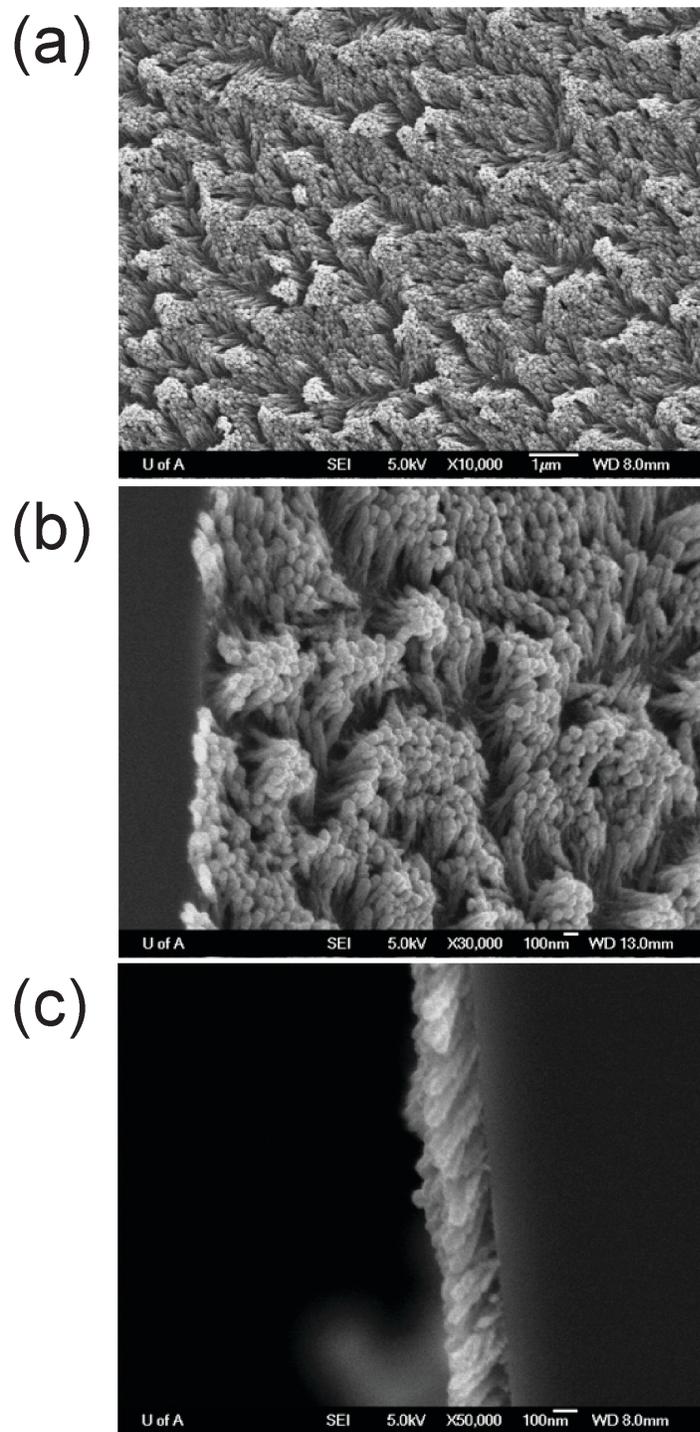
Figure 3.6 SEM images of GPTMS-trypsin modified films, following digestion of cytochrome *c*, and subsequent mass spectral analysis of the sample with (a) top view, (b) tilted view and (c) cross view.

3.3.2 Control Studies

Three controls were performed to confirm the assignment of the above results to immobilized trypsin activity.

A solution of cytochrome c (5 μL of 1 mg/mL) was deposited on a bare Si GLAD film, producing ions at m/z 616.5 and 572.5 as shown in Figure 3.7, both characteristic of ion fragments of cytochrome c formed in the gas phase. The peak at m/z 616.5 arises from the heme fragment of the protein, which rearranges to the iron protoporphyrin IX, as shown in Figure 3.8.[102]
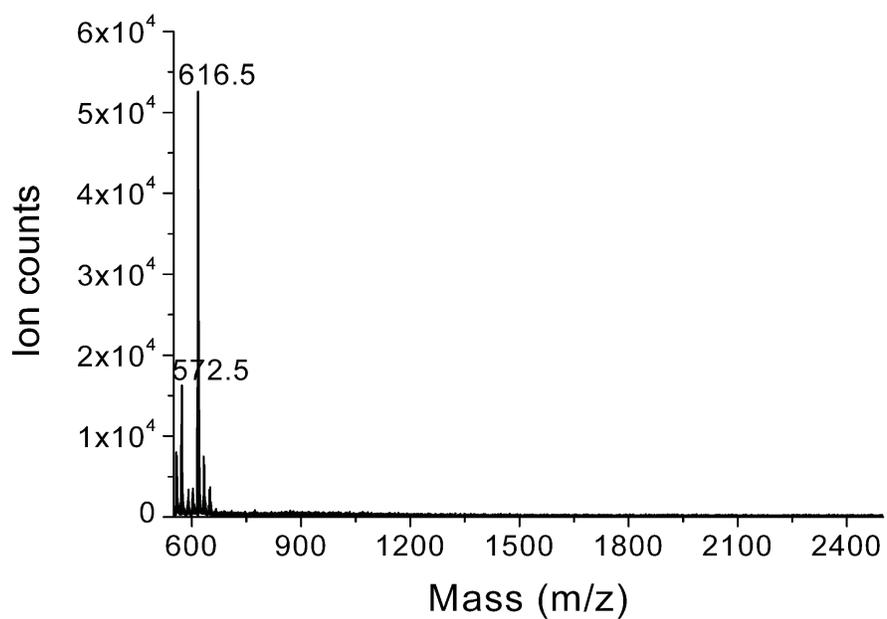
Figure 3.7 Mass spectra (obtained under positive ion mode) of cytochrome *c* on bare Si GLAD films. Peak m/z 616.5 arises from the heme fragment of the intact protein.
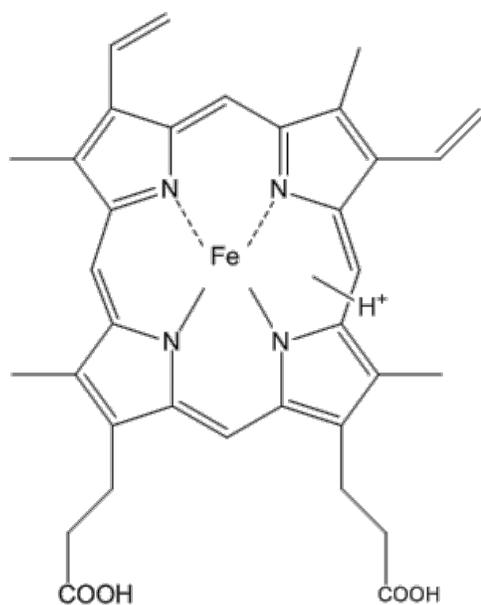
Figure 3.8 Structure of iron protoporphyrin IX.[102]

When 5 μL of 1 mg/mL trypsin solution was deposited on a bare Si GLAD film, peaks

were observed at m/z 658.8, 804.7 and 1045.6 as shown in Figure 3.9, corresponding to

known trypsin autolysis peaks.[103]
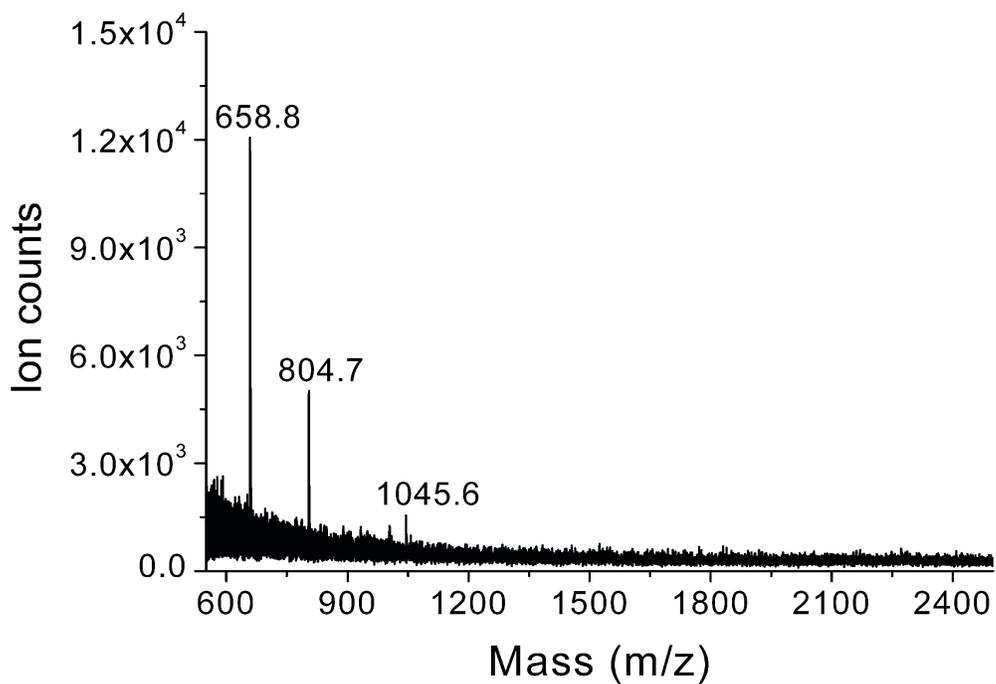
Figure 3.9 Mass spectra (positive ion mode) of trypsin on bare Si GLAD films. Peaks m/z 658.8, 804.7 and 1045.6 corresponding to known trypsin autolysis peaks.

Since the method we developed was a covalent-immobilization method, we also tested how physical adsorption would affect the digestion. The same procedure of trypsin-linkage step described in the experimental section was used in this control experiment, except that the soaked film was a bare Si GLAD film instead of a GPTMS functionalized film. A 5 μL 1 mg/mL cytochrome c solution was pipetted onto the film and the reaction was quenched after 2 hr. As shown in Figure 3.10, only a peak with m/z 617.6 was observed, which was from intact cytochrome c as explained previously. These control experiments confirm the assignment of the above results to immobilized trypsin activity.
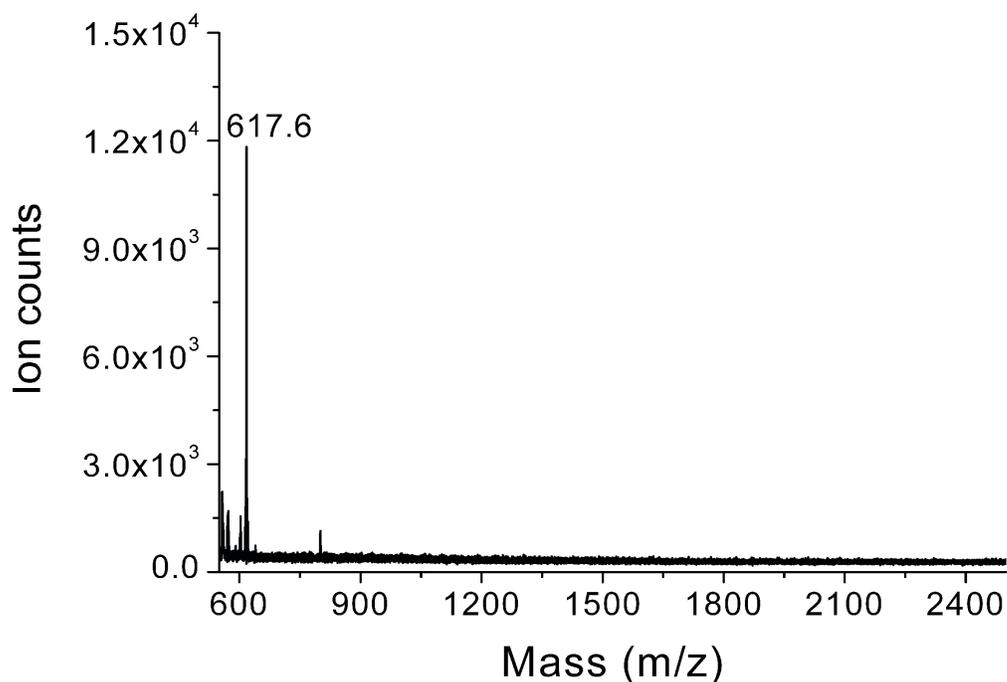
Figure 3.10 Mass spectra (positive ion mode) of non-physically adsorption immobilized-tryptic digestion control. Peak m/z 617.6 was from intact cytochrome c.

3.3.3 Digestion Reaction Optimization

The effect of pH and temperature on the digestion of cytochrome *c* by the GPTMS immobilized-tryptic digestion GLAD film surfaces was evaluated with three repetitive experiments. The buffer was 20 mM NH_4HCO_3 at pH 7.9, mixed with various amount of 1% TFA to adjust pH to lower values, of pH 7.5 and 7.7, while temperatures of ambient (~22°C) and 37°C were explored. The figures of merit were peak height ratios of the fragment ions and the protein sequence coverage. A representative mass spectrum at pH 7.9, and 37°C, is shown in Figure 3.11.
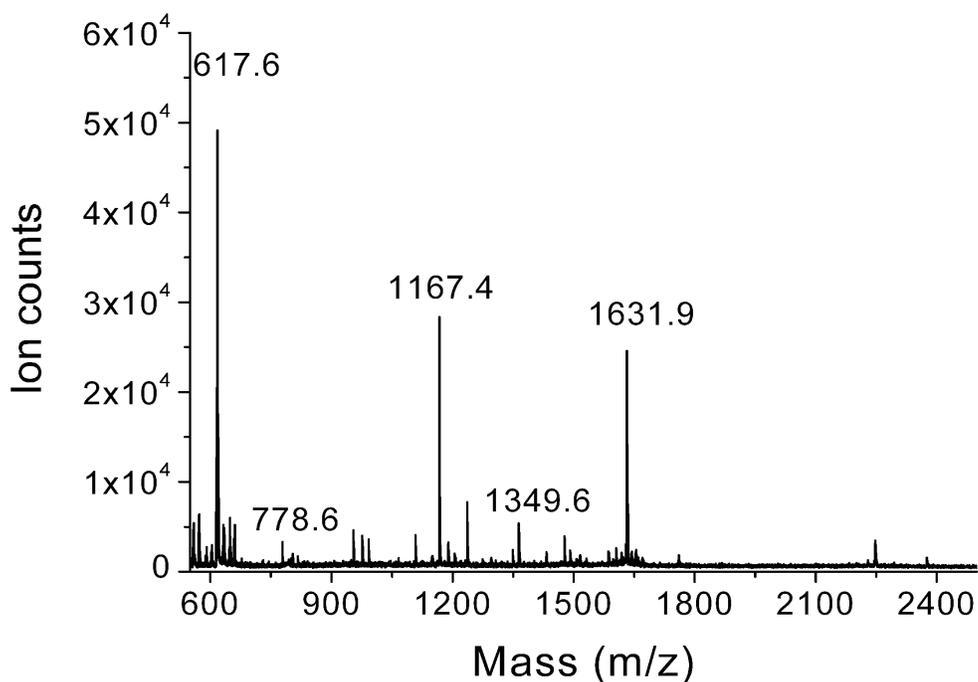
Figure 3.11 Mass spectra (positive ion mode) of immobilized-tryptic digestions at pH 7.9, 37°C. Peaks m/z 778.6, 1167.4, 1349.6, and 1631.9 were digestion peaks.

Figure 3.12 shows a plot of the ratios of peak heights at 37°C versus ambient for given ions m/z 617.7, 1167.6 and 1632.2 at three pH values. The heme fragment ion m/z 617.7 peak height ratios are less than 1 and the peak height ratios of the digest fragment ions m/z 1167.7 and 1632.2 are larger than 1, which indicates that at higher temperature more cytochrome *c* was digested. When we study m/z 617.7 peak for intact cytochrome *c*, the peak height ratio for 37°C versus ambient for the heme fragment ion did not change with pH value. When we study the fragment peaks (circle and cross symbol traces), pH 7.7 gave the largest peak height ratio difference for 37°C versus ambient conditions. When we studied the protein sequence coverage, it ranged from 53 to 60% at ambient temperature, and from 68 to 81% at 37°C. The highest protein sequence coverage was obtained at 37°C and pH 7.7. The standard deviation of peak height ratios and the protein sequence coverage range indicated that the digest fragment ion products were most variable at the highest pH. Shifts in pH (measured at ambient) during the incubation at 37°C, suggest that the volatility of NH_3 led to this greater variability.
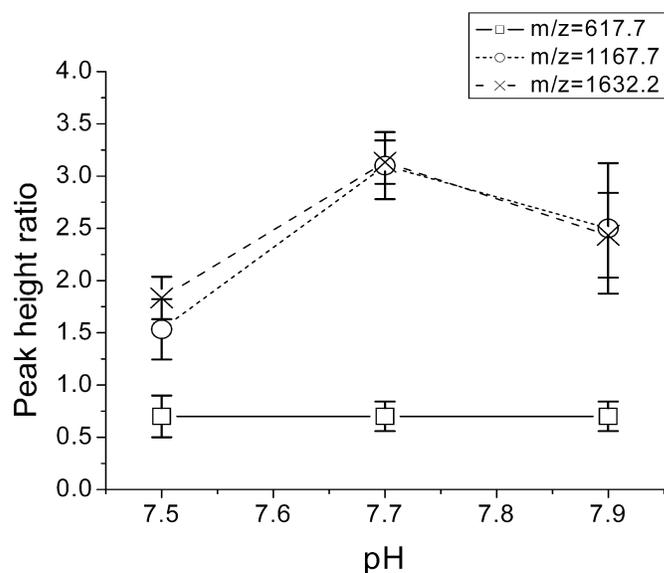
Figure 3.12 The ratios of peak heights at 37°C versus ambient for given ions m/z 617.7, 1167.6 and 1632.2 at three pH values.

3.3.4 Desalting before SMALDI

The presence of non-volatile salts in a sample causes ionization suppression and loss of sample signal, which is a significant problem for samples from blood, urine and other biological fluids. Additionally, the phosphate buffer solution used for digestion can cause suppression of signal. Simple rinsing of the film surfaces after drying may remove some of these salts, even at risk of removing some of the target sample as well. Figure 3.13. shows the spectra taken before and after washing the surfaces, following digestion by the immobilized-tryptic digestion GLAD films. Figure 3.13.a. shows only a single peak at m/z 1632.3, readily attributed to cytochrome *c*, while Figure 3.13.b. shows a series of peaks assignable to digested components of cytochrome *c*, with a 71% protein sequence coverage, and 23 matched peptides. Washing is clearly an effective step in reducing interference effects and producing good quality peptide signal.
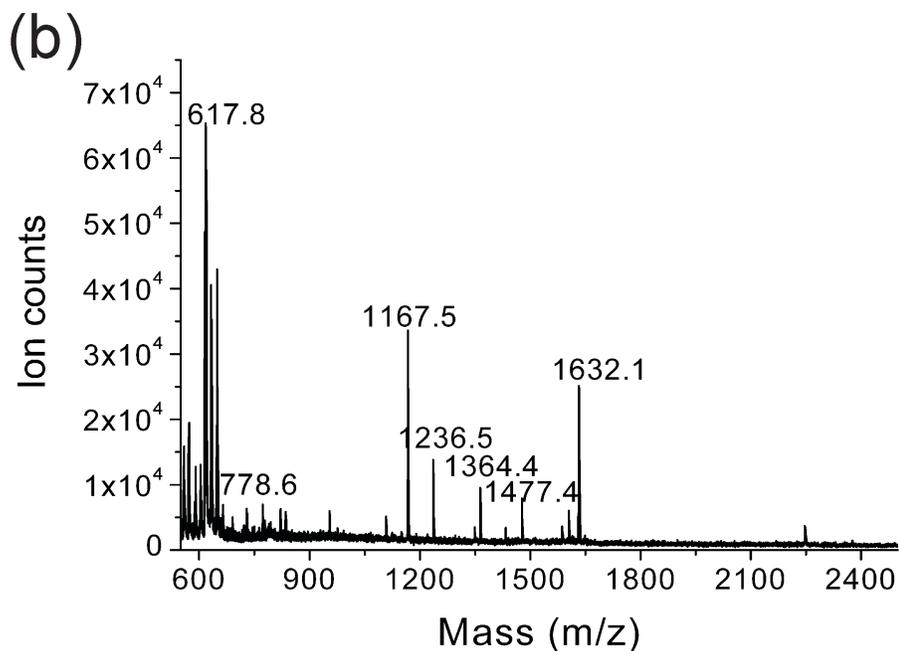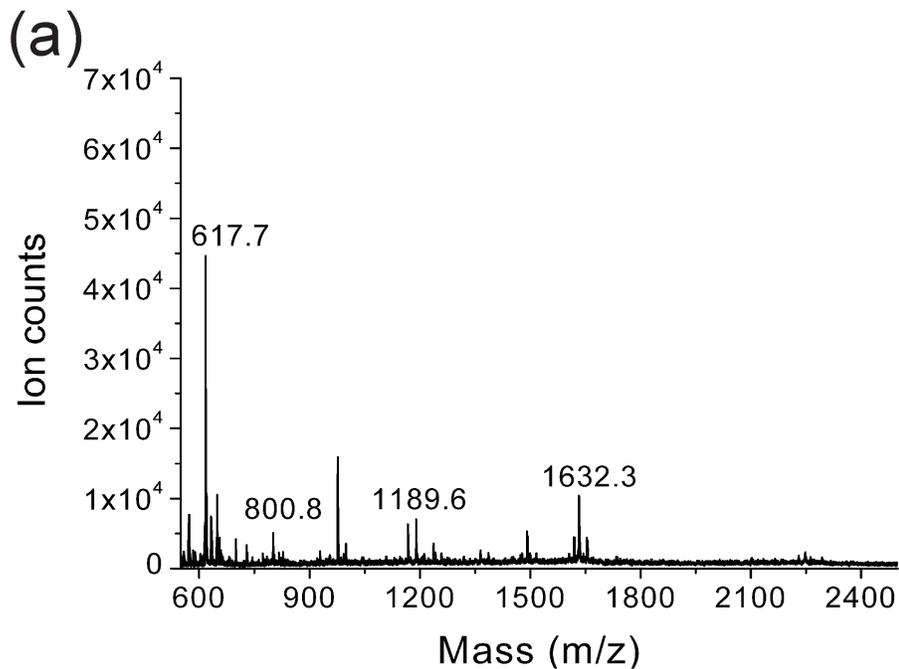
Figure 3.13 (a): Mass spectrum of the digestion on immobilized-tryptic digestion GLAD films directly to SMALDI, peak m/z 1632.3 was digestion peak; (b): mass spectrum of the desalting before SMALDI of the same chip, peak m/z 778.6, 1167.5, 1236.5, 1364.4, 1477.4, and 1632.1 were digestion peaks. Mass spectra obtained under positive ion mode.

3.3.5 MALDI and SMALDI Comparison

A comparison of MALDI and SMALDI detection of free solution tryptic digestion was performed. Two different cytochrome *c* solution concentrations were evaluated in terms of the protein sequence coverage and matched peptides. A solution of trypsin (5 μL of 0.1 mg/mL) and cytochrome *c* (5 μL of 1 and 0.5 mg/mL, respectively) were mixed and reacted at 37°C for 2 hr. The mixture was detected by MALDI with matrix HCCA and SMALDI on bare Si GLAD film. Table 3.2 shows the summary of the protein sequence coverage and matched peptides using different detection techniques.

In MALDI analysis, when 1 mg/mL cytochrome *c* was digested, a total of 32 to 37 peaks were assigned to peptide fragments of cytochrome *c*, the average was 34 peaks. The protein sequence coverage was from 86 to 89% with an average of 87%. When 0.5 mg/mL cytochrome *c* was digested, a total of 39 to 42 peaks were assigned to peptide fragments of cytochrome *c*, the average was 40 peaks. The protein sequence coverage was from 83 to 86% with an average of 85%. A lower cytochrome *c* concentration showed more matched peptides with slightly lower protein sequence coverage.

The same free solution digestion samples were detected by SMALDI-MS. For 1 mg/mL cytochrome *c* samples, a total of 20 to 30 peaks were assigned to peptide fragments of cytochrome *c*, the average was 26 peaks. The protein sequence coverage was from 58 to 82% with an average of 70%. For 0.5 mg/mL cytochrome *c* samples, a total of 31 to 32 peaks were assigned to peptide fragments of cytochrome *c*, the average was 32 peaks. The protein sequence coverage was from 61 to 68% with an average of 63%. When the same digestion sample was detected by SMALDI-MS, fewer matched peptides with more

variable protein sequence coverage were obtained compared with MALDI-MS. The average protein sequence coverage by MALDI detection, divided by the average protein sequence coverage by SMALDI detection, was 1.3 at both concentrations. The average number of matched peaks by MALDI detection, divided by the average number of matched peaks by SMALDI detection, was 1.3 at both concentrations. This result indicates that MALDI sets a baseline performance that is better than SMALDI by a factor of 1.3.

Table 3.2 MALDI and SMALDI comparisons of protein sequence coverage and matched peptides (n=3).

Detection method	MALDI		SMALDI	
Cyto *c* conc. (mg/mL)	1	0.5	1	0.5
Protein sequence coverage (%)	86-89	83-86	58-82	61-68
Matched peptides	32-37	39-42	20-30	31-32

3.3.6 Immobilized-tryptic Digestion GLAD Films Evaluation

The performance of the digestion on GPTMS immobilized-tryptic digestion GLAD film surfaces was evaluated by comparing with free solution digestion detected on bare Si GLAD films. Two different concentrations of cytochrome *c* (5 μL of 1 and 0.5 mg/mL, respectively) at reaction times of 2 hr and of 30 min were studied. The representative mass spectrum in Figure 3.14.a, of the free solution digestion, and Figure 3.14.b of the tryptic digestion on modified GLAD films are shown for 30 min of 1 mg/mL cytochrome *c*. The net result for tryptic digestion on modified GLAD films was similar to free solution digestion, in terms of the protein sequence coverage and matched peptides. A reduction in the number of autodigestion peaks was observed on the immobilized tryptic digestion films. Trypsin autodigestion is known to produce up to 13 mass fragment peaks. When cytochrome *c* (5 μL of 1 mg/mL) was digested in solution for 2 hr, 10 of the 13 trypsin autodigestion peaks were observed by SMALDI. When cytochrome *c* (5 μL of 1 mg/mL) was digested on immobilized tryptic digestion film, only 4 of 13 autodigestion peaks were seen for both 30 min and 2 hr digestion.
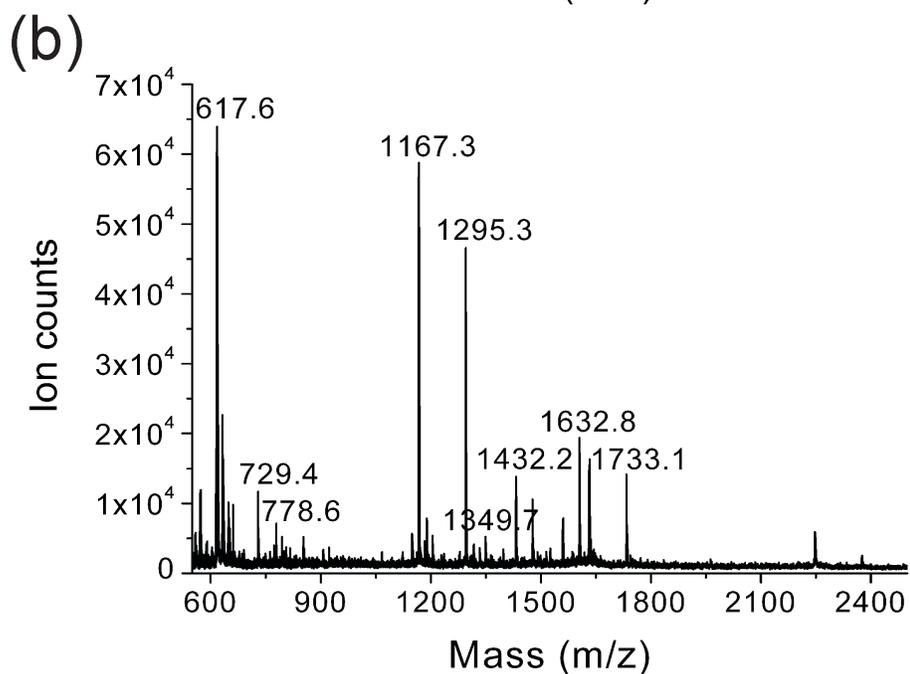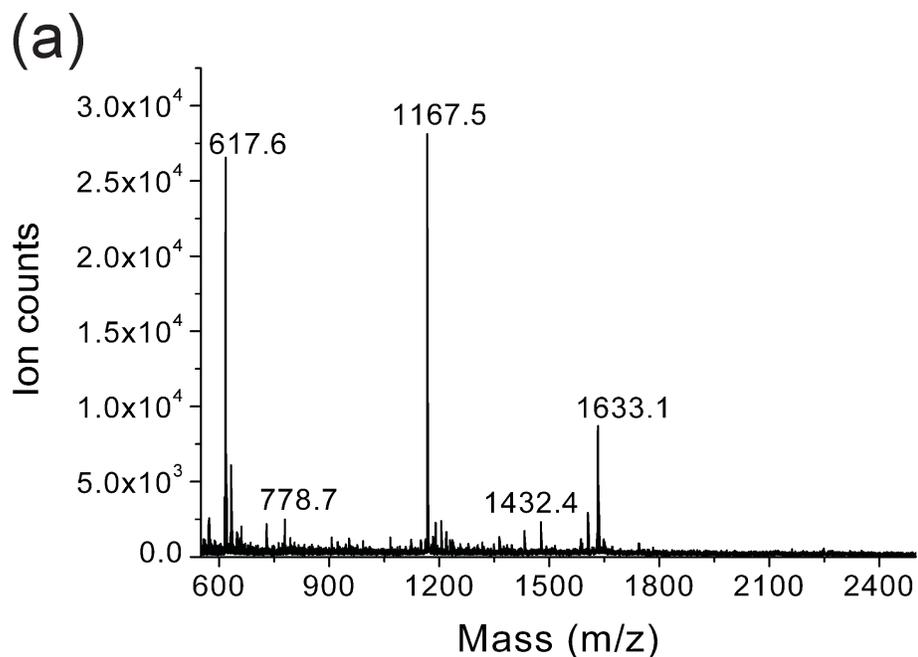
Figure 3.14 (a): Free solution digestion for 30 min of 1 mg/mL cytochrome *c*; (b): digestion on GPTMS immobilized-tryptic digestion GLAD films for 30 min of 1 mg/mL cytochrome *c*. Mass spectra obtained under positive ion mode.

Table 3.3 shows the summary of the protein sequence coverage and matched peptides of free solution digestion and immobilized-tryptic digestion at different cytochrome *c* concentrations and reaction times. When comparing cytochrome *c* concentration and different reaction times, there was no obvious trend of matched peaks and protein sequence coverage changes from free solution digestion to immobilized-tryptic digestion.

Table 3.3 Free solution digestion and immobilized-trypsin digestion comparisons of protein sequence coverage and matched peptides (n=7).

	Free solution digestion				Immobilized-trypsin digestion			
Reaction time	2hrs		30min		2hrs		30min	
Cyto *c* conc. (mg/mL)	1	0.5	1	0.5	1	0.5	1	0.5
Protein coverage (%)	58-82	61-68	58-62	54-62	64-70	65-67	65-70	59-65
Matched peptides	20-30	31-32	20-22	16-20	24-32	18-23	19-28	19-21

In free solution digestion with SMALDI analysis, when 1 mg/mL cytochrome *c* was digested for 2 hr, a total of 20 to 30 peaks were assigned to peptide fragments of cytochrome *c*. The protein sequence coverage was from 58 to 82%. When 0.5 mg/mL cytochrome *c* was digested for 2 hr, a total of 31 to 32 peaks were assigned to peptide fragments of cytochrome *c*. The protein sequence coverage was from 61 to 68%. When 1 mg/mL cytochrome *c* was digested for 30 min, a total of 20 to 22 peaks were assigned to peptide fragments of cytochrome c. The protein sequence coverage was from 58 to 62%. When 0.5 mg/mL cytochrome *c* was digested for 30 min, a total of 16 to 20 peaks were assigned to peptide fragments of cytochrome *c*. The protein sequence coverage was from 54 to 62%. The results indicate that longer reaction time gives more matched peptides, while the protein sequence coverage was relatively constant.

For immobilized-tryptic digestion with SMALDI analysis, when 1 mg/mL cytochrome *c* was digested for 2 hr, a total of 24 to 32 peaks were assigned to peptide fragments of cytochrome *c*. The protein sequence coverage was from 64 to 70%. When 0.5 mg/mL cytochrome *c* was digested for 2 hr, a total of 18 to 23 peaks were assigned to peptide fragments of cytochrome *c*. The protein sequence coverage was from 65 to 67% with an average of 66%. When 1 mg/mL cytochrome *c* was digested for 30 min, a total of 19 to 28 peaks were assigned to peptide fragments of cytochrome *c*. The protein sequence coverage was from 65 to 70%. When 0.5 mg/mL cytochrome *c* was digested for 30 min, a total of 19 to 21 peaks were assigned to peptide fragments of cytochrome *c*. The protein sequence coverage was from 59 to 65%. The results indicate that the reaction time does not greatly affect the number of assigned matched peptides. The variability of protein sequence coverage was smaller (within 6%). Therefore, although there was no advantage in the efficiency of immobilized-tryptic digestion compared with free solution digestion, the immobilized-tryptic digestion by SMALDI analysis is more reproducible, and involves fewer sample processing steps.

3.4 Conclusion

Si GLAD films, which have a large surface area, provide a good matrix for immobilization. The modification process was simple when using GPTMS functionalization on Si, giving a film ready for trypsin linkage. Digestions on the GPTMS immobilize-tryptic digestion GLAD films were performed with the sample protein, cytochrome c. The enzyme can be directly digested and then detected by SMALDI-MS after a simple washing step. In this work, the samples were used at relatively high amounts (~40 pmol protein), and the peptides are reasonably high in mass (> 500 m/z). Under these conditions, a simple washing step readily reduced salt interference, while leaving detectable amounts of peptide on the surface for analysis. However, in Chapter 4, we dealt with amino acids in artificial cerebrospinal fluid (CSF) samples, which are in a lower mass range, and salts are a more major interference when trying to achieve the required sensitivity. The advantage of the modified film digestion includes ready-to-use films at potentially low cost. The digestion results on GPTMS immobilized-tryptic digestion GLAD films were similar to the free solution digestion detected by SMALDI, though they had 30% lower performance than MALDI. The results show the feasibility of applying Si GLAD films for the rapid peptide mass fingerprinting by SMALDI-MS.

Chapter 4 Functionalization of Si GLAD Films for Detection of Free Amino Acids

4.1 Introduction

Since free amino acids (FAA) are important in neurotransmission, receptor function and are implicated in neurotoxicity, changes in FAA concentration can be an early indicator of neurodegeneration in Alzheimer's disease (AD), which is a neurodegenerative disorder. Fonteh *et al* determined concentration changes in FAA of cerebrospinal (CSF), plasma, and urine samples in probable Alzheimer's disease (pAD) subjects compared with control (CT) subjects using liquid chromatography and electrospray ionization tandem mass spectrometry (LC-MS^n).[104] LC-MS^n is a powerful tool to identify target metabolites in a complex mixture, which is suitable for on-line sample analysis. In this study, we focus on a more rapid, direct-infusion MS technique, which, without any chromatographic separation, can achieve detection FAA concentration changes for metabolite quantitation in batches. MALDI-MS, which is a powerful methodology in analytical chemistry with relatively low cost instrumentation, is limited in metabolite quantitative studies for two reasons. The first reason is that in typical MALDI experiments, strong matrix and matrix fragment ion signals will interfere with the detection of metabolite molecules in the low mass range (MW<700). Furthermore, quantitative analyses are challenging because of the shot-to-shot variability which result from the heterogeneity of the matrix and analyte co-crystallization.[105]

Recently our group demonstrated silicon (Si) glancing angle deposition (GLAD) films with highly controlled morphology for use in solid matrix laser desorption/ionization (SMALDI).[22] Si GLAD film based SMALDI takes advantage of the properties of Si nanostructures surfaces, such as the absorption of UV light, low thermo conductivity and the ability to trap liquids, to assist in the ion desorption/ionization process. Most importantly, this matrix-free technique will not produce matrix fragment ions, which interfere with the detection of small molecules. In this chapter, we develop silylated Si GLAD films for SMALDI detection of FAA. Our results showed the aptitude of silylated functionalization Si GLAD surfaces for detection of FAA. In particular, semi-quantitative analysis of pure glutamine and histidine samples, and of the spiked glutamine and histidine in artificial CSF samples were demonstrated.

The work presented in this chapter was in collaboration with Dr. Michael Brett's group in the Department of Electrical and Computer Engineering at the University of Alberta. Jason Sorge assisted with the growth of the GLAD films.

4.2 Experimental Section

4.2.1 Chemicals and Materials

Methanol, toluene, trifluoroacetic acid (TFA), HCl, NaCl, KCl, $CaCl_2•2H_2O$, $MgCl_2•6H_2O$, $Na_2HPO_4•7H_2O$, $NaH_2PO_4•H_2O$, [Des-Arg[9]]-bradykinin (MW=904), angiotensin II (MW=1046), trichloro (1*H*, 1*H*, 2*H*, 2*H*-perfluorooctyl) silane, octyltrimethoxysilane, asparagine, glutamine, histidine were purchased from Sigma-Aldrich. Silicon wafers (Test Grade, 10cm diameter, University Wafer, Boston, MA,

USA) and evaporated material, silicon (CERAC, Inc., Milwaukee, WI, USA) were used in GLAD fabrication process. Solutions were prepared using ultrapure water prepared with a deionizing system (Millipore Canada, Mississauga, ON, Canada). [Des-Arg^9]-bradykinin and angiotensin II stock solutions (1 mM) were prepared by constituting lyophilized samples in water. Glutamine, histidine and asparagine solutions (250 mM) were prepared by constituting lyophilized samples in methanol/water/1M HCl (25/25/50, v/v/v) and diluted to 0.25 mM by water as stock solutions.

4.2.2 Si GLAD Films Preparation

4.2.2.1 Si Wafer Cleaning

Si wafer substrates were cleaned prior to deposition by hot piranha solution (H_2SO_4: H_2O_2, v: v/1:3) for 15 min, followed by rinsing with water and drying with nitrogen. Piranha is highly reactive and can become extremely hot when prepared, so care must be taken. We prepared this solution by adding hydrogen peroxide to sulfuric acid very slowly. We handled piranha solution by using wet deck in University of Alberta NanoFab (Edmonton, AB).

4.2.2.2 Electron Beam Deposition

Cleaned Si wafers were cut into half by diamond stylus and mounted onto a deposition chuck. The deposition chuck was loaded into a high vacuum electron-beam deposition system (AXXIS, Kurt J. Lesker Co., Clairton, PA, USA). Silicon vertical posts of 500 nm

were deposited using GLAD at an angle of 86° relative to the substrate normal, using a substrate rotation rate of 1.2 RPM at a deposition rate of 0.4 to 0.9 nm/s.

4.2.3 Silylated Functionalization of Si GLAD Films

Si GLAD films were cut into the desired size by diamond stylus and immersed in silane solution, which was prepared by adding 50 μL trichloro (1H, 1H, 2H, 2H-perfluorooctyl) silane into 5 mL methanol, for 30 min. The functionalized Si GLAD films were stored in petri dishes.

4.2.4 Critical Point Drying

The functionalized Si GLAD films were transferred into the pressure chamber of a critical point drier (Tousimis Research Corporation, Rockville, MD, USA). In purging cycles, the liquid CO_2 was filled into the pressure chamber and immersed the films. Then the liquid CO_2 influxed and mixed, the fluid was released out of the pressure chamber and new liquid CO_2 was introduced. After several purging cycles, the heating process that generated supercritical CO_2 started, from which the supercritical CO_2 formed gaseous CO_2 while maintaining the temperature constant at 31°C (critical temperature of CO_2) and then opening the gas outlet valve to reduce the pressure in the chamber. After critical point drying, the functionalized Si GLAD films were ready for use.

4.2.5 Scanning Electron Microscopy

Scanning electron microscopy (SEM) images were taken of the chromium coated samples using a JEOL 6301F field emission scanning electron microscope. Working distances and accelerating voltages used to obtain images are listed at the bottom of each image. The chromium coated specimens are coated with an Edwards Xenosput XE 200 coater.

4.2.6 Mass Spectrometry

Mass spectrometry measurements were performed on an Applied Biosystems (Framingham, MA, USA) Voyager STR time-of-flight mass spectrometer. A pulsed N_2 laser at a wavelength of 337 nm was operated at a repetition rate of 3.0 Hz. Positive ion mode mass spectra were acquired under the following conditions. The reflector, delayed extraction mode was used. An accelerating potential of 20 kV, a 74% grid potential, a 0.07% guide wire voltage and a delay time of 350 nsec was applied. Each spectrum is the result of 100 laser shots. Negative ion mode mass spectra were acquired under the following conditions. The reflector, delayed extraction mode was used. An accelerating potential of 18 kV, a 96% grid potential, a 0.1% guide wire voltage and a delay time of 250 nsec was applied. Each spectrum is the result of 100 laser shots. The MS data recorded were processed by Voyager Data Explorer version 4.0 (Applied Biosystems, Framingham, MA, USA). The films were mounted on a modified MALDI plate by conductive adhesive tape as described in our previously published work.[22]

4.3 Results and Discussion

4.3.1 GLAD Film SMALDI Performance

4.3.1.1 Sensitivity Tests

A sensitivity test was performed to evaluate the performance of Si GLAD film-based SMALDI with current instrumental conditions. A time-of-flight mass spectrometer was used to conduct mass spectrometry measurement at positive ion mode. A series of [Des-Arg^9]-bradykinin (MW=903) solutions were diluted by methanol/0.1% TFA (30/70, v/v) in different concentrations. 0.1% TFA was added to reduce ion suppression. Laser intensities were adjusted in order to find the minimum energy needed to obtain the best signal-to-noise ratios for the analytes. Laser intensities were varied in the range of 1650-1750. Generally, lower concentrations of the analytes required higher laser intensities.

The limit of detection (S/N=10) was 0.6 fmol, which was obtained by calculating the signal-to-noise ratios for the analyte peak (m/z=903) of the serial dilutions of [Des-Arg^9]-bradykinin solution as presented in Figure 4.1. The limit of detection of positive ion mode Si GLAD based SMALDI was obtained in the sub-femtomole range, which was comparable with our previously published work.[22]
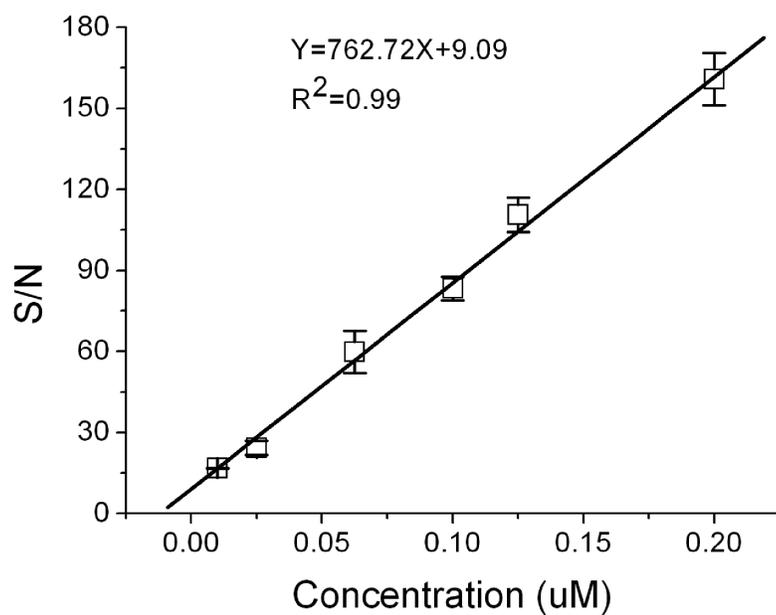
Figure 4.1 Sensitivity of Si GLAD film SMALDI. Plot representing the signal-to-noise ratio of [Des-Arg[9]]-bradykinin (MW=903) at the series of concentrations. Mass spectra obtained under positive ion mode. (n=3)

4.3.1.2 Positive vs. Negative Ion Mode

The mass spectra of pure histidine (MW=155) solutions obtained under positive and negative ion modes were compared. In positive ion mode, only at stock solution concentration (0.25 mM) can the analyte peak m/z 153 be observed. At lower concentrations, the two strong chemical background peaks at m/z 130 and m/z 186, which were also observed in our previously published work,[22] dominated the spectra and the analyte peak (m/z=153) was suppressed. We tried two methods to reduce the chemical background peaks, but neither of them solved the problem. First, we used UV-Ozone treatment, which was reported to reduce the background noise in the low mass range,[22] before deposition of the sample spots. Second, we diluted the histidine solutions with different compositions of 0.1% TFA in methanol for the purpose of reducing ion suppression. These chemical background peaks (m/z=130 and m/z=186) are most likely due to the adsorption of contaminants from the atmosphere on Si GLAD films. While the UV-Ozone treatment worked to reduce contamination above ~m/z 250, consistent with our previous report, in this very low mass range, it just re-distributes the chemical noise. In negative ion mode, the concentration of histidine we could detect was lower than 20 μM, as shown in Figure 4.2. This result was comparable to the reported values for detection of histidine on etched porous Si (50 μM).[106]
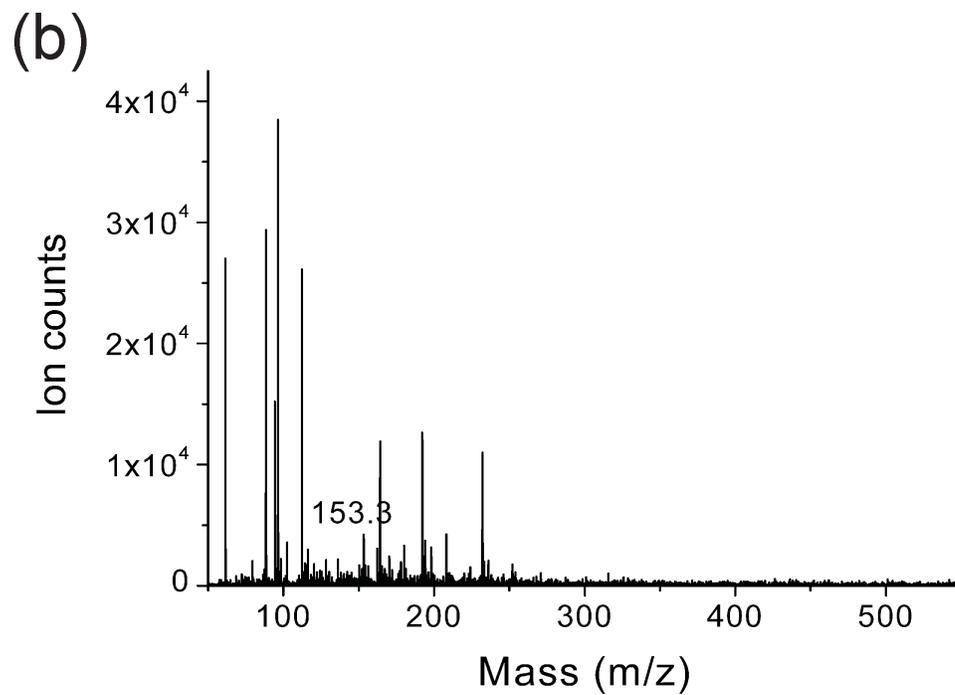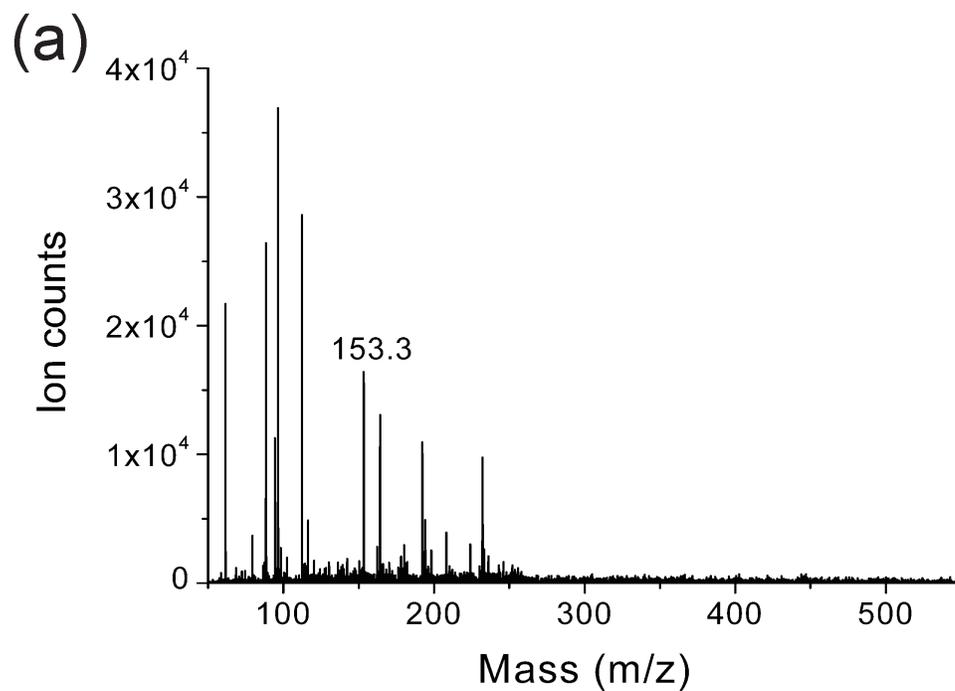
Figure 4.2 Histidine (m/z=153.3) was detected on Si GLAD films. (a) 100 μM histidine diluted by water; (b) 20 μM histidine diluted by water. Detected in negative ion mode.

4.3.2 Si GLAD Surface Modification

The concentration of histidine in CSF presented in pAD subjects was about 20 μM and the histidine in CSF from pAD subjects compared to CT subjects was reduced by 23%.[104] In our application, the bare Si GLAD film based SMALDI was sensitive enough to detect 20 μM pure histidine solution, but did not have good enough precision for detection of the changes of histidine concentration (~4 μM). Surface modification is reported as a method for improving DIOS sensitivity.[107] In this study, we explored two different Si GLAD surface modification methods for the purpose of enhancing the detection sensitivity. One is physical deposition of chemicals on the surface, and the other is silylated functionalization.

4.3.2.1 Physical Deposition of Teflon

Siuzdak's group developed nanostructure-initiator mass spectrometry (NIMS), which used porous Si to trap liquid "initiator" materials.[108] In their protocol, the commonly used initiator chemical is bis(heptadecafluoro-1,1,2,2-tetrahydrodecyl) tetramethyldisiloxane (Bis F17), which has fluorocarbon function groups, as shown in Figure 4.3.
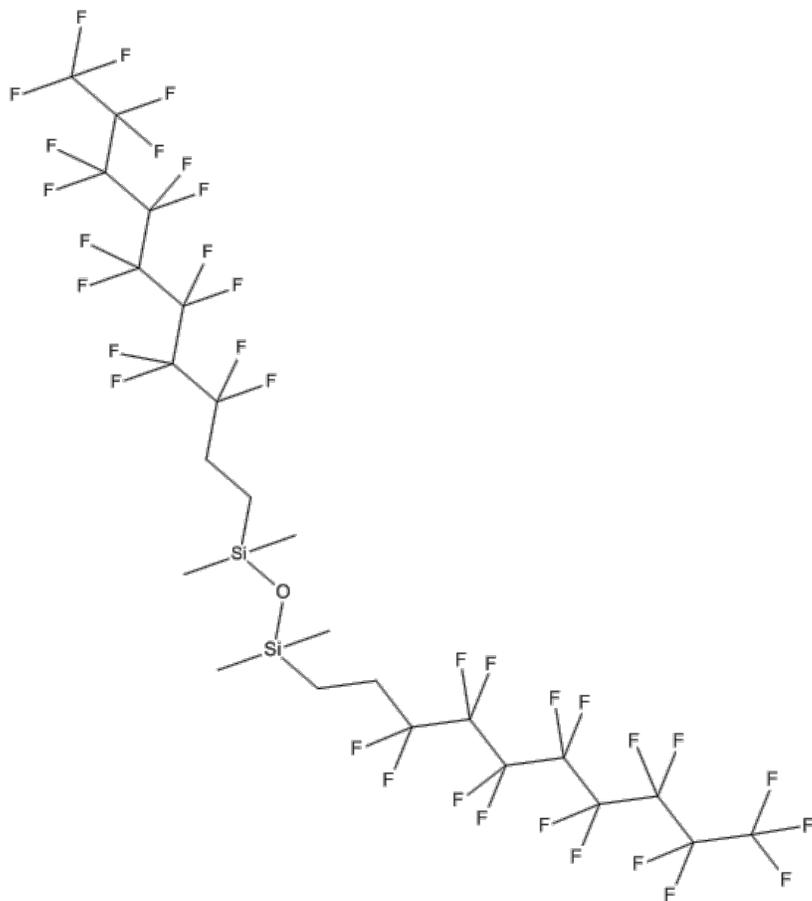
Figure 4.3 Chemical structure of Bis F17.

In our experimental design, we first considered the fluoropolymer, Teflon. We studied three different methods to carry out Teflon related physical deposition. The first method is that we followed NIMS preparation protocols.[108] We deposited several drops of 1% Teflon AF solution on 500 nm Si GLAD films and blew out excess solvent with nitrogen, followed by heating the films in an oven. The second method was to spin coat a thin Teflon layer (~50 nm) on a Si substrate and then grow 500 nm Si GLAD vertical nanoposts on the Teflon coated substrates, forming the Si GLAD on Teflon coating surfaces. The third method was to spin coat a thin Teflon layer (~50 nm) on 500 nm Si GLAD films. Angiotensin II (MW=1046) was pipetted on these films for the purpose of performance evaluation. SMALDI mass spectra were obtained using positive ion mode.

In the first method, a thick polymer coating that covered the Si GLAD films was observed. There was no analyte peak at m/z 1046 (1 μM angiotensin II) shown in the mass spectra even at high laser intensity (~2200). This may be due to the coating blocking the silicon vertical nanoposts on GLAD films. In the second method, it is interesting that the Si GLAD on Teflon coated surfaces (ion counts ~1.1×10^4) has similar SMALDI signals as the bare Si GLAD (ion counts ~1.7×10^4) for 1 μM Angiotensin II, as shown in Figure 4.4.a-b. In Figure 4.4.c-d, the Si GLAD on Teflon coating surfaces (ion counts ~4.5×10^3) even showed slightly better SMALDI signals than the bare Si GLAD (ion counts ~1.0×10^3) for 0.1 μM angiotensin II. However, the chemical background noise in the lower mass range (50-300), which was detected on the Si GLAD on Teflon coating surfaces, was noisier than the bare Si GLAD as shown in Figure 4.4.a-d. In the third method, the spin coating of Teflon on Si GLAD films was poor in uniformity and repeatability and only 1 μM angiotensin II could be detected at high laser intensities

(~2200). Overall, we rejected Teflon related physical deposition in the application for detection of FAA. This Teflon physical deposition study revealed some interesting facts in SMALDI because Teflon is an insulating material, while LDI-MS is known to require conductive plates for detection. The signals of Si GLAD on Teflon coating surfaces based SMALDI may be explained by dielectric breakdown of the thin Teflon layer under the high voltage in the mass spectrometer.

(a) 500nm Si GLAD on wafer

1μM Angiotensin II
1045.5

(b) 500nm Si GLAD on 50nm Teflon coated wafer

1μM Angiotensin II
1045.5
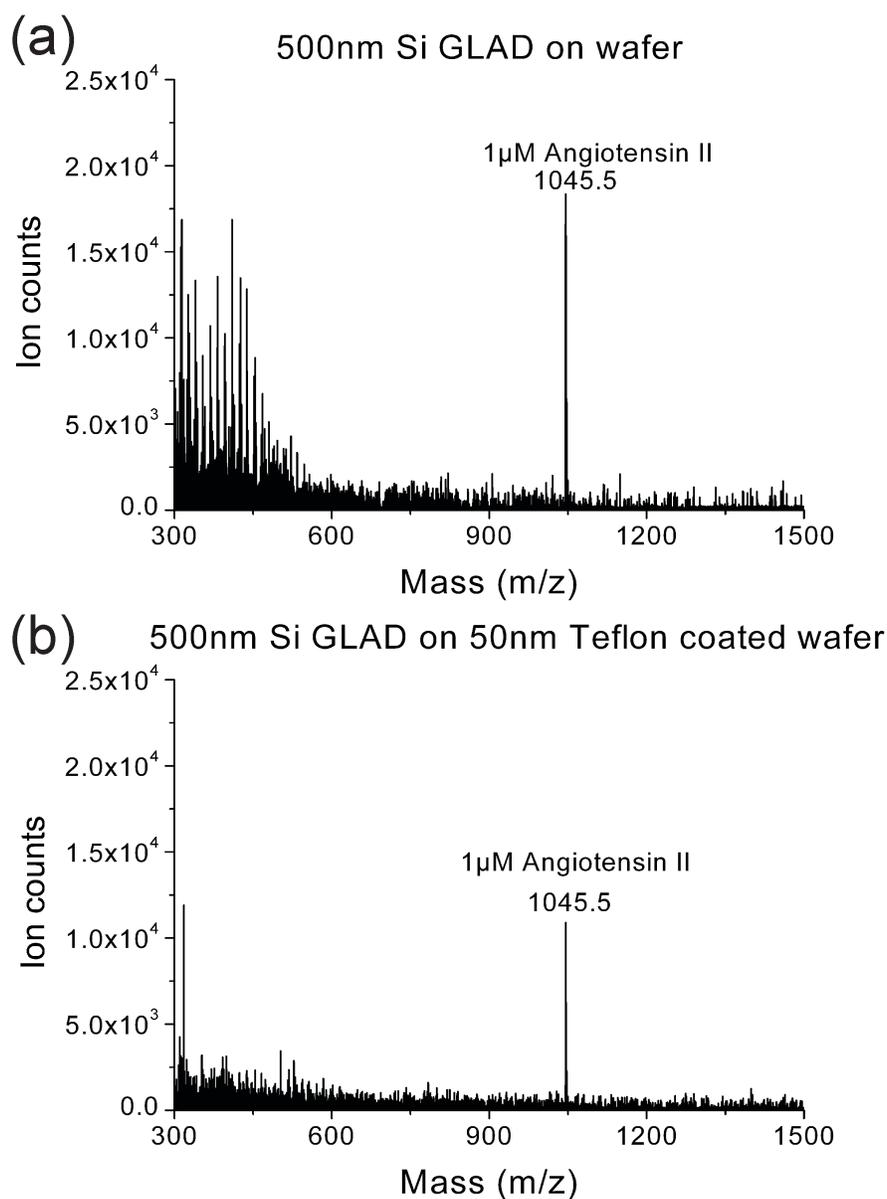
Continued on next page
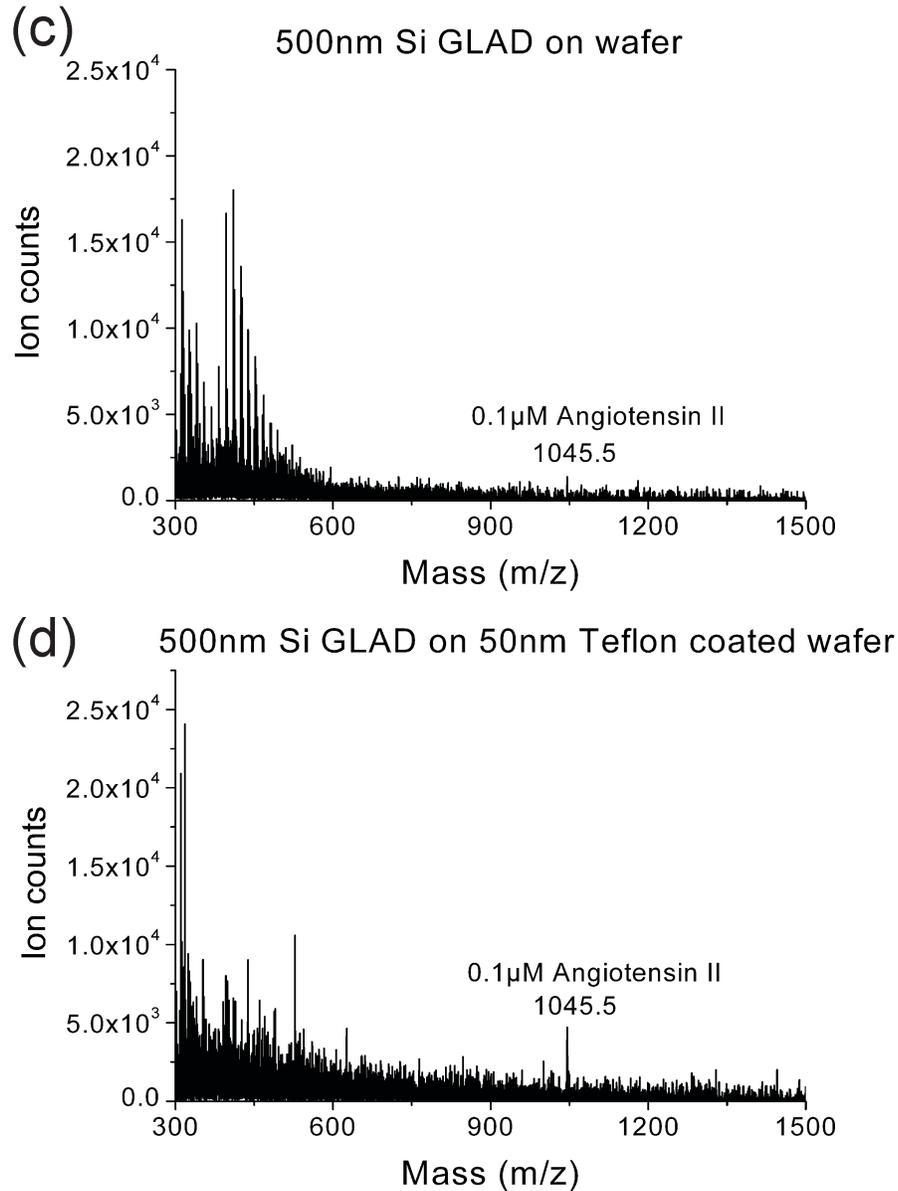
Figure 4.4 Angiotensin II (m/z=1045.5) on bare Si GLAD and Si GLAD on Teflon coating surfaces; (a) 1 μM angiotensin II, bare Si GLAD; (b) 1 μM angiotensin II, Si GLAD on Teflon coating surfaces; (c) 0.1 μM angiotensin II, bare Si GLAD and (d) 0.1 μM angiotensin II, Si GLAD on Teflon coating surfaces. Detected in positive ion mode.

4.3.2.2 Surface Silylated Functionalization

Siuzdak's group also showed the possibility of using silylated porous silicon surface for improved sensitivity.[107] We speculate on two reasons that surface coating could improve performance. The first, as evidenced by Siuzdak's work, is that the chemical background noise is greatly reduced. The oxidized Si surface is quite chemically reactive, adsorbing materials from the atmosphere easily. Coatings will reduce surface activity by capping functional groups, and so reduce adsorbate interference. More specific for GLAD films, coating will reduce hydrogen bonding between oxides on each pillar, and reduce the "nano-carpet effect". That effect leads to lower performance, so the coating may give better signals. Here, we investigated silylated functionalization on Si GLAD film surfaces. The silanization of surfaces with mono-, di-, or trialkoxysilanes occurs via the hydrolysis of the alkoxy groups, yielding hydroxyl groups that covalently bond with the silanol surface, as shown in Scheme 4.1.[109]
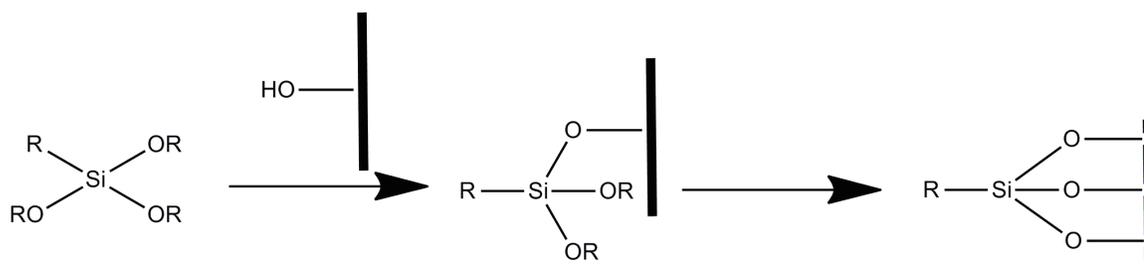
Scheme 4.1 Silanization mechanism.

4.3.2.2.1 Silylated Functionalization Processes Factors

We investigated four factors affecting the surface silylated functionalization processes—silane types, solvents, silane concentrations and silylated reaction time. The quality of silylated Si GLAD films was evaluated by SMALDI detection of pure histidine solution (0.8 μL, 200 μM) in negative ion mode.

4.3.2.2.1.1 Silane Types and Solvents

We chose two different silanes, octyltrimethoxysilane and trichloro (1*H*, 1*H*, 2*H*, 2*H*-perfluorooctyl) silane, as shown in Figure 4.5. The two silanes are chosen because 1) they are transparent to UV light and unable to ionize and 2) they have inert and hydrophobic side chains. The silylated functionalization was accomplished by liquid phase deposition of silane in organic solvent. It was reported that a uniform deposition of a silane monolayer upon glass requires a small amount of water along with hydroxyl groups on the substrate surfaces.[110] In our study, the organic solvents were used without drying, though they were the highest commercial grades. At first, we used toluene as the solvent for octyltrimethoxysilane and trichloro (1*H*, 1*H*, 2*H*, 2*H*-perfluorooctyl) silane functionalization reactions. However, the trichloro (1*H*, 1*H*, 2*H*, 2*H*-perfluorooctyl) silane formed miscible oil-in-oil droplets in toluene as the polar $-SiCl_3$ head groups form micelles in toluene. Alternatively, we used methanol for the trichloro (1*H*, 1*H*, 2*H*, 2*H*-perfluorooctyl) silane silanization process. Slight cloudiness was observed in the solution at the beginning and the solution became clear after vortexing. This phenomenon indicates the methanolysis of the chloro moieties of the silane, forming $3MeOH+R\text{-}SiCl_3 \rightarrow 3HCl+R\text{-}Si(OMe)_3$.

Octyltrimethoxysilane
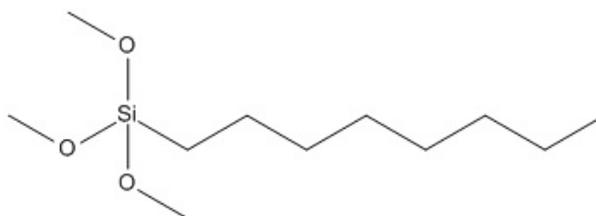
Trichloro (1*H*, 1*H*, 2*H*, 2*H*-perfluorooctyl) silane
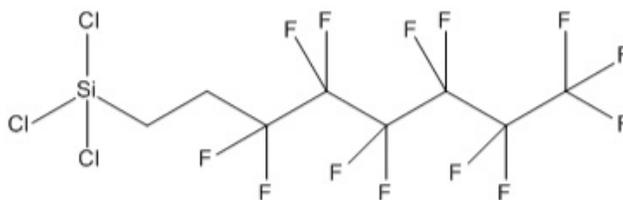
Figure 4.5 Chemical structures of octyltrimethoxysilane and trichloro (1*H*, 1*H*, 2*H*, 2*H*-perfluorooctyl) silane.

4.3.2.2.1.2 Silylated Reaction Time and Silane Concentration

For each of the silanes, we investigated two silanization factors, the silane concentrations at 1, 5, and 10% and the silylation reaction time at 30, 60, 90, and 120 min. The different silylated surfaces were freshly prepared and then evaluated by SMALDI detection of pure histidine solution (0.8 μL, 200 μM) in negative ion mode. The results are summarized in Table 4.1. When the silane concentration was at 1% and the reaction time was less than 60 min, the silylated Si GLAD film surfaces was still sensitive for the SMALDI detection of pure histidine solution (0.8 μL, 200 μM). When the reaction time was longer, at 90 and 120 min, although the appearance of the modified surfaces was the same as the shorter reaction time, these functionalized films did not give the histidine analyte peak (m/z=153) even at high laser intensities (~2500). This can be explained by the possibility of multiple surface attachments of silanol residues at longer reaction time, and cross-linking at the - $Si(OMe)_3$ moieties leading to the formation of heterogeneous polymeric layers rather than homogeneous monolayers. When the silane concentration was higher than 5%, even at the 30 min short reaction time, thin white coatings on the Si GLAD film surfaces were observed. This highly heterogeneous polymeric layer might be due to free silanol polymerization in solution prior to the silanol groups condensing with the Si GLAD film surface silanol residues.

Table 4.1 Silanization time and silane concentration study. "Y" indicates the mass spectra showed a histidine peak (m/z=153), while "N" indicates no analyte peak was seen in the mass spectra.

Conc. Time	30 min	60 min	90 min	120 min
1% (v/v)	Y	Y	N	N
5% (v/v)	N	N	N	N
10% (v/v)	N	N	N	N

4.3.2.2.2 Durability of Functionalized Surface over Time

Since the two different silane functionalized surfaces gave similar mass spectra when prepared fresh, we did some durability tests. When the silylated surfaces were stored longer than overnight, the surfaces became more hydrophobic than freshly prepared ones. Therefore, the 200 μM pure histidine solutions were diluted with methanol (v/v, 1:1) to 100 μM before SMALDI detection, to control the surface tension and the size of the droplet. This step gave a desirable sample spot size. In our preliminary tests, only trichloro (1*H*, 1*H*, 2*H*, 2*H*-perfluorooctyl) silane functionalized surfaces presented good durability as shown in Figure 4.6. The same batch of the surfaces showed similar mass spectra, in terms of the chemical background noise and the analyte peak (m/z=153) ion intensities, on day 1 and day 7. However, on overnight storage of octyltrimethoxysilane functionalized surfaces, high chemical background peaks were observed and the analyte peak (m/z=153) was suppressed. It should be pointed out that the octyltrimethoxysilane we used was many years old and trichloro (1*H*, 1*H*, 2*H*, 2*H*-perfluorooctyl) silane was newly purchased. Based on this durability study, we choose to use the trichloro (1*H*, 1*H*, 2*H*, 2*H*-perfluorooctyl) silane for all the following surface silanization. In a later phase of this project, when we wanted to explore more silanes in the modifications, a new bottle of octyltrimethoxysilane was purchased. The mass spectra did show a good durability for the newly purchased octyltrimethoxysilane functionalized surfaces from day 1 to day 7.
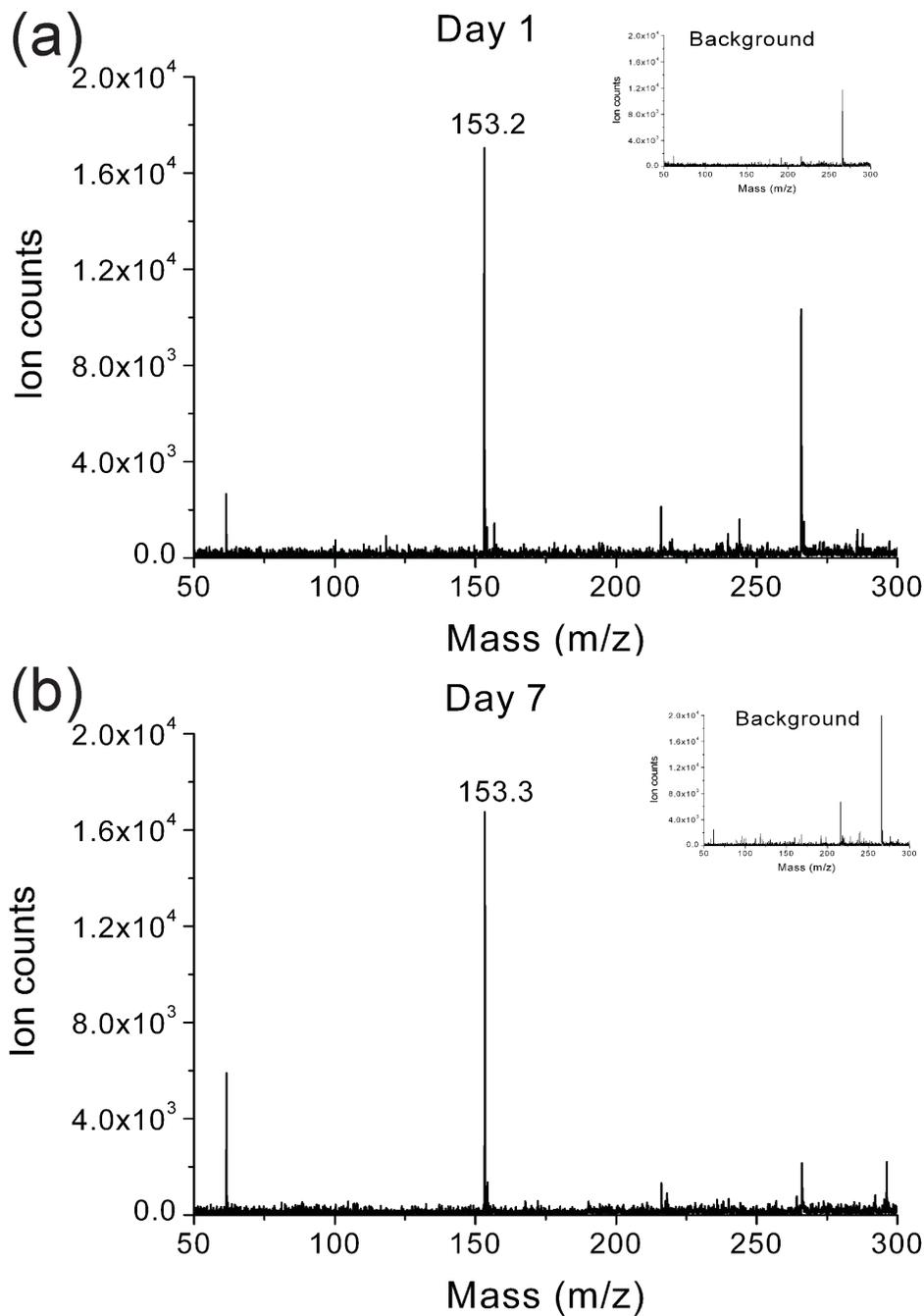
Figure 4.6 Mass spectra of durability tests of trichloro (1*H*, 1*H*, 2*H*, 2*H*-perfluorooctyl) silane functionalized surfaces; Analyte peak of histidine (m/z=153.3) on (a) Day 1 and (b) Day 7. The insert is the general background mass spectra.

4.3.2.2.3 Effective Silylated Functionalization

We chose 1% (v/v) trichloro (1*H*, 1*H*, 2*H*, 2*H*-perfluorooctyl) silane in methanol at a silanization time of 30 min as the silylated functionalization condition. The mechanism of the interaction of trichloro (1*H*, 1*H*, 2*H*, 2*H*-perfluorooctyl) silane with silanol residues on Si GLAD film surfaces is considered to be a two-step process. The first step is the methanolysis of the chloro moieties of the silane with methanol (3MeOH+R-SiCl$_3$→3HCl+R-Si(OMe)$_3$). The newly formed alkoxy silane reacted at the silanol residue surfaces to generate a silantriol, which then physisorbs onto the substrate via hydrogen bonding and ultimately forms both Si$_{substrate}$-O-Si$_{silane}$ and Si$_{silane}$-O-Si$_{silane}$ cross-linking types of covalent bonds as illustrated in Scheme 4.2. We expect the film will predominantly be a monolayer, since the chemical is freshly obtained, and is dry, so there will be little pre-polymerization, and the reaction is run under relatively dry conditions, for a fairly short time, limiting the water needed to enhance polymer formation. We used the continuous growth model to explain the functionalized monolayer formation—a liquid like disordered film is formed initially and then it further improves to a well-ordered monolayer with increasing total coverage.[111]
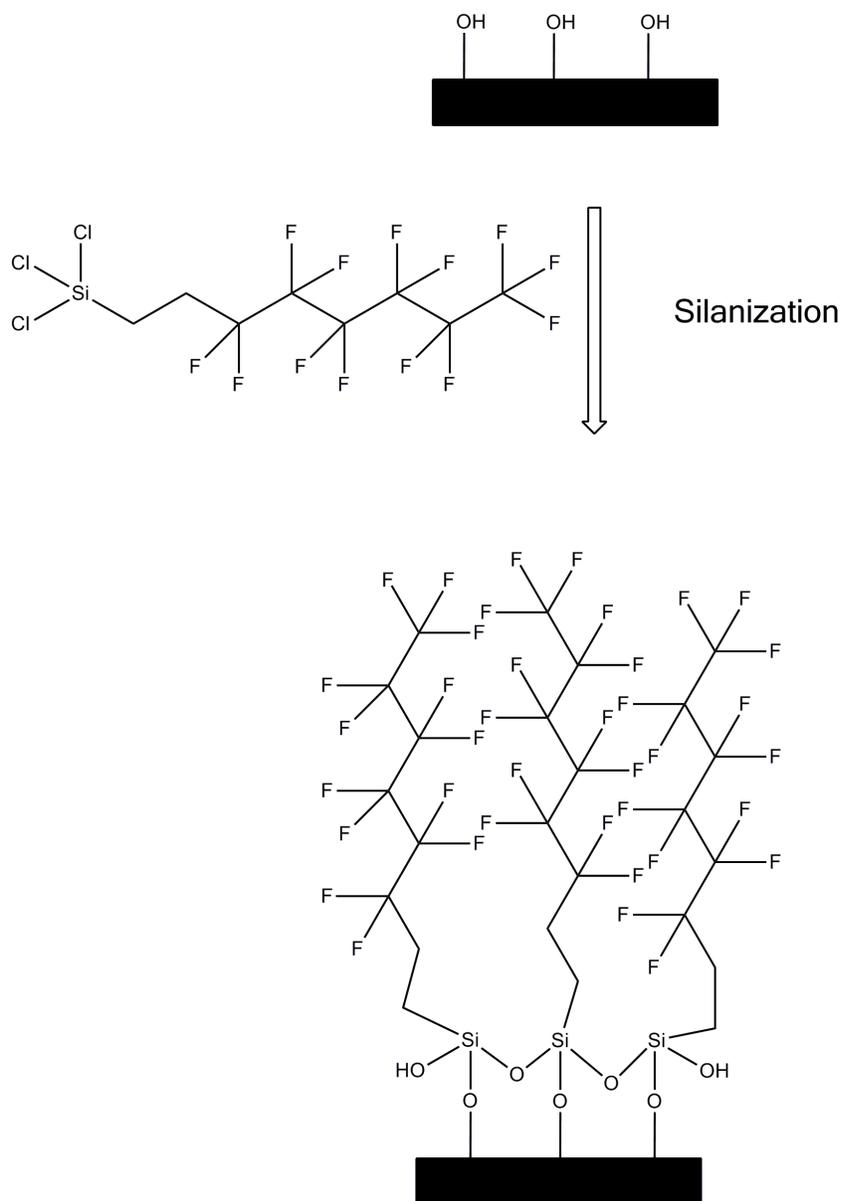
Scheme 4.2 Trichloro (1*H*, 1*H*, 2*H*, 2*H*-perfluorooctyl) silane silanization on Si GLAD film surfaces.

The mass spectra for detection of pure histidine solution (0.8 μL, 20 μM) are shown in Figure 4.7. The limit of detection (LOD) of the silylated surfaces (fmol) was better than the bare Si GLAD film surfaces (pmol). At the same time, we did not observe a "coffee-ring" effect on the silylated surfaces, which may be due to the hydrophobic modified surface. The disadvantage of a "coffee-ring" effect is that the heterogeneity of the resulting sample spots usually leads to poor sample-to-sample reproducibility of the MS signals.[112] Several studies show that the "coffee-ring" effect could be suppressed by changing surface wettability.[113, 114]
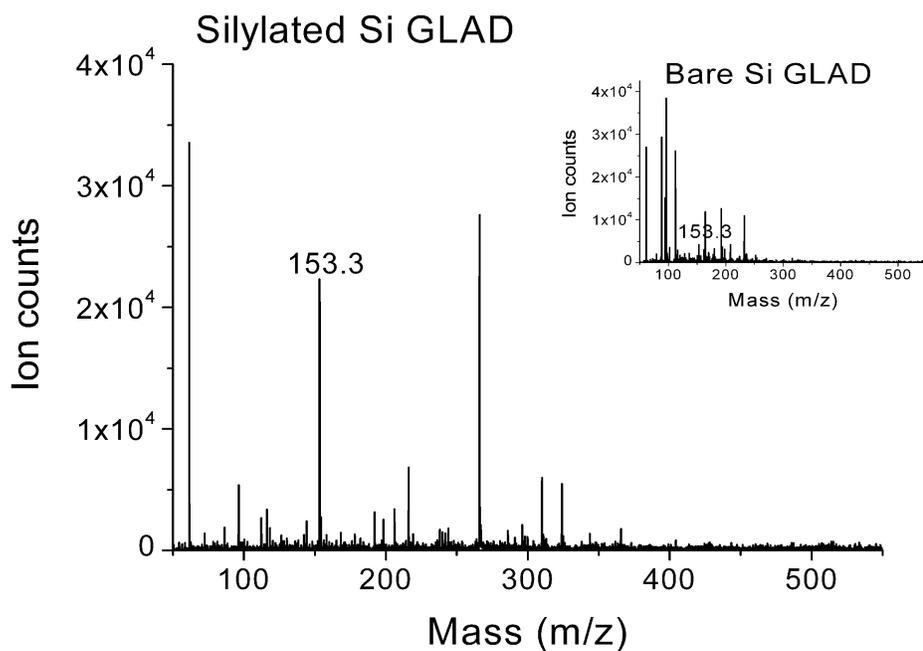
Figure 4.7 20 μM pure histidine (m/z=153.3) solution deposited on the trichloro (1*H*, 1*H*, 2*H*, 2*H*-perfluorooctyl) silane silylated Si GLAD film surfaces and the insert is 20 μM pure histidine solution deposited on the bare Si GLAD film surfaces.

4.3.2.2 SEM Images and Critical Point Drying

Figure 4.8.a-c shows the top-view, tilted-view and cross-section SEM images of the bare Si GLAD vertical nanoposts with 500 nm thickness, illustrating the columnar character of separate, individual silicon nano-pillar strands. We observed a "nano-carpet effect" in our study, which is the structural change of nanotubes and nanorods after wetting by a liquid. The nanostructures, such as nanotubes and nanorods with high surface areas and high aspect ratios are easily deformed by external forces.[101] From the point of view of SMALDI detection sensitivity, there are two qualities of the silylated surfaces. Some surfaces gave low LOD (high fmol range) while others had poor LOD in the nmol range. We carried out detailed SEM studies on these two quality surfaces. Figure 4.9.a-c shows top-view, tilted-view and cross-section SEM images of the silylated surfaces with low LOD. The SEM shows that the vertical nanoposts formed pyramid-like bundles after immersing in silane solution. These silylated surfaces gave good signals. This performance probably results from the surface retaining the vertical bundles of nanoposts structure, with pore sizes comparable to the bare Si GLAD film surfaces. Figure 4.10.a-c shows top-view, tilted-view and cross-sectional SEM images of the silylated surfaces with poor LOD. The images show that the vertical nanoposts formed a cellular network structures after immersing in silane solution, which did not retain a similar porosity to the bare Si GLAD film surfaces. There are different fabrication techniques to reducing the "nano-carpet effect". Fan *et al* recently showed that by capping the nanorods they could prevent the effect.[101] Kwan *et al* demonstrated the use of ion-milling to eliminate the effect.[115] Since the driving force to form the clusters was the capillary force when wetting the surfaces, we used critical point drying in our study to process the silylated surfaces to reduce the "nano-carpet effect".[116] Compounds at the critical point can be converted into

the liquid or gaseous phase without crossing the interfaces between liquid and gas, avoiding capillary forces. We performed critical point drying procedures on two surface preparations, samples freshly prepared and not yet dried, versus those that were coated, and allowed to cure and dry overnight. We observed that the freshly prepared surfaces became as hydrophilic as the bare Si GLAD film surfaces after critical point drying. This result indicates that the purging cycles in critical point drying wash out the un-crosslinked residues. For the overnight cured surfaces subsequent wetting and critical point drying gave surfaces that retained hydrophobic properties, and presented low LOD (fmol) in SMALDI. This result may be due to restructuring changes caused by the rewetting of the dry silylated GLAD film in liquid CO_2 and the critical point drying process, that improve the porous structure of the film.

(a)

U of A   SEI   5.0kV   X50,000   100nm   WD 7.0mm

(b)

U of A   SEI   5.0kV   X30,000   100nm   WD 13.0mm

(c)

U of A   SEI   5.0kV   X50,000   100nm   WD 9.0mm
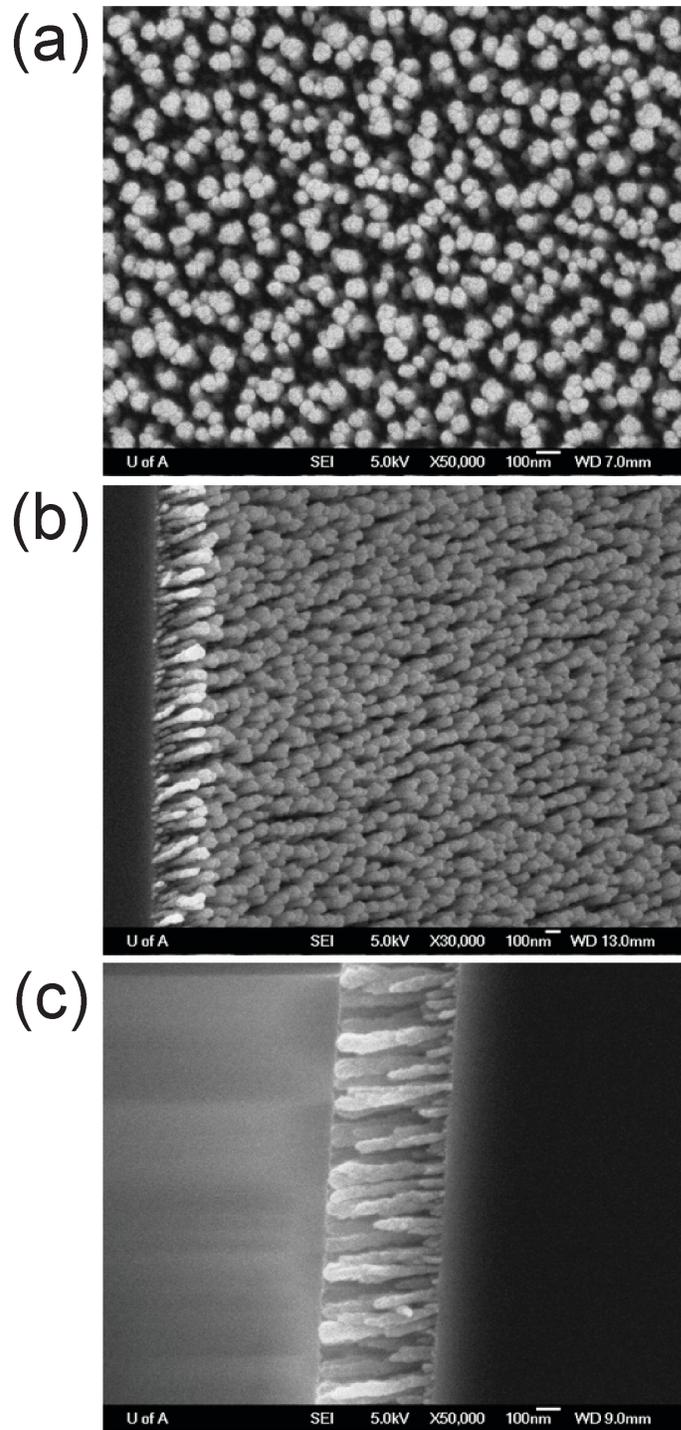
Figure 4.8 SEM images of a 500 nm thick Si GLAD film deposited on a Si substrate with (a) top view, (b) tilted view and (c) cross view. It repeats Figure 2.17.

(a)

U of A   SEI   5.0kV   X20,000   1μm   WD 10.0mm

(b)

U of A   SEI   5.0kV   X60,000   100nm   WD 12.0mm

(c)

U of A   SEI   5.0kV   X60,000   100nm   WD 11.0mm
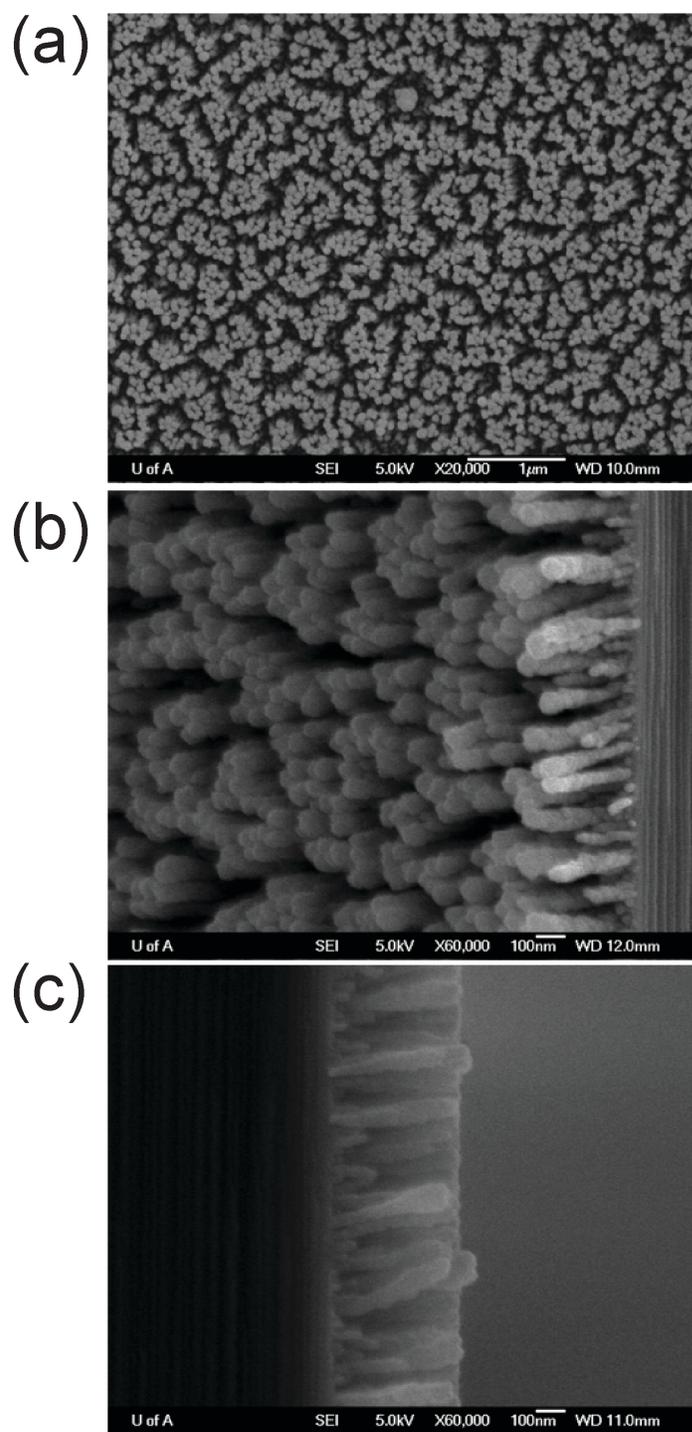
Figure 4.9 SEM images of a 500 nm thick Si GLAD films functionalized with trichloro (1*H*, 1*H*, 2*H*, 2*H*-perfluorooctyl) silane in a good quality with (a) top view, (b) tilted view and (c) cross view.

(a)

U of A   SEI   5.0kV   X20,000   1μm   WD 8.0mm

(b)

U of A   SEI   5.0kV   X20,000   1μm   WD 13.0mm

(c)

U of A   SEI   5.0kV   X60,000   100nm   WD 10.0mm
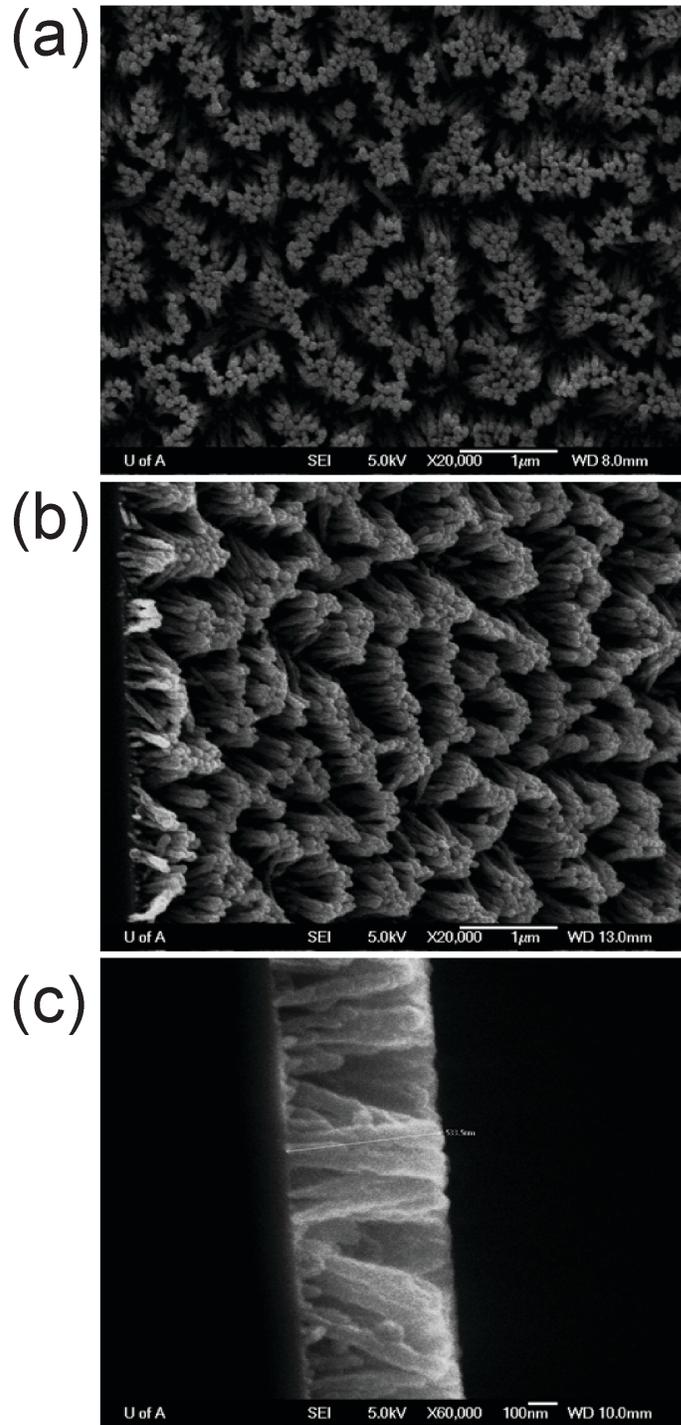
Figure 4.10 SEM images of a 500 nm thick Si GLAD films functionalized with trichloro (1*H*, 1*H*, 2*H*, 2*H*-perfluorooctyl) silane resulting in a poor quality film with (a) top view, (b) tilted view and (c) cross view.

4.3.3 Functionalized Si GLAD Films Performance

4.3.3.1 UV-Ozone Treatment Study

UV-Ozone cleaning treatment was reported to be effective to remove adsorbed hydrocarbons from the bare Si GLAD film surfaces.[22] We investigated the performance of UV-Ozone treatment on the silylated surfaces. Prior to the sample deposition of 10 μM asparagine and 10 μM histidine, the functionalized films were treated with UV-Ozone cleaner for 2, 5 and 15 min, respectively. The silylated surfaces without UV-Ozone treatment presented better performance, as shown in mass spectra in Figure 4.11.a-d and Figure 4.12.a-d. UV-Ozone treatment failure to clean the silylated surfaces may be due to the oxidation of the fluorocarbon molecules giving a noisier background.
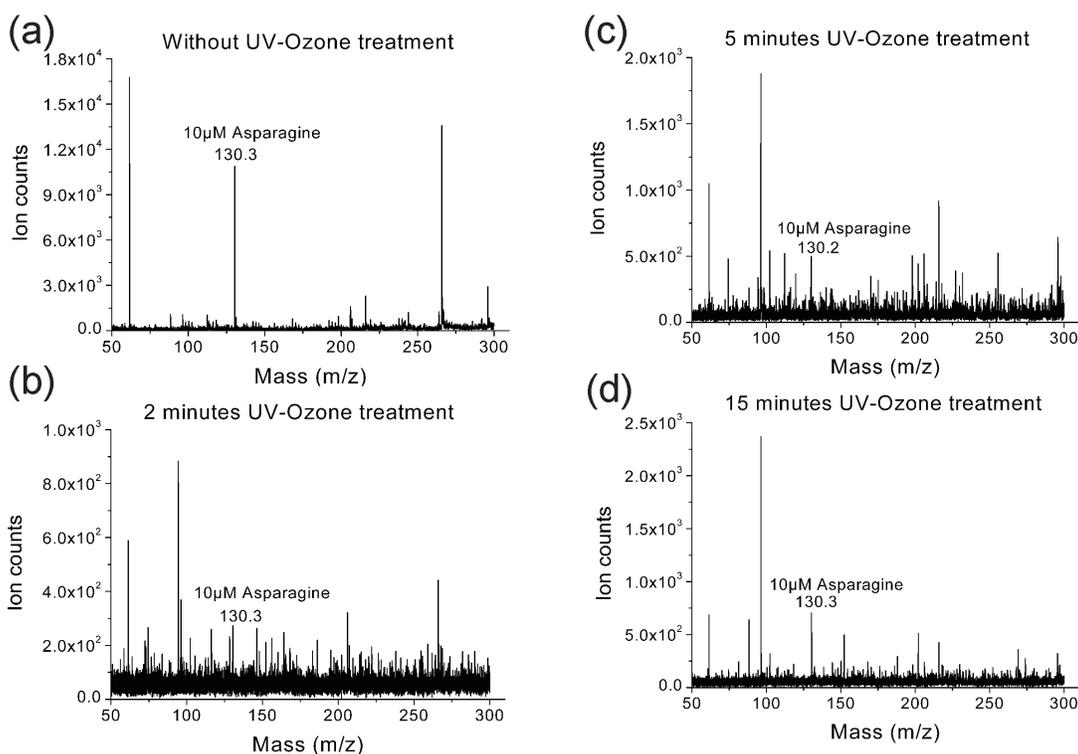
Figure 4.11 Asparagine (m/z=130.2) was detected on different UV-O treatments films; (a) 10 μM asparagine, none UV-O treatment, (b) 10 μM asparagine, 2 min UV-O treatment, (c) 10 μM asparagine, 5 min UV-O treatment and (d) 10 μM asparagine, 15 min UV-O treatment.
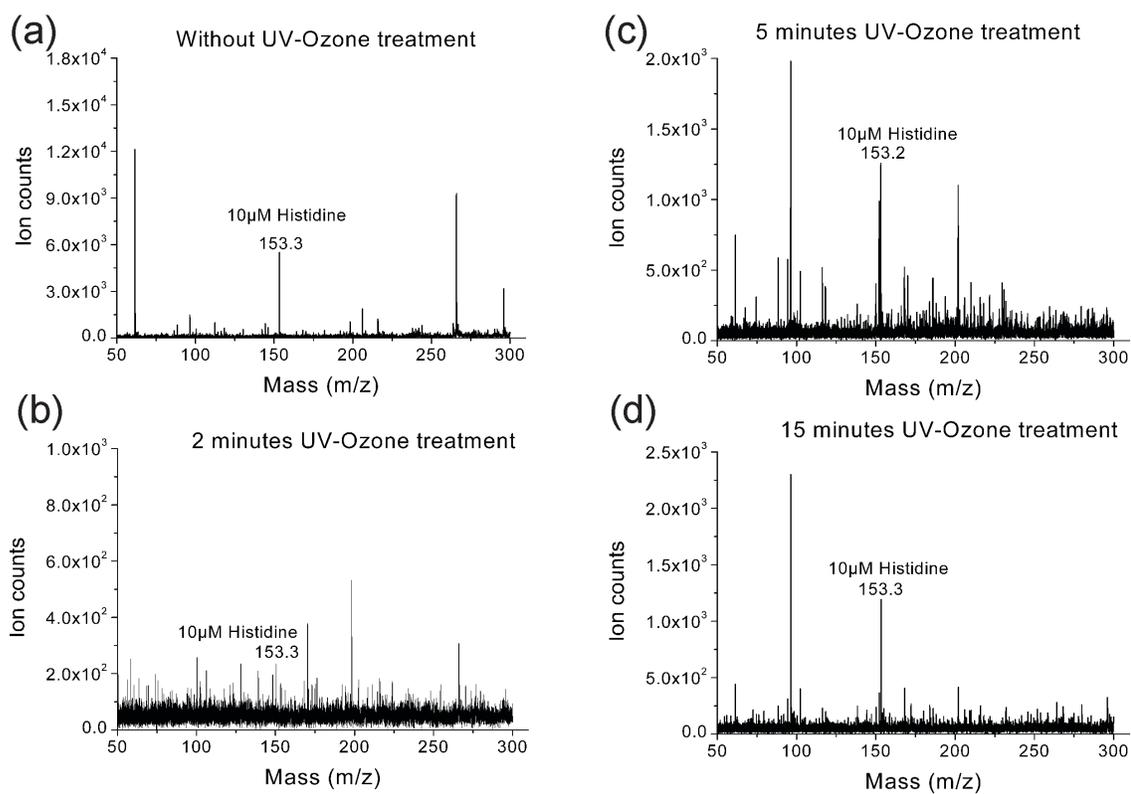
Figure 4.12 Histidine (m/z=153.2) was detected on different UV-O treatments films; (a) 10 μM histidine, none UV-O treatment, (b) 10 μM histidine, 2 min UV-O treatment, (c) 10 μM histidine, 5 min UV-O treatment and (d) 10 μM histidine, 15 min UV-O treatment.

4.3.3.2 Contact Angle Measurement

The contact angles on the surfaces are the result of three factors, the exposed chemical groups at the functionalized surface, the roughness of the surface, and the polarity of the droplets. We used contact angle measurement for two purposes. First, we measured the contact angles at four different positions on a 2 cm × 5 cm size film to evaluate the uniformity of the functionalized surfaces. The constant contact angle distribution on the surfaces, as shown in Figure 4.13, indicates that the silylated surfaces were uniform.
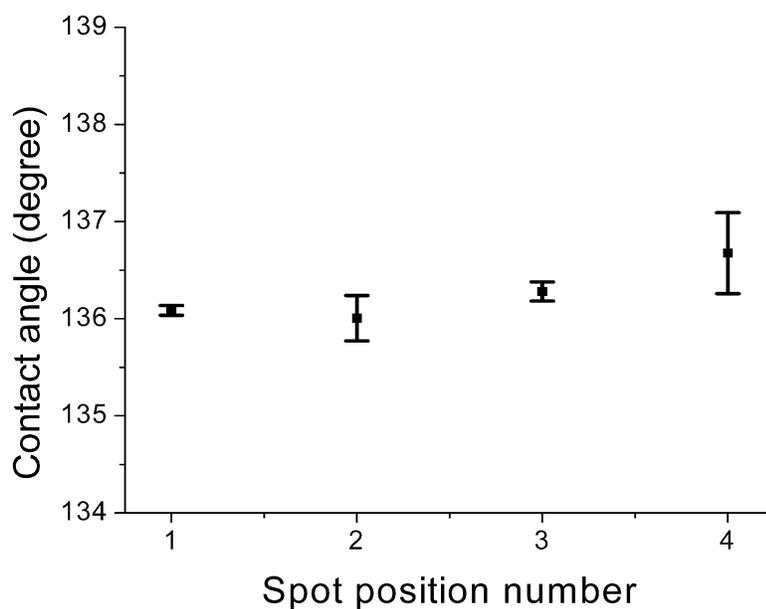
Figure 4.13 Contact angle of water droplet on different positions of the functionalized surfaces.

Second, we measured contact angles versus different methanol-in-water percentages to determine the relationship to sample spot size, as shown in Figure 4.14. The water droplet on the trichloro (1*H*, 1*H*, 2*H*, 2*H*-perfluorooctyl) silane functionalized surfaces exhibited a high contact angle as expected for fluorocarbon materials. As the percentage of methanol increased, the contact angle decreased, which is due to a decrease in the surface tension of the droplet. It is interesting to note that the contact angle shows the steepest change (from ~99° to ~25°) at methanol percentage between 70 to 80%. In the measurement of the formed spot size versus contact angles, the spot size did not linearly change with contact angles. When the methanol percentage was lower than 30%, the droplet size (~1 mm diameter) was too small for laser source alignment with the sample spots within the instrument. Finally, we chose to dilute our samples with methanol in a 1:1 ratio before SMALDI detection for two reasons, 1) the resultant spot size (~2 mm diameter) was desirable for mass spectrometry detection and 2) the droplet still presents a hydrophobic property on the surface, on which the dried sample is spread over a smaller area.
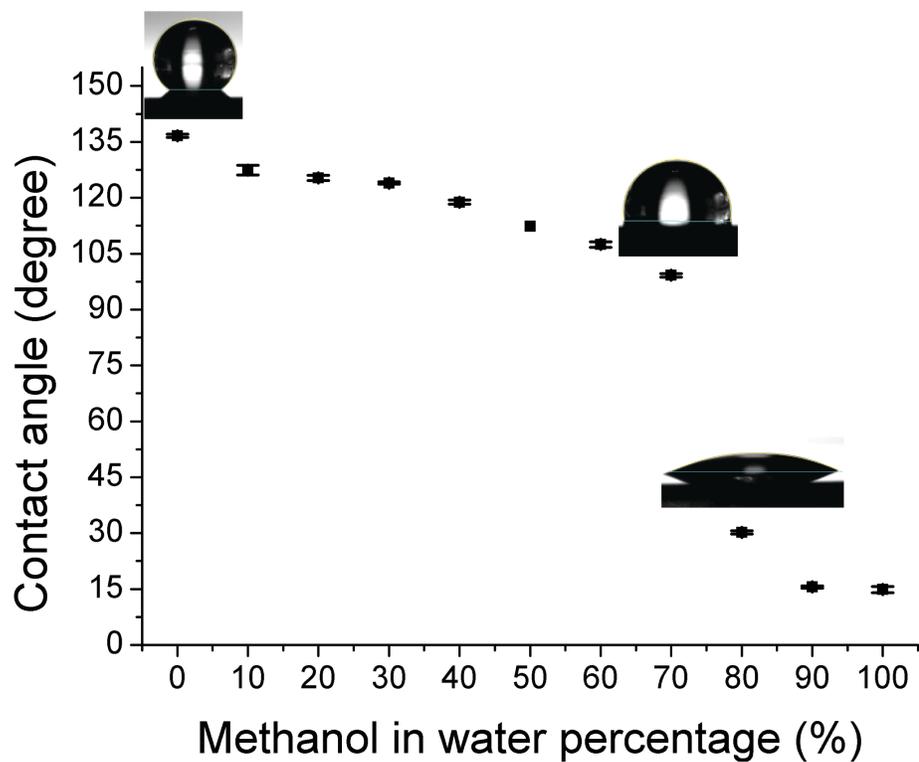
Figure 4.14 Contact angles versus methanol-in-water percentage.

4.3.3.4 Sensitivity of Functionalized Surfaces

Fonteh *et al* found that the concentrations of FAAs are significantly altered in samples from pAD compared with CT. For example, an important difference between pAD and CT is the decrease in histidine, which is normally found in the binding sites of heme proteins. The increase in glutamine concentration in the CSF of pAD compared with CT may suggest the loss of brain tissue.[104] In our study, the performance of silylated surfaces was evaluated with three amino acids, histidine, glutamine and asparagine, as shown in Figure 4.15. Amino acid samples were diluted by DI water to obtain a series of concentrations. For each concentration group, 10 μL amino acid solutions (asparagine, glutamine and histidine) and 10 μL methanol were mixed before SMALDI detection.
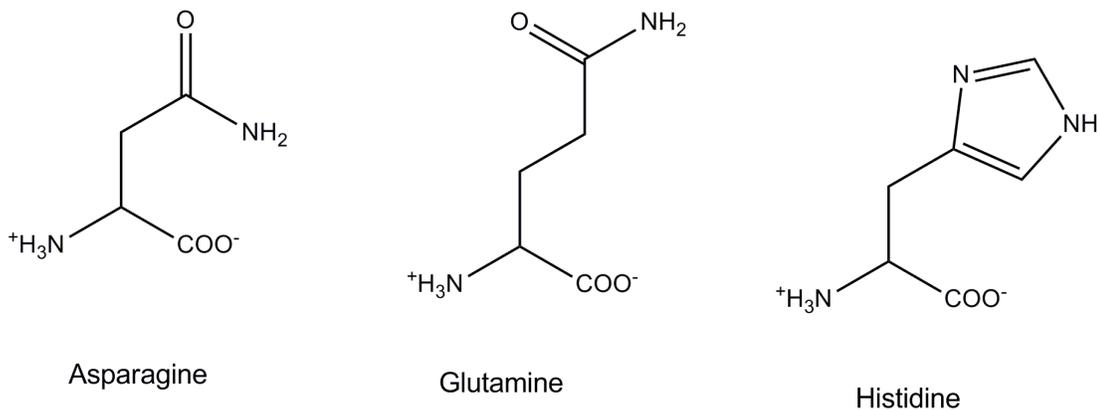
Figure 4.15 Amino acids structures

External calibration curves showed a linear peak height response in the concentration range of 0.1-30 μM as shown in Figure 4.16.a-c. A signal-to-noise ratio of 10:1 (S/N=10) for the samples was chosen when stating the LOD for two reasons. First, S/N=10 is the limit of quantitation, and this is the commonly used terminology in mass spectrometry. Second, due to the background noise and the chemical background noise in the low mass

range (50-300 Da), only when a peak exhibited a S/N greater than 10 could the peak be confidently considered to be an analyte peak. A LOD in the high femtomole range (asparagine ~400 fmol, glutamine ~300 fmol, and histidine ~300 fmol) levels was achieved for the silylated surfaces, as summarized in Table 4.2. These results suggest that the silylated surfaces can be used for quantitative studies. In CSF, the concentration of relevant amino acids, histidine, that change in patient evidencing pAD are ~8 μM, corresponding to ~6 pmol in a 2 mm spot made from a 0.8 μL volume deposit.

Table 4.2 LOD for pure FAA.

FAA	LOD (fmol)
Asparagine	468
Glutamine	335
Histidine	340
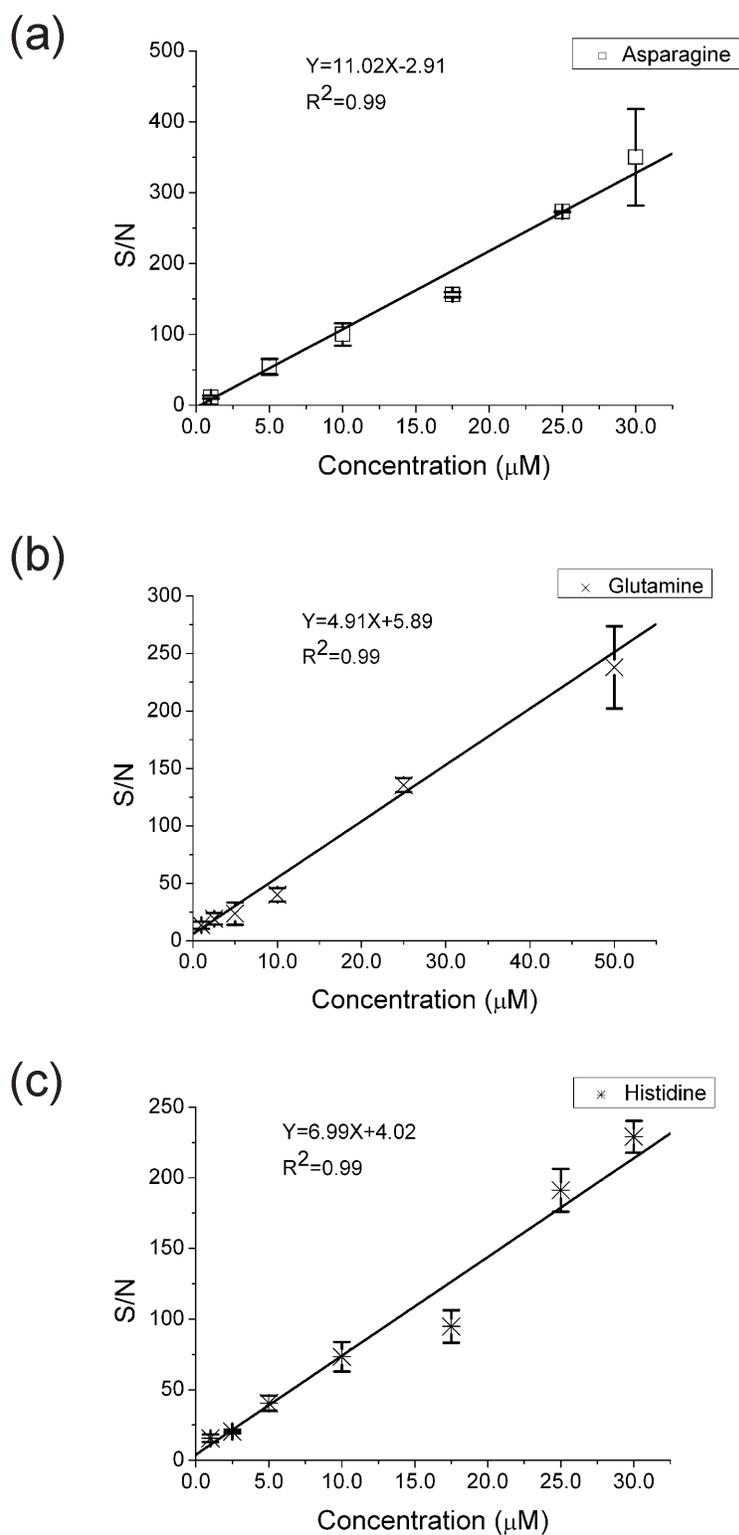
Figure 4.16 External calibration curves of pure samples; a) asparagine, b) glutamine and c) histidine. (n=10)

4.3.4 Quantitative Study of FAA Detection

4.3.4.1 Choice of Internal Standard

It must be pointed out that although the external calibration curves presented were well described by a linear regression, the data points for the external calibration were refined and selected in two steps. First, each data group (from high concentration to low concentration) went through a linear fit first and only the sets reasonably fit the linearly regression in the central region were kept, since in low concentration range, spot to spot variations become worse. In the high concentration range, the analytes showed a self-suppression effect. Secondly, these retained sets were further selected based on pairing similar laser intensities with similar peak height. In this way, for each FAA, usually at least 30 replicates were needed to get n=10 for the data in Figure 4.15. Therefore, the external calibration methods closely depend on the operator and on the assumption of a specific fit. This method would not be meaningful for identifying unknowns. To improve the quantitative study, we introduced an internal standard (IS) to the system. An appropriate IS for quantification should possess physical chemical properties that are common with those of the analytes.[117] Several studies reported the use of structural analogues,[118] derivatives,[119] functional analogues,[120] molecules of similar hydrophobicity,[117] or isotopically labeled derivatives of the analyte[121] as IS. In this study, we chose asparagine (MW=132) as IS because 1) asparagine and glutamine only differ by one methyl group in chemical structure and 2) asparagine changed less than 3% in CSF for pAD compared with CT, which can be considered as a constant concentration in CSF.[104]

4.3.4.2 Internal Calibration Curves of Pure Samples

Asparagine (MW=132) was the IS, which was diluted to 20 μM from the stock solution. Glutamine (MW=146) and histidine (MW=155) were diluted between 1 to 100 μM from the stock solutions. A 10 μL aliquot of the analyte, 10 μL IS and 20 μL methanol were mixed before SMALDI detection, so the concentrations were diluted a further four times. The final concentration of the IS was 5 μM and the final concentrations of the analytes were in the range of 0.25 to 25 μM. For each concentration, three replicates were prepared. For each solution, three sample spots were deposited by pipetting 0.8 μL of the mixture to the silylated surfaces. All data analyses were performed by averaging of 100 laser shots per spectrum, and each spectrum was collected starting from the middle and spreading out over the whole area within the sample spot. There was no data processing for the spectrum, as shown in Figure 4.17. The peak height ratios of the analyte peak relative to the IS peak were calculated and averaged from the nine measurements at each concentration. There was no data selection process for internal standard calibration. All the collected data were processed to get the calibration curves shown in Figure 4.18, which were constructed by plotting the peak height ratios of the analyte peak to the IS peak versus the concentration of the spiked analyte to the IS. All calibration curves were fit to a linear regression. We further analyzed the peak height of glutamine and corresponding IS, asparagine, separately as shown in Figure 4.18.b-c and the same for histidine-asparagine as shown in Figure 4.18.e-f. Look at Figure 4.18.b-c, glutamine at high concentration showed obvious ion suppression and the IS fixed that. And the noise is very large, the glutamine to IS ratio fixed that as shown in Figure 4.18.a. A similar result is seen for histidine, except there is not quite as much suppression for histidine as asparagine, as shown in Figure 4.18.e-f, so asparagine is not as good an IS for histidine as

it is for glutamine. Also as shown in Figure 4.18.d, the noise does not normalize as well for histidine-asparagine, as for glutamine-asparagine, showing again that asparagine is not quite as good an IS for histidine.
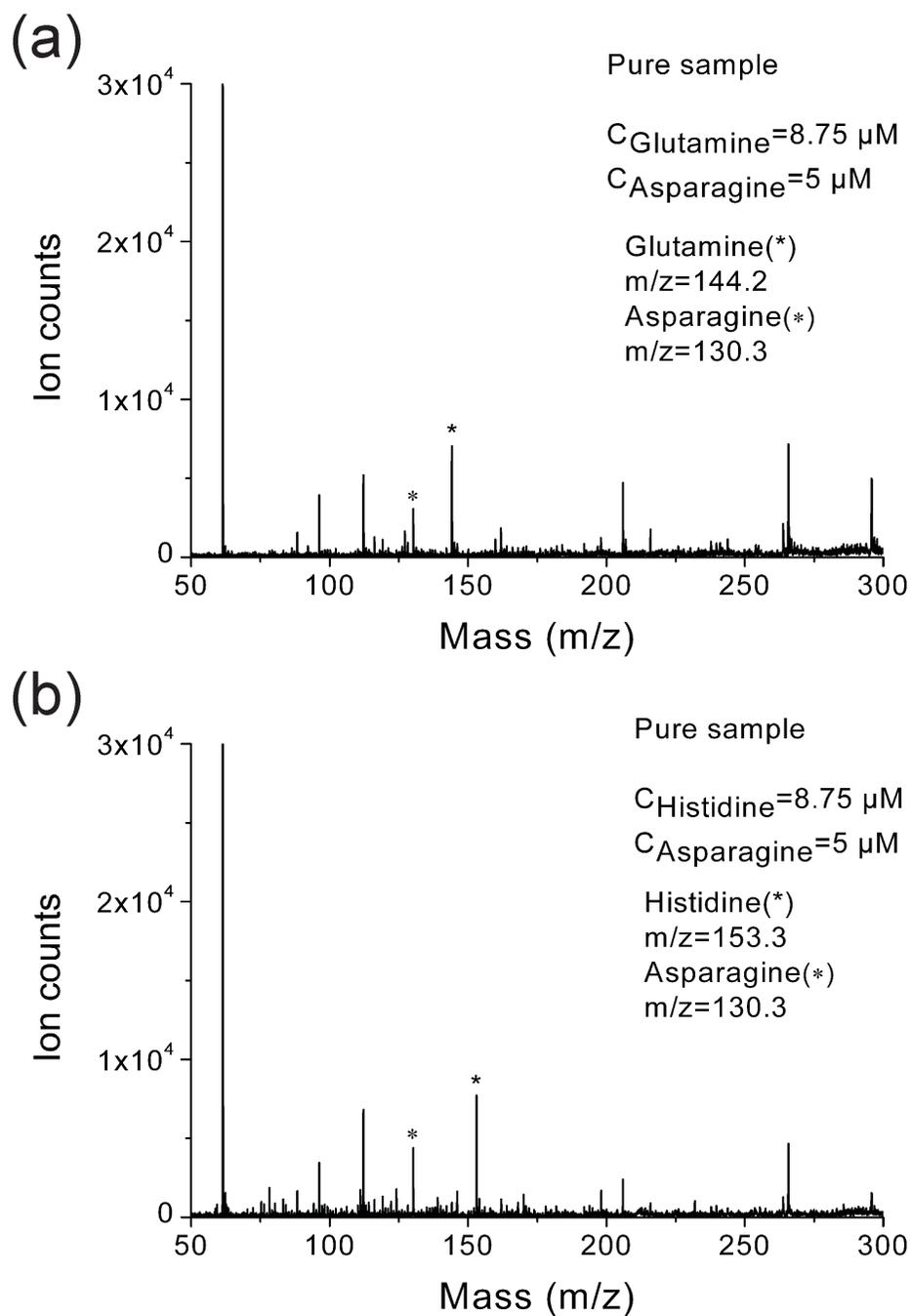
Figure 4.17 Mass spectra of pure samples: (a) glutamine-asparagine, (b) histidine-asparagine.

(a)

$Y=0.71X+0.31$

$R^2=0.99$

(b)

(c)
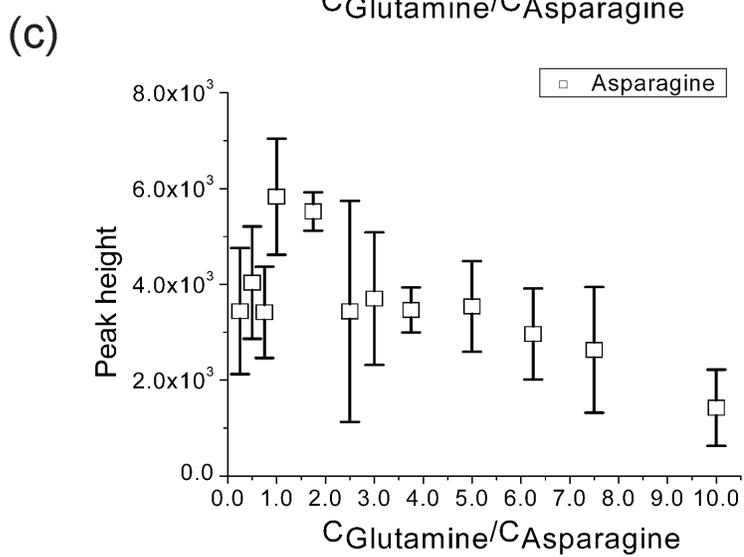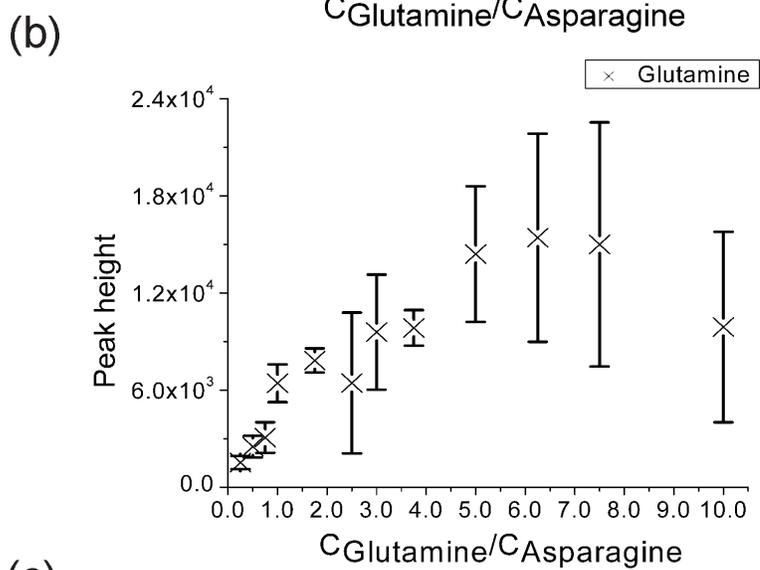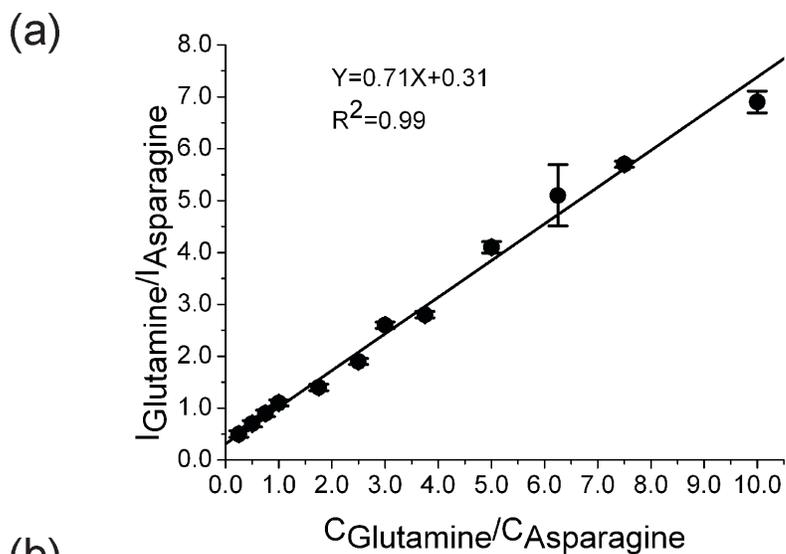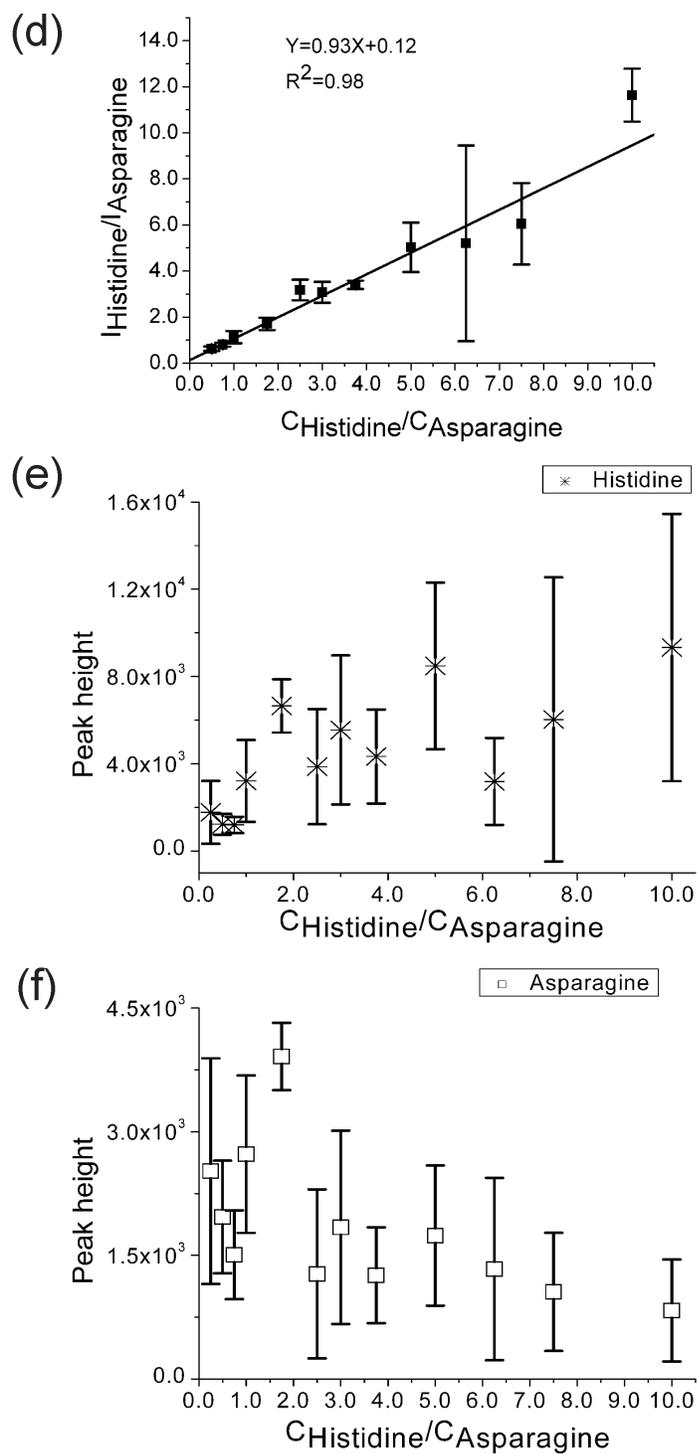
Figure 4.18 Internal calibration curves of pure samples; (a) glutamine-asparagine and (d) histidine-asparagine. Peak height analysis of (b) glutamine in glutamine-asparagine and (c) asparagine in glutamine-asparagine; (e) histidine in histidine-asparagine and (f) asparagine in histidine-asparagine. (n=9)

4.3.4.3 Internal Calibration Curves of Artificial CSF Samples

We further explored the analysis of FAA spiked in artificial CSF samples. The artificial CSF samples were prepared following the protocol of salt composition and concentrations from ALZET.[122] The ion concentrations are listed in Table 4.3.

Table 4.3 Artificial CSF composition and concentration (pH=7.3).

Ion in artificial CSF	Concentration (mM)
Na^+	150
K^+	3.0
Ca^{2+}	1.4
Mg^{2+}	0.8
PO_4^{3-}	1.0
Cl^-	155

Quantitative analysis of glutamine and histidine in artificial samples was performed using internal standard calibration. Asparagine (MW=132) was chosen as the IS. It was diluted by water to 20 μM from the stock solution. Glutamine (MW=146) and histidine (MW=155) were dissolved, then diluted with artificial CSF to between 10 to 100 μM from the stock solutions. A 10 μL aliquot of the analyte, 10 μL IS and 40 μL of methanol were mixed. The final concentration of the IS was 3.3 μM and the final concentrations of the analytes were in the range of 1.7 to 17 μM. We increased the methanol percentage because the size of the artificial CSF droplet (~1 mm) was too small to be aligned with the laser in the instrument. The artificial CSF sample is more polar than water, requiring a greater surface tension reduction. For each concentration, three replicates were prepared. For each solution, three sample spots were deposited by pipetting 1.2 μL of the mixture on the silylated surfaces. There was no rinsing step before SMALDI, to avoid the risk of washing out FAA at the same time. All data analyses were performed by averaging 100

laser shots per spectrum, and each spectrum was collected starting from the middle and spreading out over the whole area within the sample spot. There was no data processing for the spectrum, as shown in Figure 4.19. The peak height ratios of the analyte peaks relative to the IS peaks were calculated and averaged from the nine measurements at each concentration. Calibration curves, as shown in Figure 4.20, were constructed by plotting the peak height of the analyte to the internal standard versus the concentration of the spiked analyte to the internal standard. All calibration curves were fit to a linear regression. The calibration curve of glutamine and histidine spiked in artificial CSF using asparagine as the internal standard, measured on the silylated surfaces, showed acceptable linearity (R^2=0.96 and 0.97) in a working range of 5-50 μM. The plotted least squares fit weight by the standard deviation in the nine replicate data, gave a slope of m ± Δm (glutamine/asparagine 0.45 ± 0.03; histidine/asparagine 0.54 ± 0.02) and intercept of b ± Δb (glutamine/asparagine 0.58 ± 0.05; histidine/asparagine 0.44 ± 0.04). We also calculated that for a central observed value of analyte to IS peak height ratio (Y=1.5), the relative standard deviation in predicted concentration would be $\frac{\Delta concentration}{concentration} \times 100\%$, as summarized in Table 4.4. This range is larger than the expected reported physiological variations, illustrating that there will be a need to address the impact of sample salts on ionization efficiency. Alternatively, for pAD it may be necessary to select different biomarkers for use with this technique.

(a) Artificial sample

$C_{Glutamine}$=16.7 µM
$C_{Asparagine}$=3.3 µM
Glutamine(*)
m/z=144.2
Asparagine(∗)
m/z=130.3

(b) Artificial sample

$C_{Glutamine}$=6.25 µM
$C_{Asparagine}$=3.3 µM
Glutamine(*)
m/z=144.2
Asparagine(∗)
m/z=130.3

Continued on next page

(c)

Artificial sample

$C_{Histidine}$=16.7 μM
$C_{Asparagine}$=3.3 μM

Histidine(*)
m/z=153.3
Asparagine(∗)
m/z=130.3

(d)

Artificial sample

$C_{Histidine}$=6.25 μM
$C_{Asparagine}$=3.3 μM
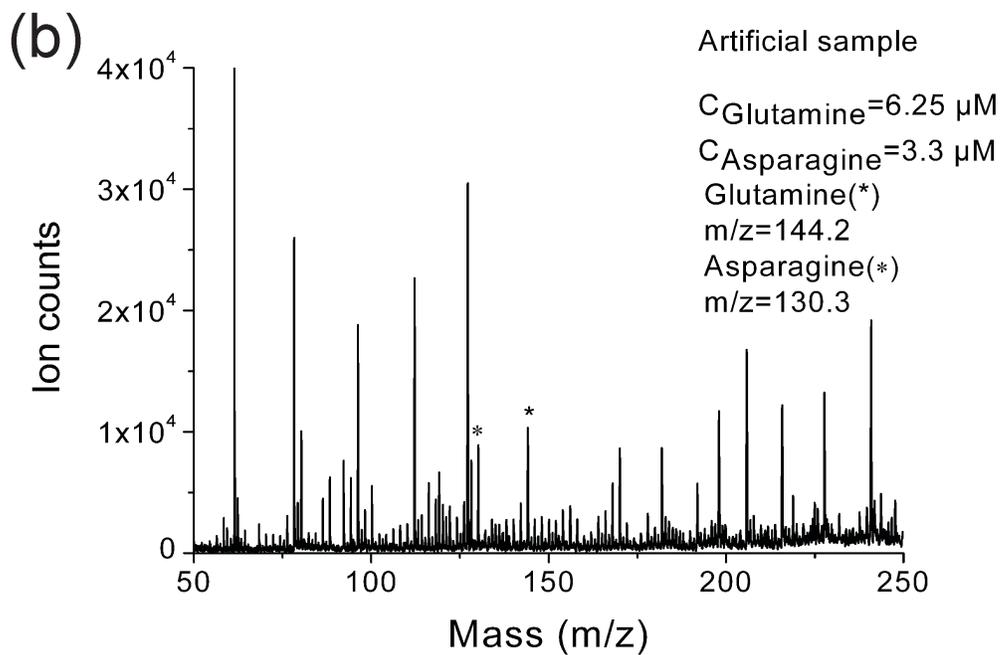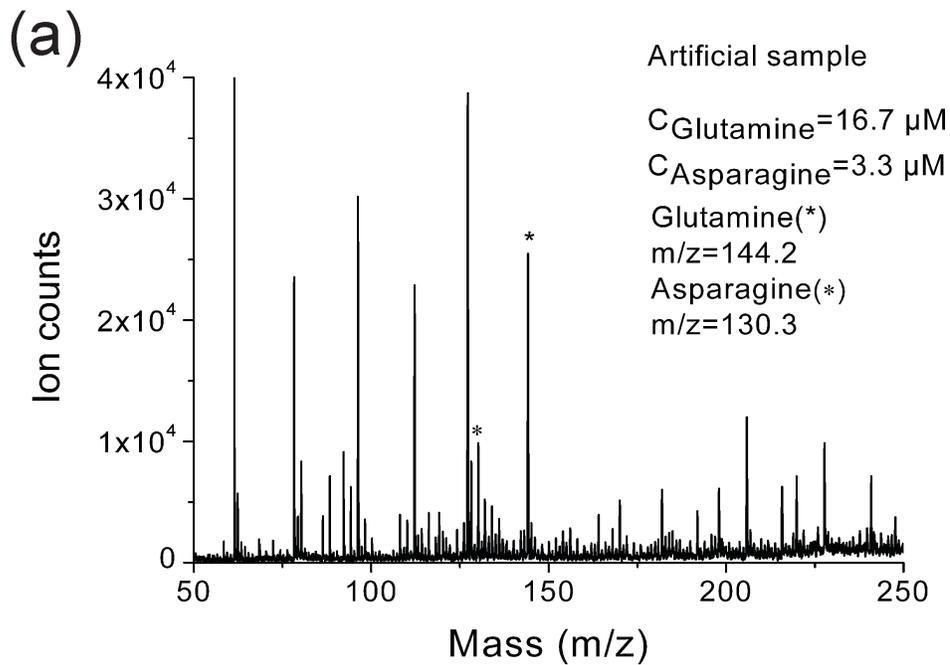
Histidine(*)
m/z=153.3
Asparagine(∗)
m/z=130.3
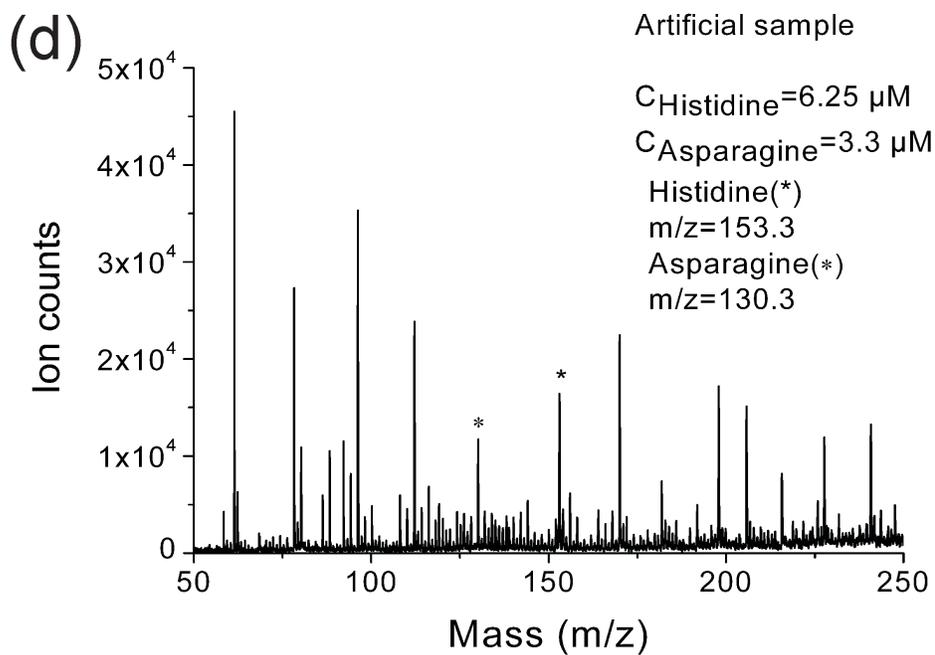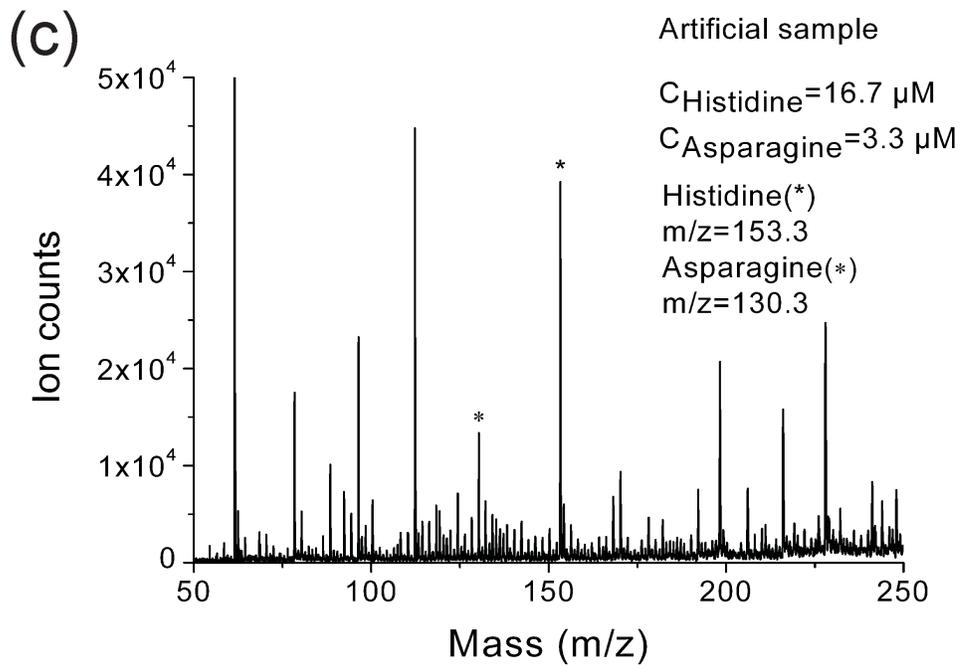
Figure 4.19 Mass spectra of artificial samples; (a-b) glutamine-asparagine and (c-d) histidine-asparagine.
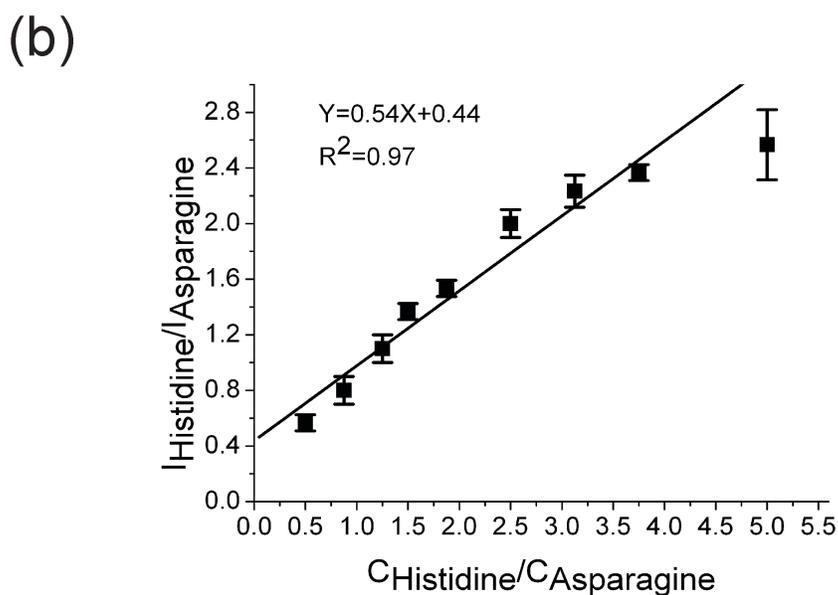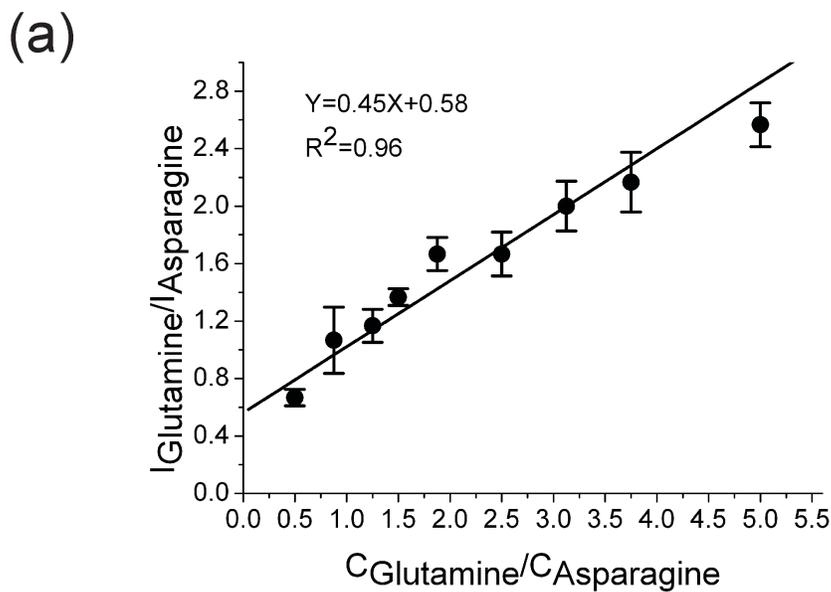
Figure 4.20 Internal calibration curves of spiked amino acids in artificial CSF samples; (a) glutamine-asparagine and (b) histidine-asparagine. (n=9)

Table 4.4 Comparison of the relative standard deviation of analytes concentration from least square fit and the physiological variation of pAD.

FAA	$\dfrac{\Delta concentration}{concentration} \times 100\%$	concentration in pAD (μM)[1]	pAD change [a] (% CT)[1]
Glutamine	$\pm 21\%$	1146 ± 10	5
Histidine	$\pm 29\%$	14 ± 6	-22

[a] The reported change in the mean concentration of FAA in pAD (n=8) compared to CT (n=8), which expressed as the % change.[1]

4.4 Conclusion

Our group has demonstrated the feasibility of using Si GLAD films for SMALDI in detection of small molecules. They optimized the morphology of Si GLAD films for MS efficiency.[22] Based on their studies, we developed silylated Si GLAD film surfaces that perform at low LOD for SMALDI detection of FAA. For pure FAA on bare Si GLAD film, the LOD were ~pmol, which would not work for the μM concentration range of FAA in CSF. For FAA on silylated Si GLAD film, the LOD were ~fmol in pure samples, which would work. However, in artificial CSF, they were ~pmol, which does not work, without using an IS. Quantitative analysis of artificial CSF sample spiked with different concentrations of glutamine and histidine showed a linear response in 5 to 50 μM, indicating that this silylated surface is suitable for metabolite quantification. Our results show the potential applicability of silylated surfaces to quantitatively analyze small metabolites in complex biological samples without pre-preparation.

Chapter 5 Conclusions and Future Work

5.1 Concluding Remarks

This thesis is directed towards new tools for biomarker analysis, which may also inform biomarker discovery. We report the investigation of silicon (Si) glancing angle deposition (GLAD) films applied to solid matrix laser desorption/ionization (SMALDI) mass spectrometry in proteomics and metabolomics. Three aspects were identified in which Si GLAD nanostructured films could potentially provide an opportunity for low-cost, fast SMALDI analysis: coupling with digital microfluidic (DMF) chips, immobilized-tryptic digestion and off-line analysis, and free amino acid (FAA) detection. Chapter 2 reports on DMF device fabrication and demonstrates a simple interface between a hydrophobic DMF surface and the hydrophilic GLAD films, which provides an attractive proof-of-concept that GLAD films are available for off-line SMALDI mass spectrometry detection. In Chapter 3, we introduce a ready-to-use chip, which is the silyated Si GLAD film, followed by immobilization of trypsin via covalent bonding. The performance of this chip is evaluated by digestion performance using cytochrome *c*. Although the result of immobilized-tryptic digestion does not show advantages compared with the result of free-solution tryptic digestion, it provides a SMALDI detectable modified surface. Our method showed lower detection limits (pmol) than previous reports on trypsin immobilization on porous Si, which cannot be detected without adding a matrix.[79] The resulting functionalized GLAD films may provide a low-cost and fast peptide mass fingerprinting (PMF) analysis. The performance for detection of free amino acids (FAA) by silylated Si GLAD films was investigated in Chapter 4. The reliability of the approach is

134

quantitatively demonstrated with calibration curves of asparagine, glutamine and histidine as pure samples, illustrating the sensitivity of the method for FAA detection is 400-fmol, 300-fmol, and 300-fmol levels, respectively. The overall results show the feasibility of extending the potential application of GLAD techniques in metobolomics, although the impact of salts on ionization efficiency remains to be overcome.

5.2 Future Work

In the work described in this dissertation, GLAD films were used for potential applications in proteomics and metabolomics. This current work with immobilized-tryptic digestion Si GLAD films demonstrates the proof-of-concept for *in situ* digestion of proteins for the rapid PMF. For future work, I anticipate this technique could be made compatible with on-tissue proteomic technologies for protein and peptide biomarkers discovery and analysis. I propose four stages to reach that goal. In the first stage we will optimize the scheme for immobilization trypsin on Si GLAD films and characterize the activity of the immobilized trypsin. We will identify the activity of the immobilized enzyme with MS using N_α-benzoyl-L-arginine ethylester hydrochloride (BAEE) as substrate, which will convert to the product N_α-benzoyl-L-arginine (B-arg), and N_α-benzoyloxycarbonyl-L-arginine (Z-arg) as internal standard.[79] In the second stage we will then assess the performance of the immobilized-tryptic Si GLAD films in terms of sensitivity, repeatability and robustness in MS and MS/MS experiments. These experiments will be carried out first with various synthetic tryptic peptide mixtures with no digestion, and then by *in situ* digestion of cocktails of proteins on the immobilized-tryptic Si GLAD films. In the third stage we will demonstrate the proof-of-concept of on-tissue digestion SMALDI imaging with MS/MS analysis. The advantage of GLAD films based SMALDI imaging is the homogeneity of signal generation that can improve the chemical spatial mapping resolution. To achieve SMALDI imaging, we will first learn how to mount the tissue on the immobilized-tryptic Si GLAD films and we will also need to build a raster with laser across tissue section in a defined pattern. In the spectra acquired on the digested tissue section, we will obtain molecular weight and intensity

information representative of the tryptic peptides, which can be plotted as the intensity of any measured ion as a function of individual pixel locations, to generate m/z specific images.[123] In the fourth stage we will direct attention towards optimizing the on-tissue digestion SMALDI imaging by exploring the film thickness, tissue sample thickness, and peptides enrichment in creating high quality images that are competitive or better than current technologies. Thus, as proposed here, GLAD films may be an ideally suited technology for on-tissue proteomic development, which can integrate efficiency *in-situ* digestion and identification of proteins from tissue section.

The results in Chapter 4 suggested the possibility of using GLAD films for SMALDI detection of FAA in real samples, but these results represent only the first step of many. The current limit of detection (LOD) is about 1 μM for FAA in pure buffers, but only 0.1 to 1 mM in artificial CSF samples. Therefore, we first need to confirm the magnitude of challenge that the salts present in CSF create for the assay of FAA by SMALDI mass spectrometry measurements in CSF. We will then go on to sample preparation, such as simple washing steps to bring the LOD in CSF back to 1 to 10 μM. For example, we will develop different ionic coatings for the GLAD films to trap ions of interest by ion exchange, and allow rinsing to remove excess salt, reducing overall salt interference from CSF. We will further develop methods to derivatize the FAA, following literature based protocols, such as differential isotope labeling[124]. These are used to enhance LOD, improve precision of measurement, and provide improved quantitative analysis.

To summarize, GLAD films could be easily integrated into mass spectrometry systems, and would add a versatile tool to surface modification, providing a platform for detection

of biomolecules. One can envision such a technique where proteomics or metabolomics

products onto GLAD films for the application in biomarker discovery or analysis.

References

1.   Gomez-Ramirez, J.; Wu, J., Network based biomarkers in Alzheimer's disease: review and future directions. *Frontiers in aging neuroscience* 2014, 6.

2.   Hernández, J.; Thompson, I. M., Prostate-specific antigen: A review of the validation of the most commonly used cancer biomarker. *Cancer* 2004, 101, 894-904.

3.   Zürbig, P.; Jahn, H., Use of proteomic methods in the analysis of human body fluids in Alzheimer research. *Electrophoresis* 2012, 33, 3617-3630.

4.   Henry, M. S.; Passmore, A. P.; Todd, S.; McGuinness, B.; Craig, D.; Johnston, J. A., The development of effective biomarkers for Alzheimer's disease: a review. *International journal of geriatric psychiatry* 2013, 28, 331-340.

5.   Zetterberg, H.; Rüetschi, U.; Portelius, E.; Brinkmalm, G.; Andreasson, U.; Blennow, K.; Brinkmalm, A., Clinical proteomics in neurodegenerative disorders. *Acta neurologica Scandinavica* 2008, 118, 1-11.

6.   Teichert, F.; Verschoyle, R. D.; Greaves, P.; Edwards, R. E.; Teahan, O.; Jones, D. J. L.; Wilson, I. D.; Farmer, P. B.; Steward, W. P.; Gant, T. W.; Gescher, A. J.; Keun, H. C., Metabolic profiling of transgenic adenocarcinoma of mouse prostate (TRAMP) Tissue by 1H-NMR analysis: evidence for unusual phospholipid metabolism. *The Prostate* 2008, 68, 1035-1047.

7.   Zhang, J.; Wei, S.; Liu, L.; Nagana Gowda, G. A.; Bonney, P.; Stewart, J.; Knapp, D. W.; Raftery, D., NMR-based metabolomics study of canine bladder cancer. *Biochimica et Biophysica Acta (BBA) - Molecular Basis of Disease* 2012, 1822, 1807-1814.

8.   Wu, H.; Xue, R.; Lu, C.; Deng, C.; Liu, T.; Zeng, H.; Wang, Q.; Shen, X., Metabolomic study for diagnostic model of oesophageal cancer using gas chromatography/mass spectrometry. *Journal of Chromatography B* 2009, 877, 3111-3117.

9.   Ganti, S.; Taylor, S. L.; Abu Aboud, O.; Yang, J.; Evans, C.; Osier, M. V.; Alexander, D. C.; Kim, K.; Weiss, R. H., Kidney Tumor Biomarkers Revealed by Simultaneous Multiple Matrix Metabolomics Analysis. *Cancer research* 2012, 72, 3471-3479.

10.   Lv, W.; Yang, T., Identification of possible biomarkers for breast cancer from free fatty acid profiles determined by GC–MS and multivariate statistical analysis. *Clinical biochemistry* 2012, 45, 127-133.

11.   Li, F.; Qin, X.; Chen, H.; Qiu, L.; Guo, Y.; Liu, H.; Chen, G.; Song, G.; Wang, X.; Li, F.; Guo, S.; Wang, B.; Li, Z., Lipid profiling for early diagnosis and progression of colorectal cancer using direct-infusion electrospray ionization Fourier transform ion cyclotron resonance mass spectrometry. *Rapid Communications in Mass Spectrometry* 2013, 27, 24-34.

12.   Zhang, T.; Wu, X.; Ke, C.; Yin, M.; Li, Z.; Fan, L.; Zhang, W.; Zhang, H.; Zhao, F.; Zhou, X.; Lou, G.; Li, K., Identification of Potential Biomarkers for Ovarian Cancer by Urinary Metabolomic Profiling. *Journal of proteome research* 2012, 12, 505-512.

13.   Chen, J.; Zhou, L.; Zhang, X.; Lu, X.; Cao, R.; Xu, C.; Xu, G., Urinary hydrophilic and hydrophobic metabolic profiling based on liquid chromatography-mass spectrometry methods: Differential metabolite discovery specific to ovarian cancer. *Electrophoresis* 2012, 33, 3361-3369.

14.   Ibáñez, C.; Simó, C.; García-Cañas, V.; Gómez-Martínez, Á.; Ferragut, J. A.; Cifuentes, A., CE/LC-MS multiplatform for broad metabolomic analysis of dietary polyphenols effect on colon cancer cells proliferation. *Electrophoresis* 2012, 33, 2328-2336.

15.   Sugimoto, M.; Wong, D.; Hirayama, A.; Soga, T.; Tomita, M., Capillary electrophoresis mass spectrometry-based saliva metabolomics identified oral, breast and pancreatic cancer-specific profiles. *Metabolomics : Official journal of the Metabolomic Society* 2010, 6, 78-95.

16.   Garbis, S.; Lubec, G.; Fountoulakis, M., Limitations of current proteomics technologies. *Journal of Chromatography A* 2005, 1077, 1-18.

17.   Chen, C.-H., Review of a current role of mass spectrometry for proteome research. *Analytica chimica acta* 2008, 624, 16-36.

18.   Becker, S.; Kortz, L.; Helmschrodt, C.; Thiery, J.; Ceglarek, U., LC–MS-based metabolomics in the clinical laboratory. *Journal of Chromatography B* 2012, 883–884, 68-75.

19.   Villas-Bôas, S. G.; Mas, S.; Åkesson, M.; Smedsgaard, J.; Nielsen, J., Mass spectrometry in metabolome analysis. *Mass spectrometry reviews* 2005, 24, 613-646.

20.   Khan, M. F.; Bennett, M. J.; Jumper, C. C.; Percy, A. J.; Silva, L. P.; Schriemer, D. C., Proteomics by mass spectrometry—Go big or go home? *Journal of pharmaceutical and biomedical analysis* 2011, 55, 832-841.

21.   Wei, J.; Buriak, J. M.; Siuzdak, G., Desorption-ionization mass spectrometry on porous silicon. *Nature* 1999, 399, 243-246.

22.   Jemere, A. B.; Bezuidenhout, L. W.; Brett, M. J.; Harrison, D. J., Matrix‐free laser desorption/ionization mass spectrometry using silicon glancing angle deposition (GLAD) films. *Rapid Communications in Mass Spectrometry* 2010, 24, 2305-2311.

23.   Karas, M.; Hillenkamp, F., Laser desorption ionization of proteins with molecular masses exceeding 10,000 daltons. *Analytical Chemistry* 1988, 60, 2299-2301.

24.   Knochenmuss, R., Ion formation mechanisms in UV-MALDI. *The Analyst* 2006, 131, 966-986.

25.   Dai, Y.; Whittal, R. M.; Li, L., Two-Layer Sample Preparation: A Method for MALDI-MS Analysis of Complex Peptide and Protein Mixtures. *Analytical Chemistry* 1999, 71, 1087-1091.

26.   Alimpiev, S.; Grechnikov, A.; Sunner, J.; Karavanskii, V.; Simanovsky, Y.; Zhabin, S.; Nikiforov, S., On the role of defects and surface chemistry for surface-assisted laser desorption ionization from silicon. *The Journal of chemical physics* 2008, 128, -.

27.   Northen, T. R.; Yanes, O.; Northen, M. T.; Marrinucci, D.; Uritboonthai, W.; Apon, J.; Golledge, S. L.; Nordstrom, A.; Siuzdak, G., Clathrate nanostructures for mass spectrometry. *Nature* 2007, 449, 1033-1036.

28.   Woo, H.-K.; Northen, T. R.; Yanes, O.; Siuzdak, G., Nanostructure-initiator mass spectrometry: a protocol for preparing and applying NIMS surfaces for high-sensitivity mass analysis. *Nat. Protocols* 2008, 3, 1341-1349.

29.   Kiema, G. K.; Jensen, M. O.; Brett, M. J., Glancing Angle Deposition Thin Film Microstructures for Microfluidic Applications. *Chemistry of Materials* 2005, 17, 4046-4048.

30.   Hawkeye, M. M.; Brett, M. J., Glancing angle deposition: Fabrication, properties, and applications of micro- and nanostructured thin films. *Journal of Vacuum Science & Technology A* 2007, 25, 1317-1335.

31.   Steele, J. J.; Taschuk, M. T.; Brett, M. J., Nanostructured Metal Oxide Thin Films for Humidity Sensors. *Sensors Journal, IEEE* 2008, 8, 1422-1429.

32.   Zhang, W.; Ganesh, N.; Block, I. D.; Cunningham, B. T., High sensitivity photonic crystal biosensor incorporating nanorod structures for enhanced surface area. *Sensors and Actuators B: Chemical* 2008, 131, 279-284.

33.   Gish, D. A.; Nsiah, F.; McDermott, M. T.; Brett, M. J., Localized Surface Plasmon Resonance Biosensor Using Silver Nanostructures Fabricated by Glancing Angle Deposition. *Analytical Chemistry* 2007, 79, 4228-4232.

34.   Chu, H. V.; Liu, Y.; Huang, Y.; Zhao, Y., A high sensitive fiber SERS probe based on silver nanorod arrays. *Optics express* 2007, 15, 12230-12239.

35.   Shanmukh, S.; Jones, L.; Driskell, J.; Zhao, Y.; Dluhy, R.; Tripp, R. A., Rapid and Sensitive Detection of Respiratory Virus Molecular Signatures Using a Silver Nanorod Array SERS Substrate. *Nano Letters* 2006, 6, 2630-2636.

36.   Driskell, J. D.; Seto, A. G.; Jones, L. P.; Jokela, S.; Dluhy, R. A.; Zhao, Y. P.; Tripp, R. A., Rapid microRNA (miRNA) detection and classification via surface-enhanced Raman spectroscopy (SERS). *Biosensors and Bioelectronics* 2008, 24, 917-922.

37.   Bezuidenhout, L. W.; Nazemifard, N.; Jemere, A. B.; Harrison, D. J.; Brett, M. J., Microchannels filled with diverse micro- and nanostructures fabricated by glancing angle deposition. *Lab on a chip* 2011, 11, 1671-1678.

38.   Bezuidenhout, L. W.; Brett, M. J., Ultrathin layer chromatography on nanostructured thin films. *Journal of Chromatography A* 2008, 1183, 179-185.

39.   Kirchert, S.; Wang, Z.; Taschuk, M.; Jim, S.; Brett, M.; Morlock, G., Inkjet application, chromatography, and mass spectrometry of sugars on nanostructured thin films. *Analytical and bioanalytical chemistry* 2013, 405, 7195-7203.

40.   Kumar, S.; Kumar, S.; Ali, M. A.; Anand, P.; Agrawal, V. V.; John, R.; Maji, S.; Malhotra, B. D., Microfluidic-integrated biosensors: Prospects for point-of-care diagnostics. *Biotechnology journal* 2013, 8, 1267-1279.

41.   Berthier, J., *Micro-drops and digital microfluidics*. William Andrew: 2012.

42.   Fair, R. B.; Khlystov, A.; Tailor, T. D.; Ivanov, V.; Evans, R. D.; Griffin, P. B.; Vijay, S.; Pamula, V. K.; Pollack, M. G.; Zhou, J., Chemical and Biological Applications of Digital-Microfluidic Devices. *Design & Test of Computers, IEEE* 2007, 24, 10-24.

43.   Teh, S.-Y.; Lin, R.; Hung, L.-H.; Lee, A. P., Droplet microfluidics. *Lab on a chip* 2008, 8, 198-220.

44.   Abdelgawad, M.; Wheeler, A. R., The Digital Revolution: A New Paradigm for Microfluidics. *Advanced Materials* 2009, 21, 920-925.

45.   Jebrail, M. J.; Wheeler, A. R., Let's get digital: digitizing chemical biology with microfluidics. *Current opinion in chemical biology* 2010, 14, 574-581.

46.   Abdelgawad, M.; Freire, S. L.; Yang, H.; Wheeler, A. R., All-terrain droplet actuation. *Lab on a chip* 2008, 8, 672-677.

47.   Gong, J., All-electronic droplet generation on-chip with real-time feedback control for EWOD digital microfluidics. *Lab on a chip* 2008, 8, 898-906.

48.   Malic, L.; Veres, T.; Tabrizian, M., Biochip functionalization using electrowetting-on-dielectric digital microfluidics for surface plasmon resonance imaging detection of DNA hybridization. *Biosensors and Bioelectronics* 2009, 24, 2218-2224.

49.   Cho, S. K.; Zhao, Y., Concentration and binary separation of micro particles for droplet-based digital microfluidics. *Lab on a chip* 2007, 7, 490-498.

50.   Barbulovic-Nad, I.; Yang, H.; Park, P. S.; Wheeler, A. R., Digital microfluidics for cell-based assays. *Lab on a chip* 2008, 8, 519-526.

51.   Wang, Y.; Zhao, Y.; Cho, S. K., Efficient in-droplet separation of magnetic particles for digital microfluidics. *Journal of Micromechanics and Microengineering* 2007, 17, 2148.

52.   Luk, V. N.; Mo, G. C.; Wheeler, A. R., Pluronic additives: a solution to sticky problems in digital microfluidics. *Langmuir* 2008, 24, 6382-6389.

53.   Abdelgawad, M.; Watson, M. W.; Wheeler, A. R., Hybrid microfluidics: A digital-to-channel interface for in-line sample processing and chemical separations. *Lab on a chip* 2009, 9, 1046-1051.

54.   Chang, Y.-H.; Lee, G.-B.; Huang, F.-C.; Chen, Y.-Y.; Lin, J.-L., Integrated polymerase chain reaction chips utilizing digital microfluidics. *Biomedical microdevices* 2006, 8, 215-225.

55.   Wheeler, A. R.; Moon, H.; Bird, C. A.; Ogorzalek Loo, R. R.; Kim, C.-J. C.; Loo, J. A.; Garrell, R. L., Digital microfluidics with in-line sample purification for proteomics analyses with MALDI-MS. *Analytical Chemistry* 2005, 77, 534-540.

56.   Verheijen, H.; Prins, M., Reversible electrowetting and trapping of charge: model and experiments. *Langmuir* 1999, 15, 6616-6620.

57.   Liu, Y.-J.; Yao, D.-J.; Lin, H.-C.; Chang, W.-Y.; Chang, H.-Y., DNA ligation of ultramicro volume using an EWOD microfluidic system with coplanar electrodes. *Journal of Micromechanics and Microengineering* 2008, 18, 045017.

58. Taniguchi, T.; Torii, T.; Higuchi, T., Chemical reactions in microdroplets by electrostatic manipulation of droplets in liquid media. *Lab on a chip* 2002, 2, 19-23.

59. Srinivasan, V.; Pamula, V. K.; Fair, R. B., An integrated digital microfluidic lab-on-a-chip for clinical diagnostics on human physiological fluids. *Lab on a chip* 2004, 4, 310-315.

60. Sista, R. S.; Eckhardt, A. E.; Wang, T.; Graham, C.; Rouse, J. L.; Norton, S. M.; Srinivasan, V.; Pollack, M. G.; Tolun, A. A.; Bali, D., Digital microfluidic platform for multiplexing enzyme assays: implications for lysosomal storage disease screening in newborns. *Clinical chemistry* 2011, 57, 1444-1451.

61. Ng, A. H.; Choi, K.; Luoma, R. P.; Robinson, J. M.; Wheeler, A. R., Digital microfluidic magnetic separation for particle-based immunoassays. *Analytical chemistry* 2012, 84, 8805-8812.

62. Choi, K.; Ng, A. H.; Fobel, R.; Chang-Yen, D. A.; Yarnell, L. E.; Pearson, E. L.; Oleksak, C. M.; Fischer, A. T.; Luoma, R. P.; Robinson, J. M., Automated Digital Microfluidic Platform for Magnetic-Particle-Based Immunoassays with Optimization by Design of Experiments. *Analytical chemistry* 2013, 85, 9638-9646.

63. Bogojevic, D.; Chamberlain, M. D.; Barbulovic-Nad, I.; Wheeler, A. R., A digital microfluidic method for multiplexed cell-based apoptosis assays. *Lab on a chip* 2012, 12, 627-634.

64. Au, S. H.; Fobel, R.; Desai, S. P.; Voldman, J.; Wheeler, A. R., Cellular bias on the microscale: probing the effects of digital microfluidic actuation on mammalian cell health, fitness and phenotype. *Integrative Biology* 2013, 5, 1014-1025.

65.   Moon, H.; Wheeler, A. R.; Garrell, R. L.; Loo, J. A., An integrated digital microfluidic chip for multiplexed proteomic sample preparation and analysis by MALDI-MS. *Lab on a chip* 2006, 6, 1213-1219.

66.   Luk, V. N.; Wheeler, A. R., A digital microfluidic approach to proteomic sample processing. *Analytical chemistry* 2009, 81, 4524-4530.

67.   Luk, V. N.; Fiddes, L. K.; Luk, V. M.; Kumacheva, E.; Wheeler, A. R., Digital microfluidic hydrogel microreactors for proteomics. *Proteomics* 2012, 12, 1310-1318.

68.   Krenkova, J.; Svec, F., Less common applications of monoliths: IV. Recent developments in immobilized enzyme reactors for proteomics and biotechnology. *Journal of separation science* 2009, 32, 706-718.

69.   Ma, J.; Zhang, L.; Liang, Z.; Shan, Y.; Zhang, Y., Immobilized enzyme reactors in proteomics. *TrAC Trends in Analytical Chemistry* 2011, 30, 691-702.

70.   Schoenherr, R. M.; Ye, M.; Vannatta, M.; Dovichi, N. J., CE-microreactor-CE-MS/MS for protein analysis. *Analytical chemistry* 2007, 79, 2230-2238.

71.   Kato, M.; Sakai-Kato, K.; Jin, H.; Kubota, K.; Miyano, H.; Toyo'oka, T.; Dulay, M. T.; Zare, R. N., Integration of on-line protein digestion, peptide separation, and protein identification using pepsin-coated photopolymerized sol-gel columns and capillary electrophoresis/mass spectrometry. *Analytical chemistry* 2004, 76, 1896-1902.

72.   Slysz, G. W.; Schriemer, D. C., Blending protein separation and peptide analysis through real-time proteolytic digestion. *Analytical chemistry* 2005, 77, 1572-1579.

73.   Feng, S.; Ye, M.; Jiang, X.; Jin, W.; Zou, H., Coupling the immobilized trypsin microreactor of monolithic capillary with μRPLC-MS/MS for shotgun proteome analysis. *Journal of proteome research* 2006, 5, 422-428.

74.   Yuan, H.; Zhang, L.; Hou, C.; Zhu, G.; Tao, D.; Liang, Z.; Zhang, Y., Integrated platform for proteome analysis with combination of protein and peptide separation via online digestion. *Analytical chemistry* 2009, 81, 8708-8714.

75.   Temporini, C.; Perani, E.; Mancini, F.; Bartolini, M.; Calleri, E.; Lubda, D.; Felix, G.; Andrisano, V.; Massolini, G., Optimization of a trypsin-bioreactor coupled with high-performance liquid chromatography–electrospray ionization tandem mass spectrometry for quality control of biotechnological drugs. *Journal of Chromatography A* 2006, 1120, 121-131.

76.   Chen, W.-Y.; Chen, Y.-C., Acceleration of microwave-assisted enzymatic digestion reactions by magnetite beads. *Analytical chemistry* 2007, 79, 2394-2401.

77.   Lin, S.; Yao, G.; Qi, D.; Li, Y.; Deng, C.; Yang, P.; Zhang, X., Fast and efficient proteolysis by microwave-assisted protein digestion using trypsin-immobilized magnetic silica microspheres. *Analytical chemistry* 2008, 80, 3655-3665.

78.   Ekström, S.; Önnerfjord, P.; Nilsson, J.; Bengtsson, M.; Laurell, T.; Marko-Varga, G., Integrated microanalytical technology enabling rapid and automated protein identification. *Analytical chemistry* 2000, 72, 286-293.

79.   Xu, S.; Pan, C.; Hu, L.; Zhang, Y.; Guo, Z.; Li, X.; Zou, H., Enzymatic reaction of the immobilized enzyme on porous silicon studied by matrix‐assisted laser desorption/ionization‐time of flight‐mass spectrometry. *Electrophoresis* 2004, 25, 3669-3676.

80.   Gao, J.; Xu, J.; Locascio, L. E.; Lee, C. S., Integrated microfluidic system enabling protein digestion, peptide separation, and protein identification. *Analytical Chemistry* 2001, 73, 2648-2655.

81.   Kjellander, M., Nanoporous Aluminum Oxide–A Promising Support for Modular Enzyme Reactors. 2013.

82.   Temporini, C.; Perani, E.; Calleri, E.; Dolcini, L.; Lubda, D.; Caccialanza, G.; Massolini, G., Pronase-immobilized enzyme reactor: an approach for automation in glycoprotein analysis by LC/LC-ESI/MS n. *Analytical chemistry* 2007, 79, 355-363.

83.   Temporini, C.; Dolcini, L.; Abee, A.; Calleri, E.; Galliano, M.; Caccialanza, G.; Massolini, G., Development of an integrated chromatographic system for on-line digestion and characterization of phosphorylated proteins. *Journal of Chromatography A* 2008, 1183, 65-75.

84.   Migneault, I.; Dartiguenave, C.; Bertrand, M. J.; Waldron, K. C., Glutaraldehyde: behavior in aqueous solution, reaction with proteins, and application to enzyme crosslinking. *Biotechniques* 2004, 37, 790-806.

85.   Monsan, P., Optimization of glutaraldehyde activation of a support for enzyme immobilization. *Journal of Molecular Catalysis* 1978, 3, 371-384.

86.   Richards, F.; Knowles, J., Glutaraldehyde as a protein cross-linking reagent. *Journal of molecular biology* 1968, 37, 231-233.

87.   Shih, S. C.; Yang, H.; Jebrail, M. J.; Fobel, R.; McIntosh, N.; Al-Dirbashi, O. Y.; Chakraborty, P.; Wheeler, A. R., Dried blood spot analysis by digital microfluidics coupled to nanoelectrospray ionization mass spectrometry. *Analytical chemistry* 2012, 84, 3731-3738.

88.   Lapierre, F.; Piret, G.; Drobecq, H.; Melnyk, O.; Coffinier, Y.; Thomy, V.; Boukherroub, R., High sensitive matrix-free mass spectrometry analysis of peptides using silicon nanowires-based digital microfluidic device. *Lab on a chip* 2011, 11, 1620-1628.

89.   Chen, E. b. P., Molecular Interfacial Phenomena of Polymers and Biopolymers, 1st Edition. *Woodhead Publishing* 2005.

90.   Loeb, G. E.; Bak, M.; Salcman, M.; Schmidt, E., Parylene as a chronically stable, reproducible microelectrode insulator. *Biomedical Engineering, IEEE Transactions on* 1977, 121-128.

91.   Schmidt, E.; McIntosh, J.; Bak, M., Long-term implants of Parylene-C coated microelectrodes. *Medical and Biological Engineering and Computing* 1988, 26, 96-101.

92.   Yang, M. K.; Tokarsky, E. W.; French, R. H., Optical properties of Teflon® AF amorphous fluoropolymers. *Journal of Micro/Nanolithography, MEMS, and MOEMS* 2008, 7, 033010-033010-9.

93.   Bateni, A.; Susnar, S.; Amirfazli, A.; Neumann, A., A high-accuracy polynomial fitting approach to determine contact angles. *Colloids and Surfaces A: Physicochemical and Engineering Aspects* 2003, 219, 215-231.

94.   Dodd, S. J., A Deterministic Model for the Growth of Non-conducting Electrical Tree Structures. *Journal of Physics D: Applied Physics* 2003, 36, 129-141.

95.   Schwartz, L. W.; Garoff, S., Contact angle hysteresis on heterogeneous surfaces. *Langmuir* 1985, 1, 219-230.

96.   Křenková, J.; Foret, F., Immobilized microfluidic enzymatic reactors. *Electrophoresis* 2004, 25, 3550-3563.

97.   Calleri, E.; Temporini, C.; Perani, E.; De Palma, A.; Lubda, D.; Mellerio, G.; Sala, A.; Galliano, M.; Caccialanza, G.; Massolini, G., Trypsin-based monolithic bioreactor coupled on-line with LC/MS/MS system for protein digestion and variant identification in standard solutions and serum samples. *Journal of proteome research* 2005, 4, 481-490.

98.   Hua, Y. The Use of Microfluidics for Multiplexed Protein Analysis. University of Alberta, University of Alberta Libraries, 2010.

99.   Li, D.; Teoh, W. Y.; Gooding, J. J.; Selomulya, C.; Amal, R., Functionalization strategies for protease immobilization on magnetic nanoparticles. *Advanced Functional Materials* 2010, 20, 1767-1777.

100.   Ghafourifar, G.; Fleitz, A.; Waldron, K. C., Development of glutaraldehyde‐crosslinked chymotrypsin and an in situ immobilized enzyme microreactor with peptide mapping by capillary electrophoresis. *Electrophoresis* 2013, 34, 1804-1811.

101.   Fan, J.-G.; Zhao, Y.-P., Characterization of watermarks formed in nano-carpet effect. *Langmuir* 2006, 22, 3662-3671.

102.   Carraway, A. D.; Burkhalter, R. S.; Timkovich, R.; Peterson, J., Characterization of heme peptides by mass spectrometry. *Journal of inorganic biochemistry* 1993, 52, 201-207.

103.   Mascot database search help: Trypsin autolysis. http://www.matrixscience.com/help/autolysis_help.html.

104.   Fonteh, A.; Harrington, R.; Tsai, A.; Liao, P.; Harrington, M., Free amino acid and dipeptide changes in the body fluids from Alzheimer's disease subjects. *Amino acids* 2007, 32, 213-224.

105.   Li, J.; Lipson, R. H., Assays Using a NIMS Chip: Loosely Bound but Highly Selective. *Analytical chemistry* 2013, 85, 6860-6865.

106.   Vaidyanathan, S.; Jones, D.; Ellis, J.; Jenkins, T.; Chong, C.; Anderson, M.; Goodacre, R., Laser desorption/ionization mass spectrometry on porous silicon for

metabolome analyses: influence of surface oxidation. *Rapid communications in mass spectrometry* 2007, 21, 2157-2166.

107. Trauger, S. A.; Go, E. P.; Shen, Z.; Apon, J. V.; Compton, B. J.; Bouvier, E. S.; Finn, M.; Siuzdak, G., High sensitivity and analyte capture with desorption/ionization mass spectrometry on silylated porous silicon. *Analytical chemistry* 2004, 76, 4484-4489.

108. Woo, H.-K.; Northen, T. R.; Yanes, O.; Siuzdak, G., Nanostructure-initiator mass spectrometry: a protocol for preparing and applying NIMS surfaces for high-sensitivity mass analysis. *Nature protocols* 2008, 3, 1341-1349.

109. Halliwell, C. M.; Cass, A. E., A factorial analysis of silanization conditions for the immobilization of oligonucleotides on glass surfaces. *Analytical Chemistry* 2001, 73, 2476-2483.

110. Cras, J.; Rowe-Taitt, C.; Nivens, D.; Ligler, F., Comparison of chemical cleaning methods of glass in preparation for silanization. *Biosensors and Bioelectronics* 1999, 14, 683-688.

111. Vallant, T.; Brunner, H.; Mayer, U.; Hoffmann, H.; Leitner, T.; Resch, R.; Friedbacher, G., Formation of self-assembled octadecylsiloxane monolayers on mica and silicon surfaces studied by atomic force microscopy and infrared spectroscopy. *The Journal of Physical Chemistry B* 1998, 102, 7190-7197.

112. Vorm, O.; Roepstorff, P.; Mann, M., Improved resolution and very high sensitivity in MALDI TOF of matrix surfaces made by fast evaporation. *Analytical Chemistry* 1994, 66, 3281-3287.

113. Ko, H.-Y.; Park, J.; Shin, H.; Moon, J., Rapid self-assembly of monodisperse colloidal spheres in an ink-jet printed droplet. *Chemistry of materials* 2004, 16, 4212-4215.

114.   Hu, J.-B.; Chen, Y.-C.; Urban, P. L., Coffee-ring effects in laser desorption/ionization mass spectrometry. *Analytica chimica acta* 2013, 766, 77-82.

115.   Kwan, J. K.; Sit, J. C., The use of ion-milling to control clustering of nanostructured, columnar thin films. *Nanotechnology* 2010, 21, 295301.

116.   Hall, J.; Taschuk, M.; Brett, M., Polarity-adjustable reversed phase ultrathin-layer chromatography. *Journal of Chromatography A* 2012, 1266, 168-174.

117.   Li, Y. L.; Gross, M. L., Ionic-liquid matrices for quantitative analysis by MALDI-TOF mass spectrometry. *Journal of the American Society for Mass Spectrometry* 2004, 15, 1833-1837.

118.   Bucknall, M.; Fung, K. Y.; Duncan, M. W., Practical quantitative biomedical applications of MALDI-TOF mass spectrometry. *Journal of the American Society for Mass Spectrometry* 2002, 13, 1015-1027.

119.   Bungert, D.; Heinzle, E.; Tholey, A., Quantitative matrix-assisted laser desorption/ionization mass spectrometry for the determination of enzyme activities. *Analytical biochemistry* 2004, 326, 167-175.

120.   Fujiwaki, T.; Tasaka, M.; Takahashi, N.; Kobayashi, H.; Murakami, Y.; Shimada, T.; Yamaguchi, S., Quantitative evaluation of sphingolipids using delayed extraction matrix-assisted laser desorption ionization time-of-flight mass spectrometry with sphingosylphosphorylcholine as an internal standard: practical application to cardiac valves from a patient with fabry disease. *Journal of Chromatography B* 2006, 832, 97-102.

121.   Zabet‑Moghaddam, M.; Heinzle, E.; Tholey, A., Qualitative and quantitative analysis of low molecular weight compounds by ultraviolet matrix‑assisted laser

desorption/ionization mass spectrometry using ionic liquid matrices. *Rapid communications in mass spectrometry* 2004, 18, 141-148.

122.   ALZET® - Formulating the Solution.

http://www.Alzet.com/products/guid_to_use/csf_preparation.html.

123.   Groseclose, M. R.; Andersson, M.; Hardesty, W. M.; Caprioli, R. M., Identification of proteins directly from tissue: in situ tryptic digestions coupled with imaging mass spectrometry. *Journal of Mass Spectrometry* 2007, 42, 254-262.

124.   Wu, Y.; Li, L., Development of Isotope Labeling Liquid Chromatography–Mass Spectrometry for Metabolic Profiling of Bacterial Cells and Its Application for Bacterial Differentiation. *Analytical chemistry* 2013, 85, 5755-5763.